Spring 2009

Characterization of Microwave Cavity Discharges in a Supersonic Flow

Dareth Janette Drake
Old Dominion University

CHARACTERIZATION OF MICROWAVE CAVITY DISCHARGES IN A SUPERSONIC FLOW

by

Dereth Janette Drake
B.S. May 2002, Longwood University
M.S. May 2005, Old Dominion University

A Dissertation Submitted to the Faculty of
Old Dominion University in Partial Fulfillment of the
Requirement for the Degree of

DOCTOR OF PHILOSOPHY

PHYSICS

OLD DOMINION UNIVERSITY
May 2009

Approved by:

Leposava Vušković (Director)

Svetozar Popović (Member)

Alexander L. Godunov (Member)

James L. Cox, Jr. (Member)

John B. Cooper (Member)

ABSTRACT

CHARACTERIZATION OF MICROWAVE CAVITY DISCHARGES IN A SUPERSONIC FLOW

Dereth Janette Drake
Old Dominion University, 2009
Director: Dr. Leposava Vušković

A partially ionized gas is referred to as either a plasma or a discharge depending on the degree of ionization. The term discharge is usually applied to a weakly ionized gas, i.e. mostly neutrals, where as a plasma usually has a larger degree of ionization. To characterize a discharge the plasma parameters, such as the rotational temperature, vibrational temperature, and electron density, must be determined. Detailed characterization of supersonic flowing discharges is important to many applications in aerospace and aerodynamics. One application is the use of plasma-assisted hydrogen combustion devices to aid in supersonic combustion. In conditions close to the real combustion environment, a cylindrical microwave cavity was used to study the effects of hydrogen and air admixtures to plasma parameters in an argon supersonic flowing discharge. Argon and hydrogen were chosen since their atomic and molecular structure are well documented in the literature. In addition, argon, as a noble gas, will help to decrease the penalty from ionization. However, the presence of hydrogen, nitrogen, and oxygen molecules leads to complex branching inter-radical chemistry, which may result in the decrease of the degree of ionization and the loss of combustion enhancing radicals. A qualitative description of the ionization loss was the main goal of this thesis. To complement the experiments a gas kinetic model was developed to explore the extent of ionization loss due to the addition of hydrogen and air.

The second goal of this thesis is to develop a supersonic flowing microwave discharge to validate Martian atmospheric entry models and explore the prospect of harvesting Martian entry plasma. The interactions between the Martian atmosphere and the Mars Landers have been a challenging issue from the very beginning of Mars exploration. During the entry phase, the friction between the atmosphere and probes cause thermal ionization and heating of the surrounding gas. An atmospheric and

kinetic model was developed for Martian atmospheric entry plasma based on the existing Mars data. The entry plasma parameters vary considerably depending on the spacecraft's trajectory. In addition, we found that variations in the entry plasma composition were considerable and have to be included in various future harvesting schemes.

The experimental set-up included a de Laval nozzle in conjunction with a cylindrical microwave resonance cavity to create a Mach 2 supersonic flowing microwave discharge in the following gases: (1) Ar with up to 10% hydrogen and 45% air and (2) Martian simulated mixture composed of 95.7% CO_2, 2.75% N_2, and 1.55% Ar. Optical emission spectroscopy was employed to perform detailed measurements of the spectra of Ar, H, CO, and N_2. The gas temperature, vibrational temperature, and electron temperature along with the electron density were determined for both types of gas mixtures. We observed a decrease in the rotational and vibrational temperatures when hydrogen and air were added to an argon discharge. From analysis of the data for a pure air discharge, we determined that this decrease was due to the mixing of the different gas species. In addition, we found that the electron temperature did not change with the power density in the discharge, but it did decrease when hydrogen was added to a pure Ar discharge.

We developed a technique for finding the electron density by using the N_2 second positive system. Direct indications of ionization loss were observed in the electron density measurements taken in the $Ar/H_2/Air$ discharges. In addition, in the Martian simulated mixture we found that the electron density measurements were consistent with those predicted by the atmospheric entry model. Both the experimental and model results for both types of gas mixtures indicate that the multispecies chemisty of the gases is very important to the characterization of a supersonic flowing discharge.

ACKNOWLEDGMENTS

I would like to begin by thanking my advisor, Dr. Leposava Vušković who has always been there to give me aid and support when things were not going right in my research. Her knowledge and enthusiasm about physics have been crucial to my development as a physicist. Additionally, I would like to thank Dr. Svetozar Popović, for giving me his time, patience, and support. His skills in the laboratory and invaluable knowledge of physics have been essential to my completing this research project.

To the faculty, staff, and graduate students of the physics department at ODU, thank you for all your support, laughter, and encouragement over these last six years. I especially want to thank my fellow graduate student, Marija Rašković, who's understanding of plasma physics and spectroscopy has been invaluable. In addition, I want to thank Saori Pastore and Eman Ahmed whose depth of knowledge never ceases to amaze me and whose friendship I will cherish always.

Most importantly I want to especially thank my mom, dad, and brother, Glinn, who have supported me throughout this whole experience. Without you I would not be who I am today.

TABLE OF CONTENTS

LIST OF TABLES

LIST OF FIGURES

CHAPTER I

INTRODUCTION

In the mid-1950s, the United States Air Force began studies into the use of hypersonic vehicles for space flight. By the early 1960s, the Air Force, in conjunction with the National Aeronautics and Space Administration (NASA), had developed the X-15, which set altitude and speed records for that time. This rocket propelled vehicle could send astronauts into Earth's lower orbit (100 km). But these rockets required enormous amounts of fuel to launch a small craft with one to three humans on board into space. As such the average pay load for a rocket propelled craft was only 1% of the total lift mass [1]. Electric propulsion was then suggested as a reasonable alternative to the rocket engines for its possible ability to allow for large manned missions to other planets and exploring the farthest reaches of our solar system [2]. In the first part of the 21st century, NASA and the European Space Agency (ESA) started to use electric propulsion engines in space vehicles. In these devices, a plasma is generated inside of the engine to allow for high exhaust velocities, which alleviates the need for extra fuel for take off. Since this research began, the supersonic flowing discharges and plasmas have been used for many aeronautic applications in fields beyond electric propulsion engines, including supersonic drag reduction, inlet shock control, aid to supersonic combustion, atmospheric entry modeling validation, generation of ceramic coatings, and carbon nanotube production.

Numerous aeronautics applications have met with the relatively neglected field of plasma aerodynamics. Many of these applications fall within the range of the thermodynamic and plasma parameters that have not been properly characterized. The electron density is one such parameter. There are two commonly employed methods to determine the electron density: analysis of the stark broadening of spectral lines and the implementation of a Langmuir probe. Stark broadening occurs when the radiation emitted by a single particle is effected by the charged particles surrounding it [3]. Stark broadening allows for the determination of the electron density in plasmas at values above 10^{15} cm^{-3}. A Langmuir probe is a type of electrical probe in which a small piece of conducting material is inserted into a discharge while maintaining an applied voltage to produce electronic or ionic current [4]. This device will determine

This dissertation follows the style of *Physical Review E*.

the electron density up to 10^{11} cm^{-3}. As can be seen there is a region between 10^{11} and 10^{15} cm^{-3} in which neither of these methods are able to accurately measure the electron density. This is the region in which most of the plasmas used for aeronautics applications exist.

Another plasma parameter which is important for characterization is the gas-kinetic temperature. This quantity is needed in order to characterize the thermal motion of the bulk, ground state neutrals. Lasers and electric probes are often used to determine this feature of the plasma. However, these methods are both expensive and obtrusive. Therefore it is essential that we find an inexpensive, nonintrusive, and *in situ* technique which can accurately determine the gas temperature. Emission spectroscopy is a relatively simple technique and it is both nonintrusive and *in situ.* However, this technique does not allow for direct measurement of the gas temperature. In the literature, it is assumed that the gas temperature can be equated to the rotational temperature if the molecular excited states are produced by direct electron excitation from the ground state [5]. Therefore, by analysis of the spectra of the excited states of molecules we can determine the rotational temperature and thus the gas temperature. Emission spectroscopy has been shown to provide fairly good results for the gas temperature from analysis of the spectra of different molecules [6, 7].

For most aeronautics applications, molecularly complex gases are used to produce the required plasma. The collisional dynamics of these flows is very complex. Bogaerts and Gijbels [8] used a combination Monte Carlo and fluid model to analyze a glow discharge of 99% Ar and 1% H_2. In order to completely characterize this discharge, they needed to include over 60 reactions in their model. Since most of the gases used in aeronautics applications contain more then two species, the multispecies plasma dynamics must be determined. However, these types of interactions are very complex and thus are not very well understood. In addition, in these plasmas the presence of multiple molecular species can cause complex branching and inter-radical collisional dynamics. This leads to a need to measure the vibrational temperature since the bonds between the atoms in different molecules can break at high vibrational energies (temperatures) which generates new species in the discharge.

Diagnostics are not the only issues with these plasmas, there are also physical problems which arise from the interactions of these plasmas and the supersonic flow. Inside of these flows, shock waves will form. Many experiments have been performed

with the aim to understand the interaction of a shock wave and a weakly ionized gas since the electronic and thermal properties of the plasma can affect the shock wave. This interaction can manifest itself in the form of a localized increase of electron temperature, plasma induced shock dispersion and acceleration, optical emission enhancement, or double (or multiple) electric layers. In an early experiment by Ionikh *et al.* [9], a short discharge pulse, in which the steady state density values of the excited and charged atoms were maintained, was used to separate the vibrational and electronic effects from the thermal ones. They demonstrated that the gas temperature was the main influence on a shock wave in a supersonic flowing plasma. In addition, many groups [10, 11] found an increase in the local shock velocity downstream as compared to the velocity upstream. They determined that this increase could not be due solely to the temperature gradient. Further experiments found that this increase was directly dependent on the direction of the applied electric field [12].

The interaction of a plasma with a shock wave can also cause a dispersion of the shock [12], which forms a double peak in flow. This effect has been attributed to the separation and redistribution of space charge across the shock layer, i.e. the formation of a double electric layer. In addition, an excessive increase in radiation from the electronically excited states across the shock layer have also been observed [13, 14, 15]. This increase could not be explained by the linear approximation, where the height of potential barrier in the double layer was of the order of the electron temperature in the unperturbed plasma. Siefert *et al.* [16] proposed that a strong double electric layer existed at the shock fronts based on the interactions between heavy particles in the plasma-shock region. Thus, one of the aims of this project was to observe the changes in population across the shock front formed by a spherically blunt body in order to assess the strength of the double layer.

All of these problems, both diagnostic and physical, must be resolved in order to be able to use supersonic discharges for various aeronautic applications. One of the most common applications of supersonic discharges is to plasma-assisted combustion [17, 18]. At supersonic speeds, the compression required for combustion to occur in an engine can heat the gas beyond the operating temperature of the materials used [19]. A possible resolution to this problem is to use a plasma source to partially ionize the flow and produce excited species or radicals [20, 21]. The simplest form of a plasma ignition device is an argon hydrogen plasma torch [22]. A plasma torch is a device which ionizes a gas and creates a directed flow of plasma out of a nozzle

head. In addition to Ar/H_2, the most common gas mixtures used in plasma torches for plasma-assisted supersonic combustion are N_2 /H_2, H_2 /O_2, and hydrocarbons. These plasma torches can be DC electric discharges, nanosecond pulsed discharges, or microwave discharges.

In this research we are focused on an Ar/H_2 microwave discharge, since the modeling of the gas mixture is not too complex. This gas mixture is also not highly flammable, as opposed to the H_2/O_2. In our mixture, H_2, which is a simple molecule, interacts with the O_2 in the air to create combustion. The Ar in this mixture acts as a buffer gas, thus controlling the reaction. One of the main issues associated with Ar/H_2 discharges is ionization loss. It has been well documented that when small amounts of H_2 are added to an Ar discharge, the electron density will decrease due to election-ion recombination [8]. This phenomena has been detected not only in models but also in experiments with subsonic flowing discharges [23, 24]. However the processes leading to ionization loss are poorly understood and their study was one of the primary goals of this research.

The second part of this research is focused on atmospheric entry modeling. Supersonic discharges are used to simulate the plasma which forms around the outside of a ship during the entry phase. Sending manned missions to other planets in our solar system, primarily Mars, is one of the primary objectives of NASA. However, this requires a better understanding of the problems each crew will face not only once on the planet but also during the entry phase. The interactions between a ship and the atmosphere can be very complicated and currently are not fully understood. Experiments have been conducted to recreate these conditions for Earth and Mars for the purpose of modeling. In these experiments, $N_2/O_2/Ar$ [25] gas mixtures are used for Earth entry simulations and $CO_2/N_2/Ar$ mixtures for Mars. The mixtures are then sent through a convergent-divergent nozzle to create supersonic flow and then ionized by some means, most commonly radio frequency or microwaves [26]. By adding models of geometries similar to that of the probes, shock waves are formed in the discharge. Another approach is to allow the gas to be ionized either in an electric discharge tube [27] or by use of microwaves. Then a shock wave is produced, most commonly by a spark gap generator [28], and allowed to propagate through the discharge. The interactions between these shock waves and the discharge can then be studied in order to understand characteristics of atmospheric entry. Detailed understanding of atmospheric entry is also key to many experiments which have been

proposed, including production of O_2 in the Martian atmosphere [5] and generation of power by use of a magnetohydrodynamic generator, see Appendix A.

Although the applications of electrical discharges have been studied indepthly, there are still very few studies devoted to the diagnostics of plasma parameters, such as rotational and vibrational temperature, electron density, and applied electric field. The first aim of this research is to analyze the plasma parameters associated with plasma-assisted supersonic combustion and atmospheric entry modeling. The second aim is to understand the role of ionization loss in $Ar/H_2/Air$ supersonic mixtures as associated with supersonic combustion using experimental data and gas kinetic modeling. The last aim of this research is to model Martian atmospheric entry plasma (MAEP) using *in situ* techniques.

This dissertation is organized as follows. In chapter 2, we describe the experimental set-up and diagnostic techniques used in this research. In addition, the calculations used for study of the plasma parameters and experimental results are described for both types of plasmas. In chapter 3, we present the characterization of $Ar/H_2/Air$ discharges using gas kinetic modeling. The electron energy distribution functions and associate electron transport coefficients are discussed along with a comparison to experimental results. In chapter 4, we show the modeling techniques used to study Martian atmospheric entry plasma and compare our modeling results with data from the NASA probes. Finally in chapter 5, we present our conclusions about this research.

CHAPTER II

EXPERIMENT

II.1 EXPERIMENTAL SET-UP

We built a set-up that allows for study of supersonic discharges in a small scale laboratory setting since (total length of the system is about 2.5 m). One of the main advantages of this type of apparatus is that it allows for uniform ionization of a large valume of the flow at any given moment. Another key advantage to this experiment is that the microwave cavity allows for easy breakdown of the gas mixtures under study. In addition, we are able to work at higher Mach numbers since the geometry of a convergent-divergent nozzle can be easily altered to achieve them.

The scheme of the supersonic flowing discharge set-up is shown in Fig. 1. Gas mixtures of (1) pure Ar with up to 10% H_2 and up to 45% air and (2) a Martian simulated mixture of 95.7% CO_2, 2.75% N_2, and 1.55% Ar were fed into the stagnation chamber through a gas manifold. Gas flow was established by a Pfeiffer Okta 500 A roots blower, which was supported by two Varian SD-700 roughing pumps. The capacity of the pumping system allowed for generation of supersonic flow at static pressures of 1 to 20 Torr.

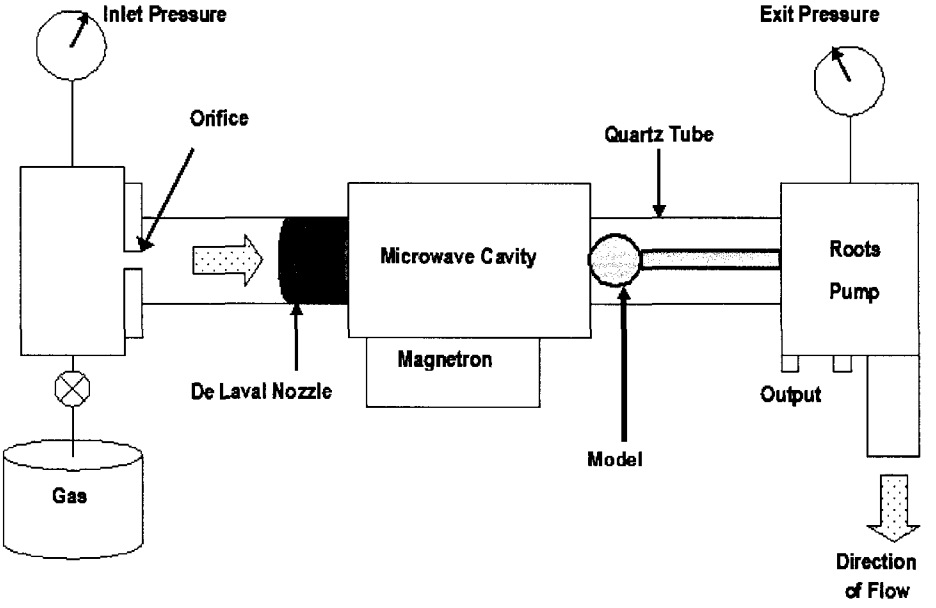

FIG. 1: Scheme of the supersonic flowing microwave discharge.

We have used a commercial microwave generator, operating in the S-band at 2.45 GHz, to sustain a cylindrical cavity, pulsed repetitive discharge at power densities between 0.5 and 5.0 W/cm^3. Using a quartz tube at pressures of 1 to 3 Torr as a waveguide and the de Laval nozzle, positioned so that the divergent end was in the same plane as the cavity wall, a supersonic discharge was also sustained downstream of the microwave cavity, which operated in the $TE_{1,1,1}$ mode. At higher power densities, the discharge expanded upstream through the nozzle into the converging section where it formed a symmetric pattern of bright filaments.

II.1.1 Microwave Resonance Cavity

In this experiment, a right rectangular cylindrical resonance cavity was used to sustain a pulsed repetitive discharge. The relationship between the resonance frequency (ω) and the cavity dimensions can be derived from the propagation of electromagnetic waves in a hollow metallic cylinder [29]. For a cavity operating in TE mode, this relationship is

$$\omega_{mnp} = \frac{1}{\sqrt{\mu\epsilon}}\sqrt{\frac{x_{mn}^2}{r^2} + \frac{p^2\pi^2}{d^2}}, \tag{1}$$

where m, $p = 0, 1, 2, \ldots$, $n = 1, 2, 3, \ldots$, μ is the permeability of the material, ϵ is the permittivity of the material, r is the inner radius of the cavity, d is the length of the cavity, x_{mn} is the n$^{\text{th}}$ root of the equation $J_m(x) = 0$, and $J_m(x)$ is the m$^{\text{th}}$ order Bessel function that satisfies the boundary conditions for the cavity. This cavity was designed to operate in the lowest TE mode, $TE_{1,1,1}$.

Since our cavity is an imperfect conductor, the microwave energy in the cavity can be lost in many ways, as discussed in Ref. [30]. Heat is the most common loss mechanism in a microwave cavity. The quality factor, or Q-factor, is a measure of the rate at which a vibrating system dissipates its energy into heat. In an optical resonance cavity, the Q-factor is defined as the ratio of the energy stored in the cavity (E) to the power dissipated by the cavity (P) times the resonance frequency (ω_o),

$$Q = \omega_o \frac{E}{P}. \tag{2}$$

The Q-factor for any resonance cavity is calculated [29] using the following relationship

$$Q = \frac{\mu_o}{\mu_c \delta} \frac{1}{2(1 + \epsilon_\lambda \frac{Cl}{4A})}. \tag{3}$$

Here μ_o is the permeability of free space, μ_c is the permeability of the cavity walls, A is the cross sectional area of the cavity, C is the circumference of the cavity, l is the length of the cavity, ϵ_λ is a dimensionless number on the order of unity, and δ is the skin depth which is defined as

$$\delta = \sqrt{\frac{\rho}{\pi f \mu_c}} \tag{4}$$

where ρ is the resistivity of the cavity walls and f is the resonance frequency.

The cavity was constructed from aluminum and had an inner radius of 0.037 m, which aloud us to determine

$$\begin{aligned} \rho &= 2.65\ \mu\Omega[\text{cm}] \\ \mu_o &= 4\pi \times 10^{-7}\ \text{H/m} \\ C &= 0.232\ \text{m} \\ A &= 0.0043\ \text{m}^2 \end{aligned}$$

and, since aluminum is not magnetic in nature, $\mu_c = \mu_o$. The length of the cavity was then determined by subtracting the detuning length and widths of each end wall from the total length of the cavity, which gave a length of about 0.25 m. Additionally, the resonance frequency was 2.45 GHz. By substituting these values into Eqs. (3) and (4), we found that the resonance cavity has a Q-factor of 2.14 $\times 10^{-4}$.

Once the Q-factor for the cavity is known, we needed to tune the cavity. As the detuning rods are moved in and out of the microwave cavity (see Fig. 2) the spectral line intensity for the plasma will change. At some point this intensity was at its maximum.

To find this maximum position, the microwave cavity was placed at the very end of the de Laval nozzle. Then the rods were pulled completely out of the cavity, which had a length of about 0.11 m. The flow for this calibration measurement consisted of a mixture of 95% Ar and 5% H_2. The ambient pressure was set at 33.0 Torr and

the output pressure at 2.2 Torr, as indicated by the two barometers placed at either end of the quartz tube.

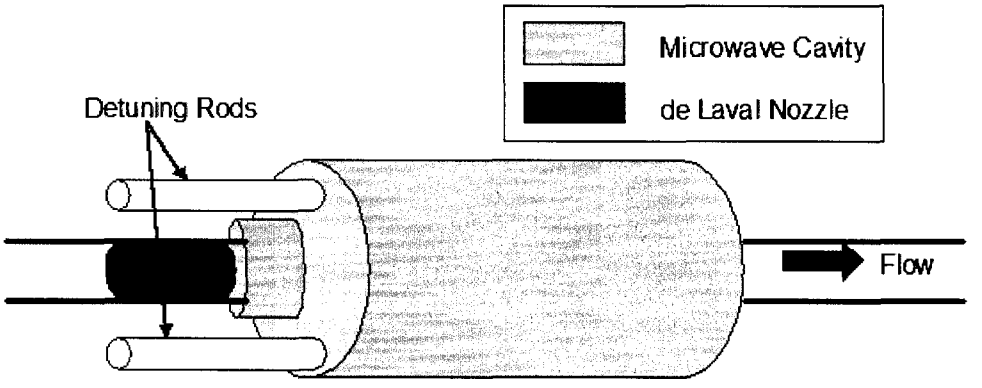

FIG. 2: Schematic of detuning rods for the microwave cavity.

Next, the power density was set to 1.05 W/cm^3 for the microwave cavity. Finally, the intensity of the hydrogen gamma (H_γ) spectral line (434.0 nm) was observed using grating 1 of the spectrometer. I continued this process for different lengths of the detuning rods and determined that the maximum spectral line intensity occurred when the rods were 0.078 m out of the cavity.

II.1.2 Convergent-Divergent (de Laval) Nozzle

The most common approach to studying supersonic and hypersonic air flows is by use of a convergent-divergent nozzle, or de Laval nozzle as it is known. Developed in 1887 by Carl de Laval, the essential physics of this device is that as the air flows through the convergent section of the nozzle it will begin to accelerate till it approaches the throat of the nozzle where it will achieve Mach 1, see Fig. 3.

The continuity equation for fluid flow expresses this relationship between the cross sectional area and the velocity of the flow at two different points,

$$A_1 v_1 = A_2 v_2. \tag{5}$$

It is obvious from Eq. (5) that as the area decreases, the velocity must increase at a similar rate causing the observed acceleration to Mach speed. After leaving the

throat of the nozzle, the diameter of the divergent section of the nozzle increases very rapidly causing a further increase in acceleration towards the final Mach number [31].

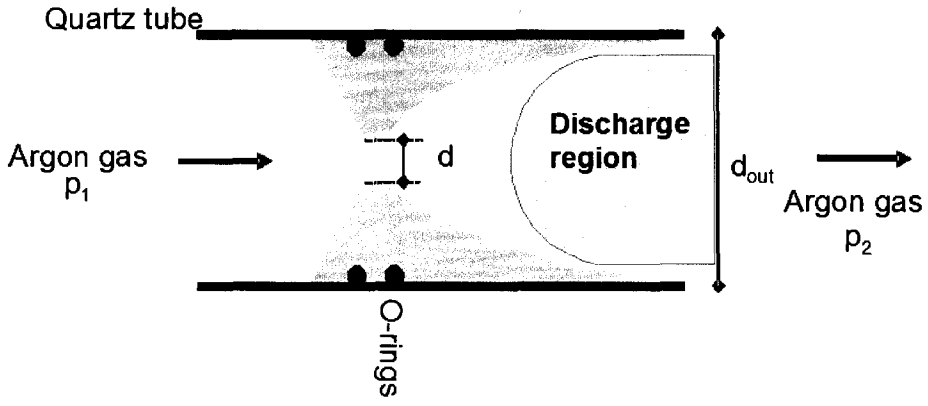

FIG. 3: Schematic drawing of the de Laval nozzle.

One of the most important parts of the de Laval nozzle is the design of the divergent region. If the geometry of the nozzle is inaccurate, shock waves will form in the flow which can be undesirable in most circumstances. If the angle of this region is set such that when a collision is made with the wall the new direction of the flow is parallel with the axis of symmetry for the nozzle, then uniform supersonic flow can be obtained.

The Mach number (M) is defined as

$$\mathrm{M} = \frac{v}{a_s}, \tag{6}$$

where v is the velocity of the object and the speed of sound (a_s) is defined as

$$a_s = \sqrt{\frac{\gamma p}{\rho}} = \sqrt{\gamma R T}, \tag{7}$$

where p is the pressure, ρ is the density, R is the specific gas constant, T is the temperature, and the specific heat ratio (γ) is defined as

$$\gamma = \frac{\mathrm{c}_P}{\mathrm{c}_V}. \tag{8}$$

Here c_P is the specific heat at constant pressure and c_V is the specific heat at constant volume. If the Mach number is less then 1, then the flow is said to have a subsonic speed. At $M = 1$, the flow is referred to as sonic, but in the range $0.8 \leq M \leq 1.2$ the flow is described as transonic. If the flow has a Mach number of $1 < M \leq 5$, the flow is considered supersonic. If the flow has a Mach number greater then 5, it is referred to as hypersonic.

Each nozzle will have one specific Mach number, which is based upon the design of the nozzle. To construct a de Laval nozzle, the desired Mach number and the specific heat ratio, Eq. (8), of the gas being used must be known. Then by knowing the cross sectional area of the exit, the area-Mach number relation, Eq. (9), can be employed to calculate the cross sectional area of the throat [32],

$$\left[\frac{d_{out}}{d}\right] = \frac{1}{M^2}\left[\frac{2}{\gamma - 1}\left(1 + M^2\frac{\gamma - 1}{2}\right)\right]^{\frac{\gamma+1}{\gamma-1}}. \tag{9}$$

The de Laval nozzles used in this study were machined from unfired Hydrous Aluminum Silicate (Grade "A" Lava). The nozzle inside of the microwave cavity had little effect on the discharge, since lava is a dielectric with a dielectric constant of approximately 5.3. We added an adjustable hollow plate tuner to the microwave cavity to avoid detuning effects caused by the nozzle.

Supersonic flow downstream of the nozzle was analyzed in free flowing pure argon in the absence of the discharge. By measuring the inlet pressure (p_{in}) and the exit pressure (p_{out}), we determined the Mach number by employing

$$M = \sqrt{\frac{\left(\frac{p_{in}}{p_{out}}\right)^{\frac{\gamma-1}{\gamma}} - 1}{(\gamma - 1)/2}}. \tag{10}$$

We constructed five nozzles of varying lengths (43-80 mm) and shapes for the divergent section (conical and parabolic). We determined that the best shape for supersonic flow was conical. Based on our nozzle's geometry, we calculated the Mach number from Eq. (9) to be 2.91 in a pure argon flow. The Mach number calculated from Eq. (10), above 3.5 Torr, for the conical nozzle used in this experiment was 2.09 $\pm$ 0.02. The difference in these two numbers is most likely due to turbulence in the

flow. Previously, we mentioned that this turbulence could be due to the angle of the divergent section, but another possible source of turbulence is the smoothness of the surface of the divergent section of the nozzle. If the nozzle's surface is not smooth, there will be a small areas where flow collisions will not be parallel with the surface of the nozzle, thus producing turbulence in the flow.

We found that changing the position of the nozzle in the quartz tube had little effect on the calculated Mach number, $\pm$ 5%. From Fig. 4, we observed that as the pressure increased the Mach number also increased until it reached a steady state at values above 3.5 Torr. The rapid change in the Mach number below 3 Torr makes the data in this area less reliable.

In addition, we observed how the Mach number varied inside of the Martian simulated discharge. From Fig. 5, we see that the Mach number between 0.5 and 2.5 Torr increases almost linearly till it reaches a plateau. This plateau in the Martian mixture occurs at around Mach 2.15, while in the pure Ar flow it was at 2.09. This difference is expected since different gases can have different Mach numbers even under the same experimental conditions due to a difference in the specific heat ratio (γ).

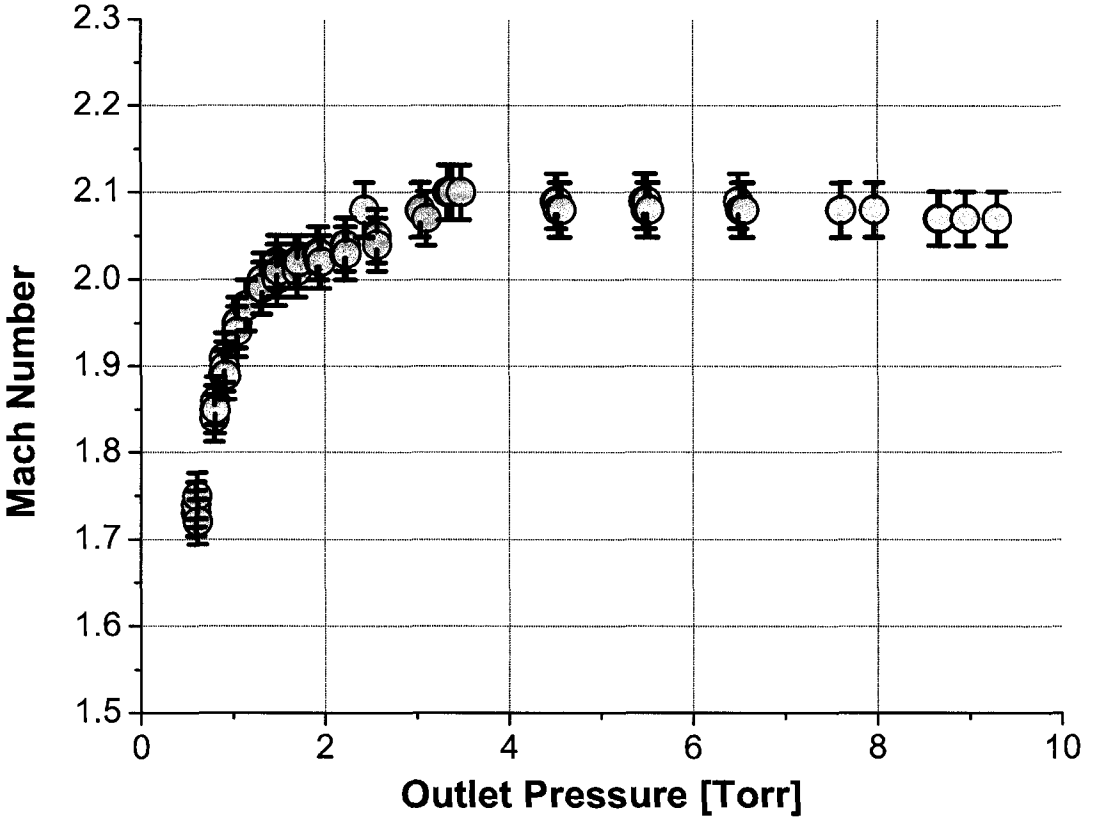

FIG. 4: Mach number as a function of the pressure in the microwave cavity in a pure Ar flow.

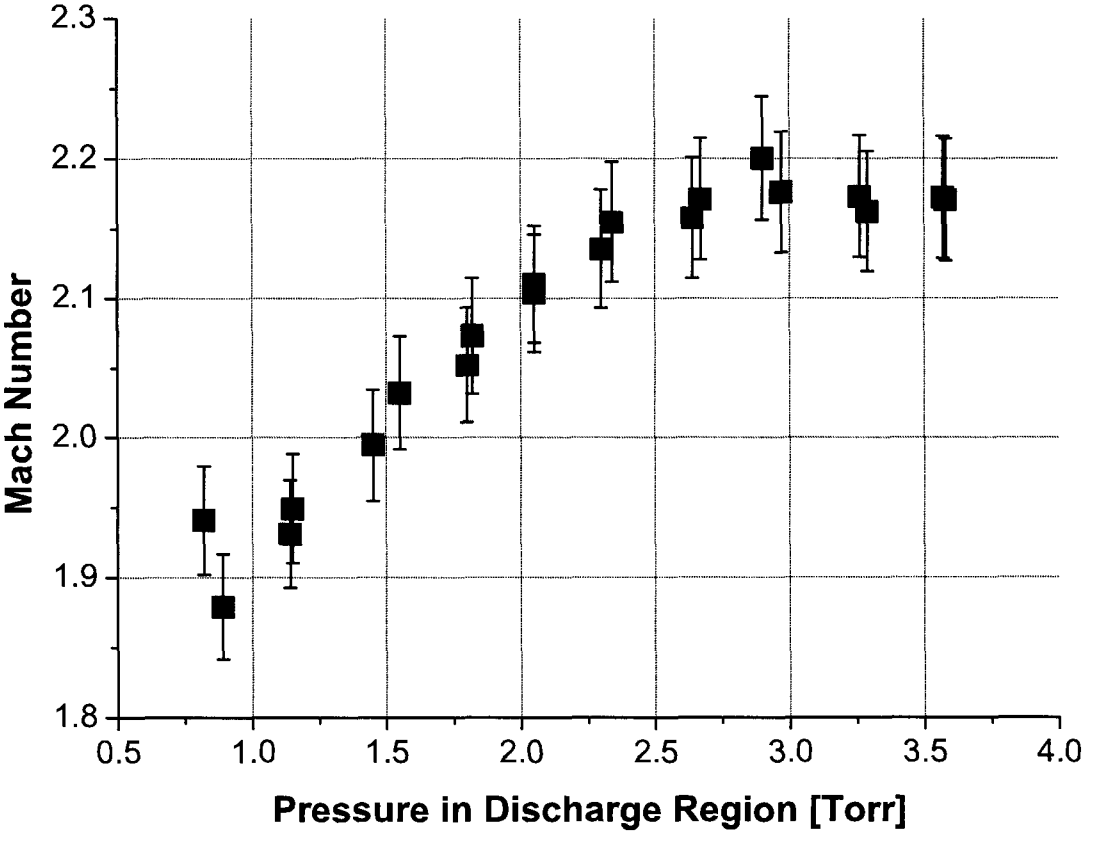

FIG. 5: Mach number as a function of the pressure in the microwave cavity in a flow of Martian simulated gas.

II.1.3 Spherical Blunt Bodies

Shock waves are formed when a supersonic flow experiences a sudden change in direction due to the presence of an object [33]. We used spherically blunt bodies placed in the path of the flow to create stationary acoustic shock fronts. We constructed three models from Teflon measuring diameters of 9.5, 12.7, and 15.9 mm. The models were attached to Teflon rods connected to the end of an aluminum pole which was then controlled by a manual traverse so that the model could be moved up to 25 mm along the axis of symmetry for the discharge allowing for analysis of the shock fronts. In our experiment we used the 9.5 mm model since it was the smallest and had the least possibility of choking the flow at the sides of the model which can make the shock front harder to visualize.

By assuming that the flow in front of the blunt body along the axis of symmetry has a constant density, we can make approximations for the standoff distance for the shock front in the discharge. Since the Mars probes are conical in shape, the first approximation we made was that these conical shape bodies can be approximated by spherically symmetric bodies, see Fig. 6.

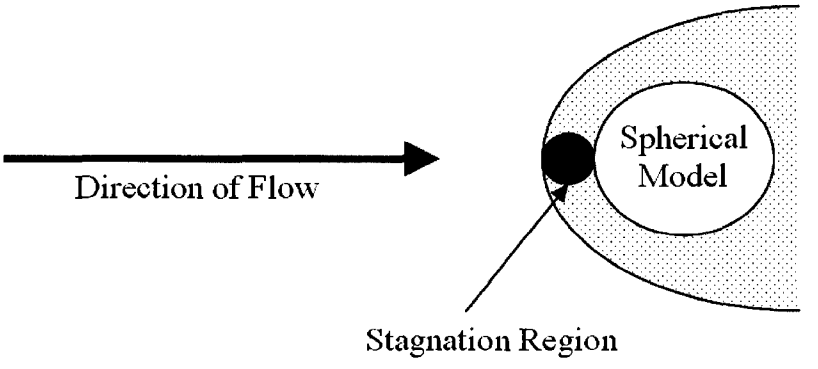

FIG. 6: Schematic of stagnation point region in front of a spherical model.

Now if we assume that the shock front will be at a constant distance from the spherical models, we can say that the body to shock ratio in the stagnation point region will be [34]

$$Y = \frac{\mathrm{R_{body}}}{\mathrm{R_{shock}}}, \tag{11}$$

where R_{body} is the radius of the model and R_{shock} is the radius of the shock. The shock density ratio,

$$\epsilon = \frac{(\gamma - 1)M^2 + 2}{(\gamma + 1)M^2}, \tag{12}$$

will satisfy

$$0 = 3(1 - \epsilon)^2 Y^5 - 5(1 - 4\epsilon)Y^3 + 2(1 - \epsilon)(1 - 6\epsilon) \tag{13}$$

such that the relationship between the Mach number and the standoff distance,

$$\delta = R_{shock} - R_{body}, \tag{14}$$

can be found from

$$\epsilon = \frac{b + \sqrt{b^2 - ac}}{a}, \tag{15}$$

where

$$\begin{aligned} a &= 3(Y^5 + 4) \\ b &= 3Y^5 - 10Y^3 + 7 \\ c &= 3Y^5 - 5Y^3 + 2. \end{aligned}$$

Using R_{body} for each of the models and γ for argon, which is 1.67, we calculated the standoff distance as a function of the Mach number. From Fig. 7, we observe that the standoff distance decreases with increasing Mach number for all three models. Since the Mach number for our flow is 2.09 in pure Ar, this figure indicates that the standoff distance for our shock front will be approximately 1.5, 2.0, and 2.5 mm in front of the 9.5, 12.7, and 15.9 mm models, respectively.

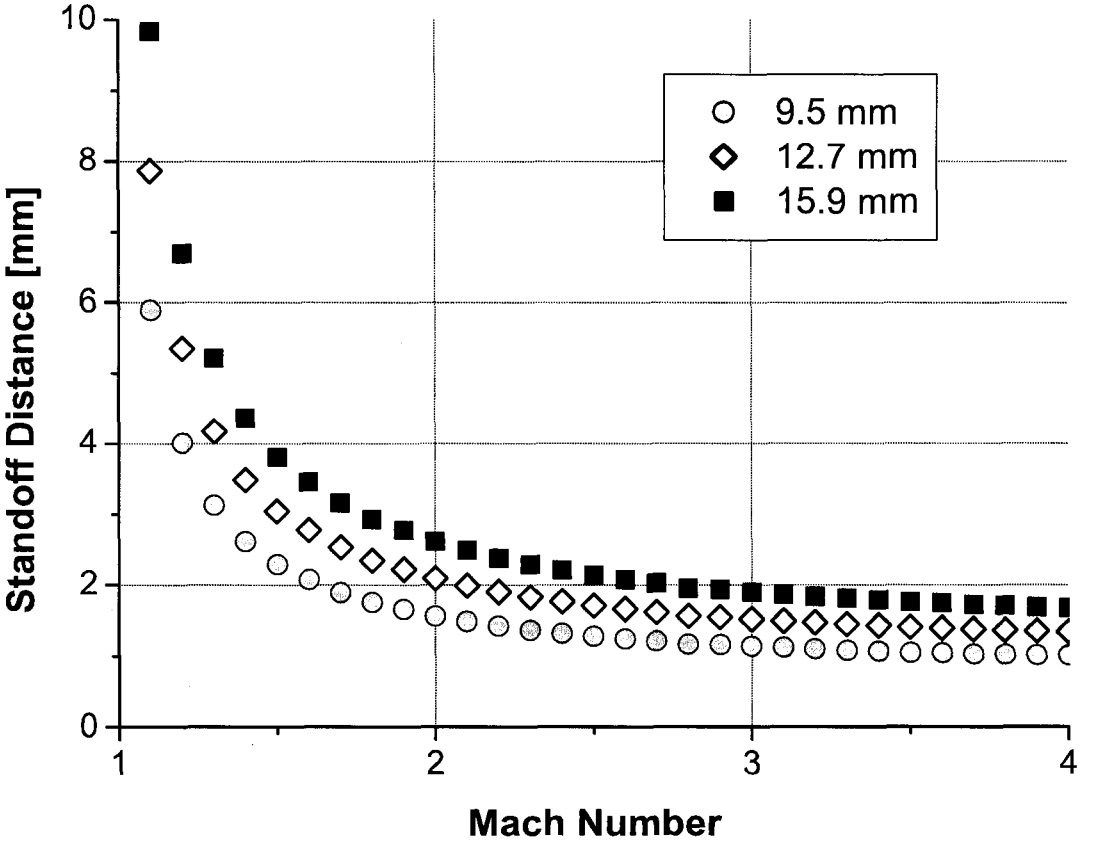

FIG. 7: Standoff distance for the shock fronts as a function of the Mach number for the 9.5, 12.7, and 15.9 mm models in a pure Ar discharge.

In addition to the standoff distance, two other parameters are important for identifing the shock front in a discharge. The first of these parameters is the shock thickness (δ). The shock thickness is defined as [35]

$$\delta = l_o \frac{\mathrm{M}}{\mathrm{M}^2 - 1}, \tag{16}$$

where M is the Mach number and l_o is the mean free path length defined by

$$l_o = \frac{1}{n\sigma}, \tag{17}$$

where n is the number of molecules per unit volume and σ is the effective cross section. In Fig. 8, we observe the change in the shock thickness with pressure in the discharge region for a discharge of pure Ar. The figure shows a strong decrease in thickness at low pressures. For example at a pressure of 2.5 Torr the shock thickness will be 2.06 mm.

The other parameter is the density ratio (ρ_0/ρ). For a monoatomic gas the density ratio can be equated to a dimensionless velocity (η) or specific volume [35]. The equation for the change in the density ratio with respect to the distance through the shock front (x) is

$$\frac{(1-\eta)}{(\eta-\eta_1)^{\eta_1}} = \frac{(1-\sqrt{\eta_1})}{(\sqrt{\eta_1}-\eta_1)^{\eta_1}} \exp\left[\frac{1.1x}{\delta}\right], \tag{18}$$

where η_1 is defined as

$$\eta_1 = \frac{1}{4} + \frac{3}{4}\frac{1}{\mathrm{M}^2}. \tag{19}$$

The gas density ratio was determined as a function of $\mathrm{x/l_0}$ in a Mach 2 discharge of pure Ar at a pressure of 2.5 Torr and a temperature 1200 K. We present these results in Fig. 9 in which the shock front is located at position 0. From the figure, we see a large change in the density as we cross the shock region. Thus we should observe a similar change in density at the shock fronts in our discharges.

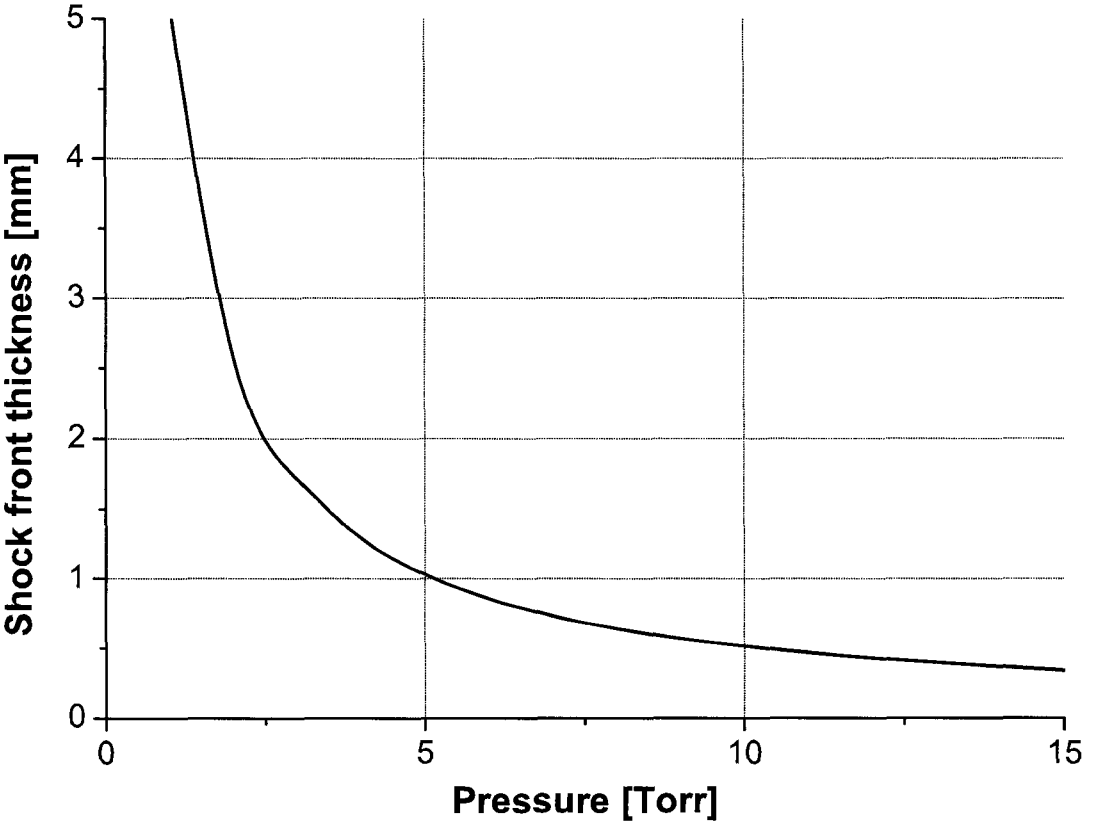

FIG. 8: Shock front thickness as a function of the pressure in a discharge of a pure Ar discharge.

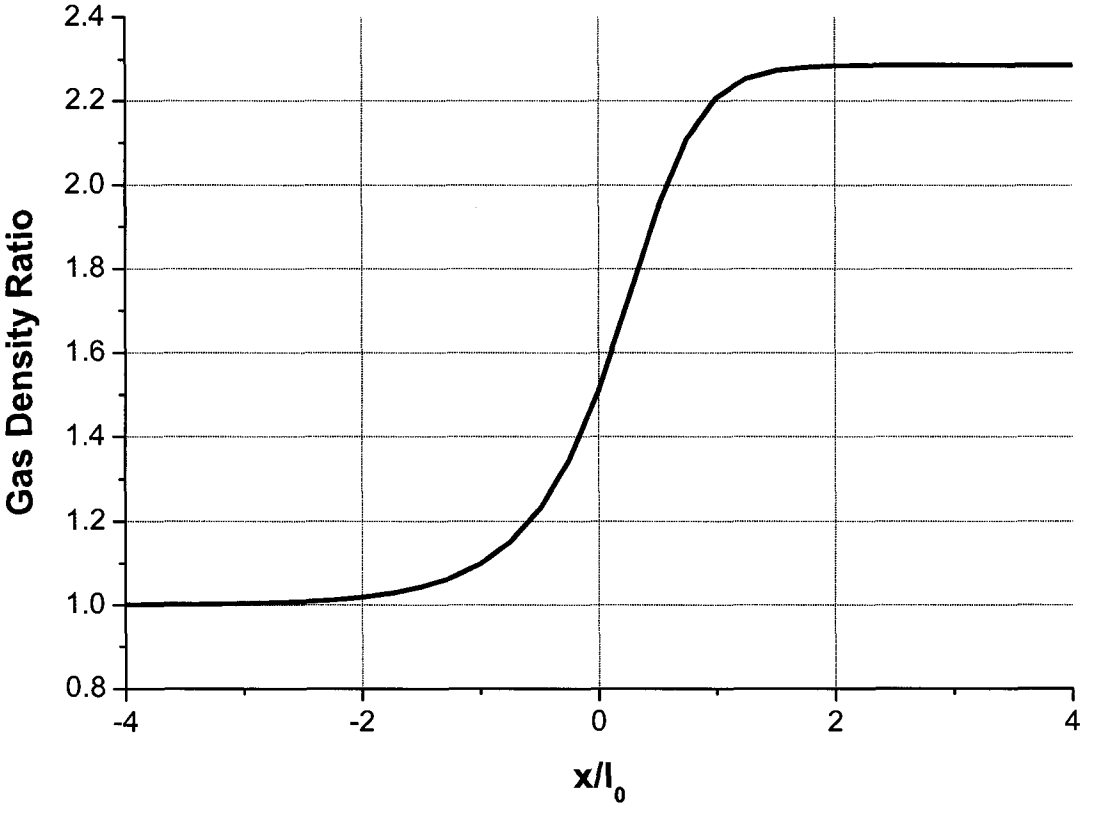

FIG. 9: Gas density ratio across a shock front as a function of the position (x/l_0) in a Mach 2 discharge of pure Ar at a pressure of 2.5 Torr and a temperature of 1200 K.

II.2 DIAGNOSTIC TECHNIQUES

There are many possible diagnostic techniques which can be used to characterize a discharge or plasma. One of the most basic and useful is the Langmuir probe. The idea behind this piece of equipment is that a small piece of conducting material is inserted into a discharge while maintaining an applied voltage to produce electronic or ionic current [4]. The basic problem for this type of diagnostic tool and the others like it [36] is that the interpretation of the results is relatively complicated. These techniques require that something be placed into the plasma, which can cause problems both with calculating discharge parameters and within the discharge itself. Therefore it is unwanted. We have thus chosen to use optical emission spectroscopy for our diagnostic technique since it is simple, non-intrusive, and *in situ.* In order to understand the stability of the discharge we decided to added tp the appartus a very basic set-up for the detection of photons.

II.2.1 Optical Emission Spectroscopy

We used optical emission spectroscopy on the flow by employing an Acton SpectraPro-500i: Model SP-556 Spectrograph in conjunction with a charged-coupled device (CCD) camera. The spectrometer had a focal length of 0.5 m and was equipped with a triple grating turret, where grating (1) had 3600 grooves per millimeter with a resolution of 0.005 nm, grating (2) had 1800 grooves per millimeter with a resolution of 0.02285 nm, and grating (3) had 600 groves per millimeter with a resolution of 0.07 nm at 435.8 nm. The CCD camera used in this experiment was an Apogee, Model SPH5-Hamamatsu S7030-1007, Back-Illum with a pixel array of 1024 $\times$ 122 and a pixel size of 24 microns. The line shapes and band intensities needed for evaluation of the gas and electron temperatures and electron density were obtained by integrating over 10 to 1000 pulses. All spectral measurements were performed side-on with respect to the direction of the flow, see Fig. 10. Small windows were constructed in the side of the cavity to allow for diagnostic measurements to be made.

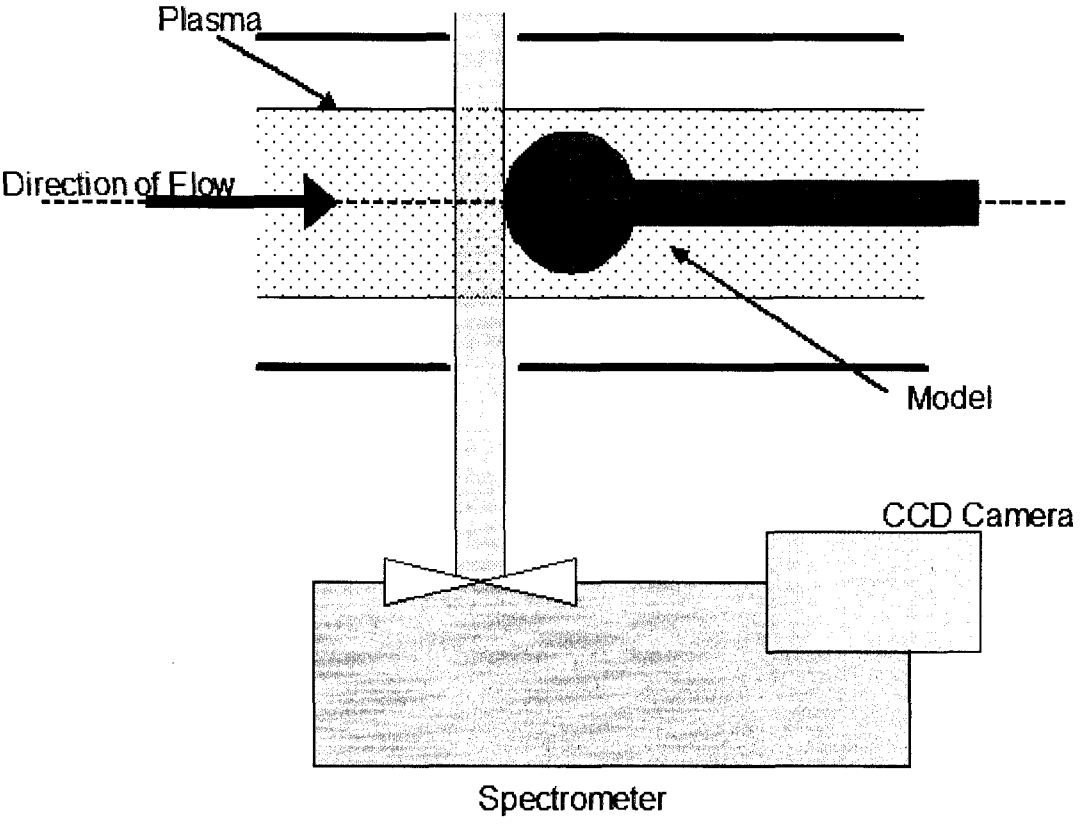

FIG. 10: Schematic of the optical emission spectroscopy set-up.

II.2.2 Blackbody Calibration of Spectra

Using a blackbody source, calibration curves were calculated for each grating of the spectrometer. For this calibration we used the Spectra-Physics Quartz Tungsten Halogen Lamp (model 63350), which has a predefined relationship between the wavelength (λ) and the irradiance (I),

$$I = \lambda^{-5} e^{A+\frac{B}{\lambda}} \left(C + \frac{D}{\lambda} + \frac{E}{\lambda^2} + \frac{F}{\lambda^3} + \frac{G}{\lambda^4} \right), \tag{20}$$

where the coefficents are given by
A = 41.85337541901
B = -4899.97859767823
C = 0.821306420331086
D = 428.610013779565
E = -317020.290823792
F = 85820275.9042372
G = -8493841443.25663.

We measured the number of counts for wavelengths between 250-1000 nm using the spectrometer and CCD camera. Then we determined an estimate of the irradiance per count [mW/m^2(nm)counts] for each grating by dividing the irradiance calculated by Eq. (20) with the number of counts. Fig. 11 shows data for the irradiance per count for grating (1). Corresponding graphs were obtained for gratings (2) and (3).

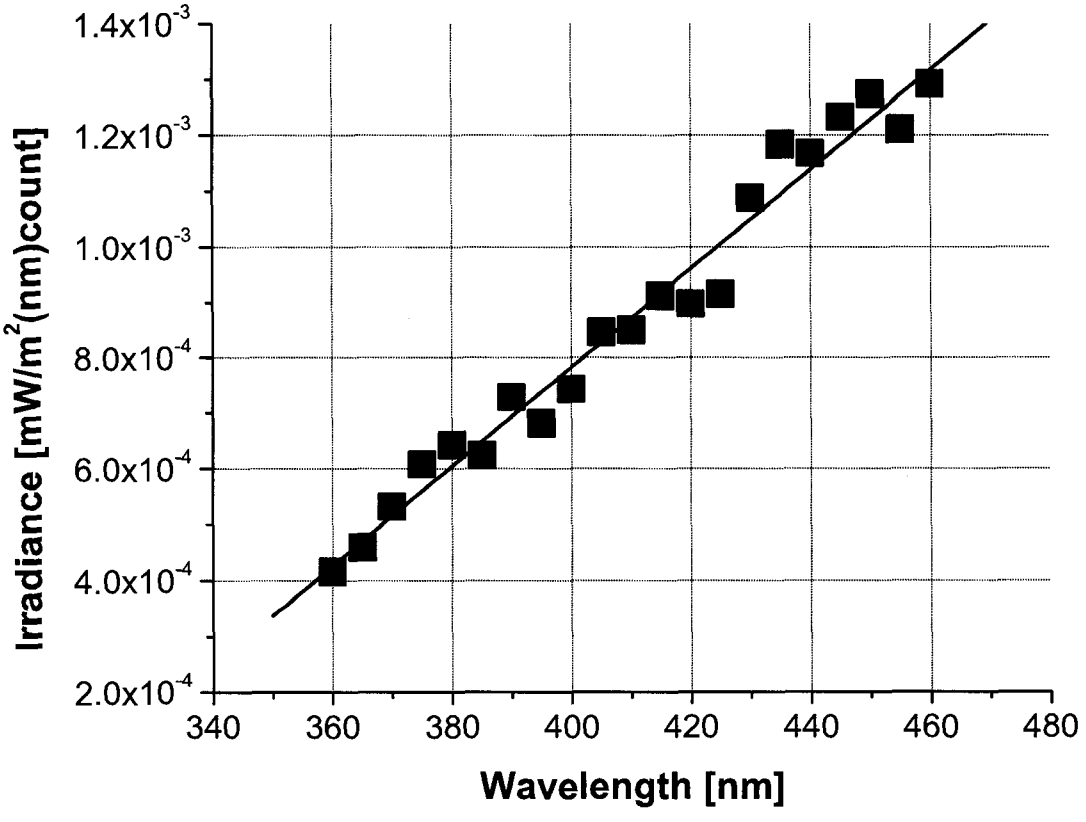

FIG. 11: Irradiance per count for grating 1 as a function of the wavelength.

II.2.3 Discharge Stability

It is important to understand the stability of a discharge in order to completely characterize it. To study the plasma stability we used a home-made photomultiplier tube (PMT) detector attached to a Tektronix TDS 340 A two channel digital real-time oscilloscope. A 796.2 nm interference filter was placed between the PMT and the microwave cavity to allow intensity measurement of Ar I lines around this wavelength.

Fig. 12, shows that the discharge stabilizes after about 13 s after the power to the magnetron is turned on. After 13 s we observe that there is jitter in the data. Analyzing this jitter we determined that on average the jitter is constant through time and thus can be effectively canceled from the results obtained in the latter part of this thesis. To take the measurements for data presented in II.3, we waited at least 15 s after ignition.

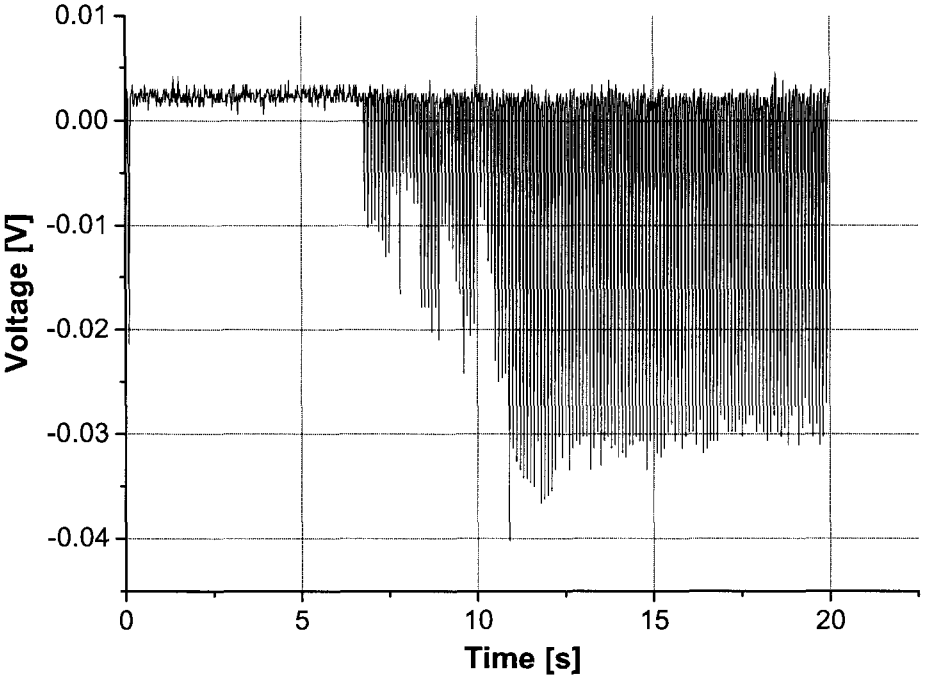

FIG. 12: PMT signal intensity as a function of time in a pure Ar discharge.

II.3 MEASUREMENTS

The specific feature of the supersonic flowing discharge is that heavy particles have flow-directed velocities comparable in magnitude to their thermal velocities [18]. This leads to substantial drift of excited particles downstream of the microwave cavity. In order to account for possible effects caused by drifting of excited species, one has to determine the rotational, vibrational, and electron temperatures as well as the electron density in the discharge. These parameters constitute the characterization of a supersonic flowing discharge.

II.3.1 Population of Argon Excited States

It has been observed [37, 13, 14] that there is an increase in radiation from the electronically excited states across the shock layer. Therefore measurements of these excited state populations, when the spherical blunt body is present, can be an indicator of a shock front in a supersonic discharge. To determine the population, we measured the intensity of each spectral line and multiplied by the irradiance per count for that wavelength from the black body calibrations presented in section II.2.2. We then obtained the irradiance of that particular spectral line in units of [mW/m^2(nm)]. In the next step we divided our result with the length of the plasma region (about 2 cm) and expressed the irradiance (P_λ) in terms of radiometric quantities [W/cm^3(nm)]. Further, we converted from radiometric to photonic quantities by using

$$\frac{dN_p}{dt} = P_\lambda \cdot \lambda \cdot 5.03 \times 10^{15} \left[\frac{\text{ph}}{\text{cm}^3 \cdot \text{s}}\right]. \tag{21}$$

Finally, we were able to calculate the population (N_u) by using

$$N_u = \frac{dN_p/dt}{A_{ul} \cdot g_u} \left[\frac{1}{\text{cm}^3}\right] \tag{22}$$

where A_{ul} is the transition probability and g_u is the statistical weight of the upper excited state.

In Fig. 13 is shown the population of observed Ar excited states in a free flowing discharge. By comparing the population values with a Boltzmann plot (straight line), we found that the population of the higher energy levels was lower then the

lower energy levels. We also observed that the rate of the decrease is higher for higher microwave powers. In addition, we observed how the populations varied with the amount of H_2 in the discharge. From Fig. 14, we see that the overall effect of adding the hydrogen to the discharge is to decrease the population of excited states. This effect is a direct result of ionization loss in the discharge due to electron-ion recombination [8].

We also measured the populations of the 4s-4p states of Ar varied in front of our model in a discharge at a power density of 0.865 W/cm^3 and a pressure of 3.3 Torr and present these results in Fig. 15 for the $2p_{10}$-$1s_5$ Ar I transition at 912.3 nm. We observe that both in the pure Ar and in the Ar with 5% H_2 the populations increased significantly when the model was added to discharge. However, there is no clear variation in the populations in front of model indicating that the shock may be too weak to observe at these pressures. Similar results were observed at 7.2 Torr and for higher energy transitions, such as 4p-5d, 4p-6s, and 4p-5s.

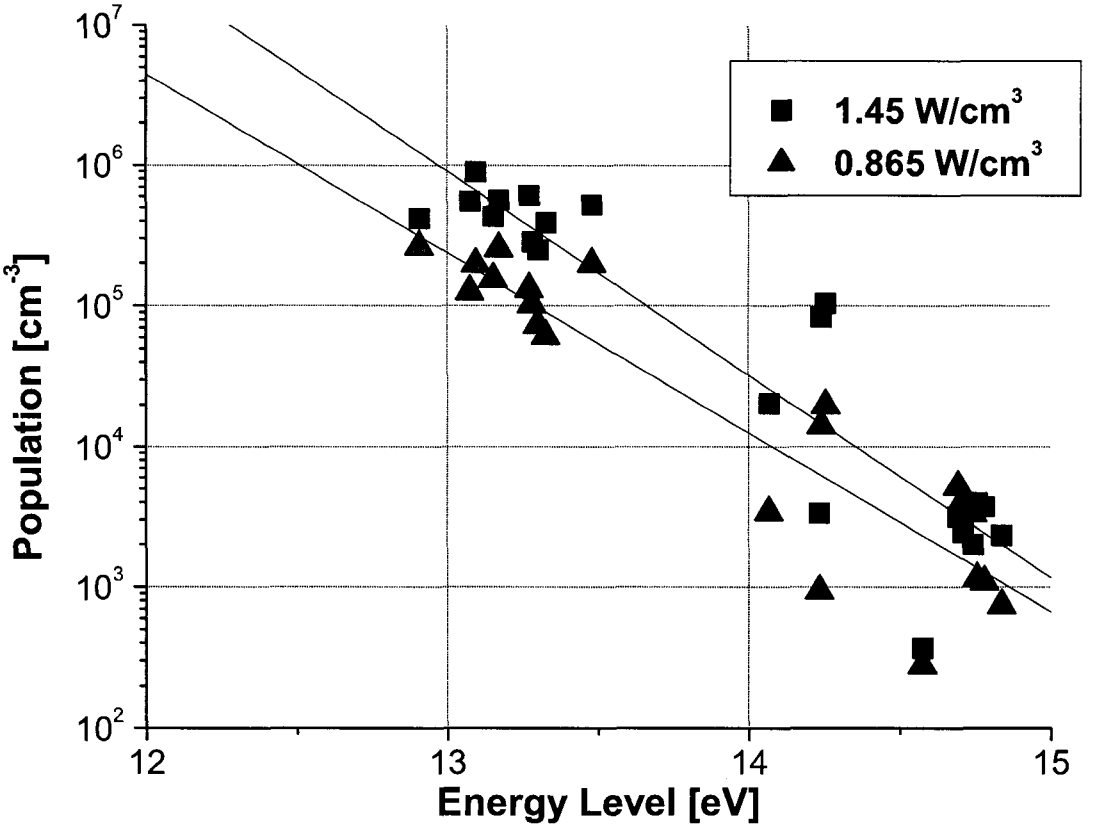

FIG. 13: Population of the Ar I lines as a function of the energy for an Ar discharge operated at a pressure of 2.5 Torr and two different power densities.

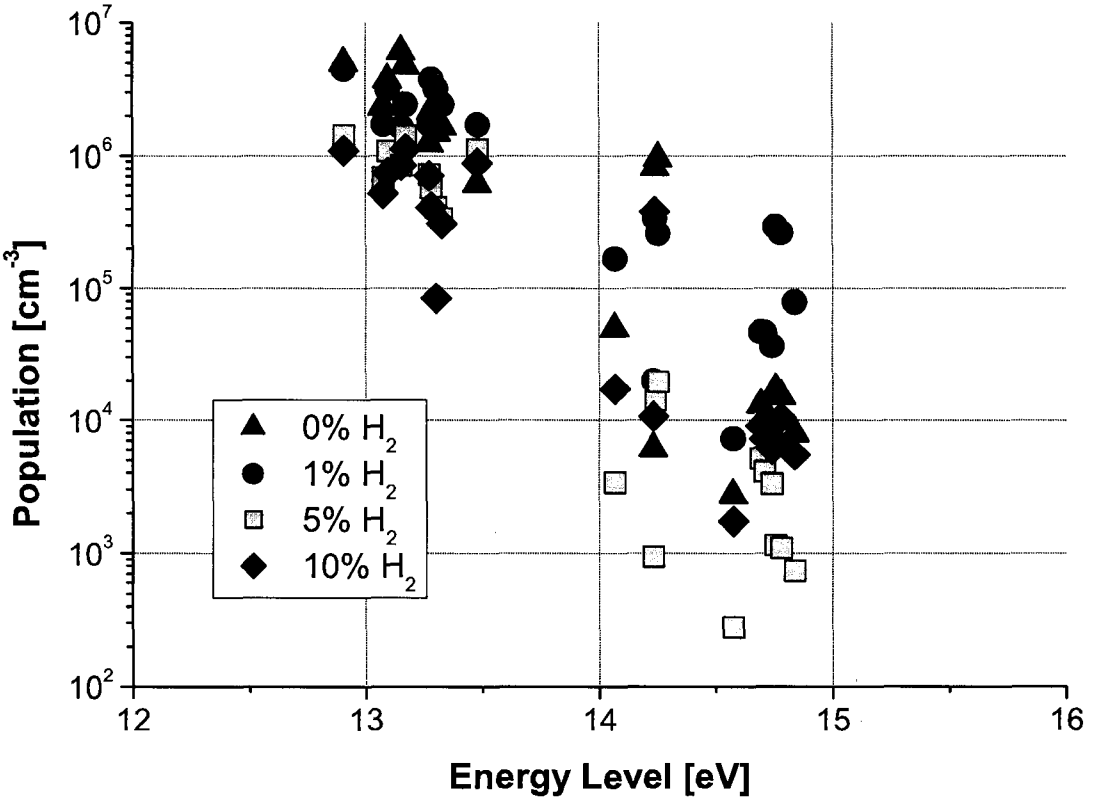

FIG. 14: Population of the Ar excited states in an Ar discharge as a function of the energy. Data are shown for different amounts of H_2 in the mixture.

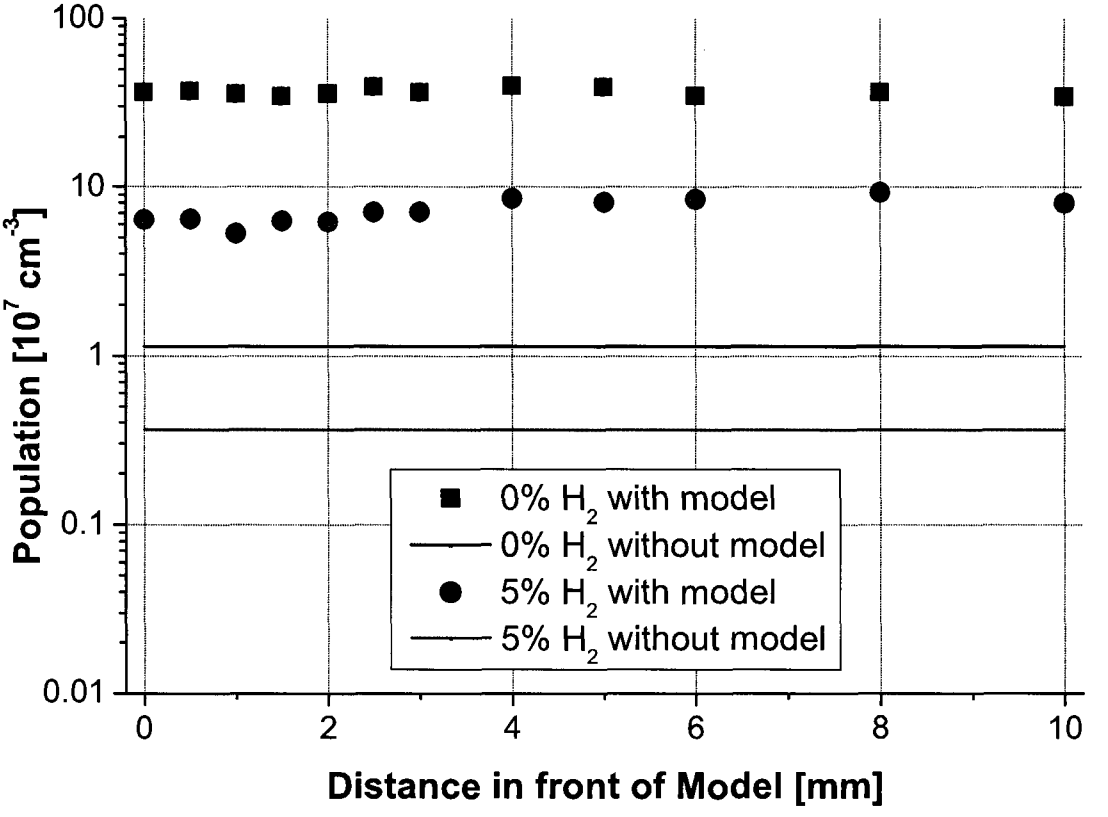

FIG. 15: Axial distribution of the Ar I $2p_{10}$ state population in front of the spherical model at 2.3 Torr. Data were taken from the intensity of 912.3 nm transition with different amounts of H_2 in the mixture.

II.3.2 Rotational Temperature

The rotational temperature of the constituent molecules in a gas discharge is the closest substitute to the gas-kinetic temperature, which is the quantity needed to characterize thermal motion of the bulk, ground state neutrals. We have accepted a common assumption that the rotational temperature of molecules in the discharge is equivalent to the gas temperature if the molecular excited states are produced by direct electron excitation from the ground state [5].

In air and nitrogen discharges, the N_2 second positive system is the most commonly used system for determination of the rotational temperature since it can easily be identified in an emission spectra and it has a large oscillator strength [38]. For carbon dioxide mixtures, the CO rotational system is used since it has a well-defined electric dipole moment and a relatively strong band emission intensity.

Nitrogen Rotational Systems

We have chosen to use the N_2 $C^3\Pi_u$ - $B^3\Pi_g$ second positive system, which ranges from the ultraviolet (280.0 nm) to the visible (492.0 nm) part of the spectra, to determine the rotational temperature. From Fig. 16, we observed that there are many rotational transitions in each vibrational band. For the second positive system, the rotational spectrum consists of three branches: P, Q, and R. The triplet splitting of the rotational quantum number (J) in both states causes the P and R branches to be split into three sub-branches and the Q branch into two [28].

We have chosen to use the $\Delta = 2$ system with a band head at 380.5 nm, since there is minimal self absorption and there is no interference from other atomic lines or molecular bands. Self absorption occurs when light emitted by the N_2 molecule from the interior of plasma passes through and is absorbed by N_2 molecules near the exterior of the plasma. Thus the emitted light intensity will be weaker and the effect can vary for different spectral lines [39].

For any multiplet vibrational system, the rotational components, $F_{\Omega,J}$ ($\Omega = 0, 1, 2$), can be determined from the semi-empirical formulas [6]

$$\begin{aligned} F_{0,J} &= B_v[J(J+1) - Z_1^{1/2} - 2Z_2] - D_v\left(J - \frac{1}{2}\right)^4 \\ F_{1,J} &= B_v[J(J+1) - 4Z_2] - D_v\left(J + \frac{1}{2}\right)^4 \\ F_{2,J} &= B_v[J(J+1) + Z_1^{1/2} - 2Z_2] - D_v\left(J + \frac{3}{2}\right)^4 \end{aligned} \tag{23}$$

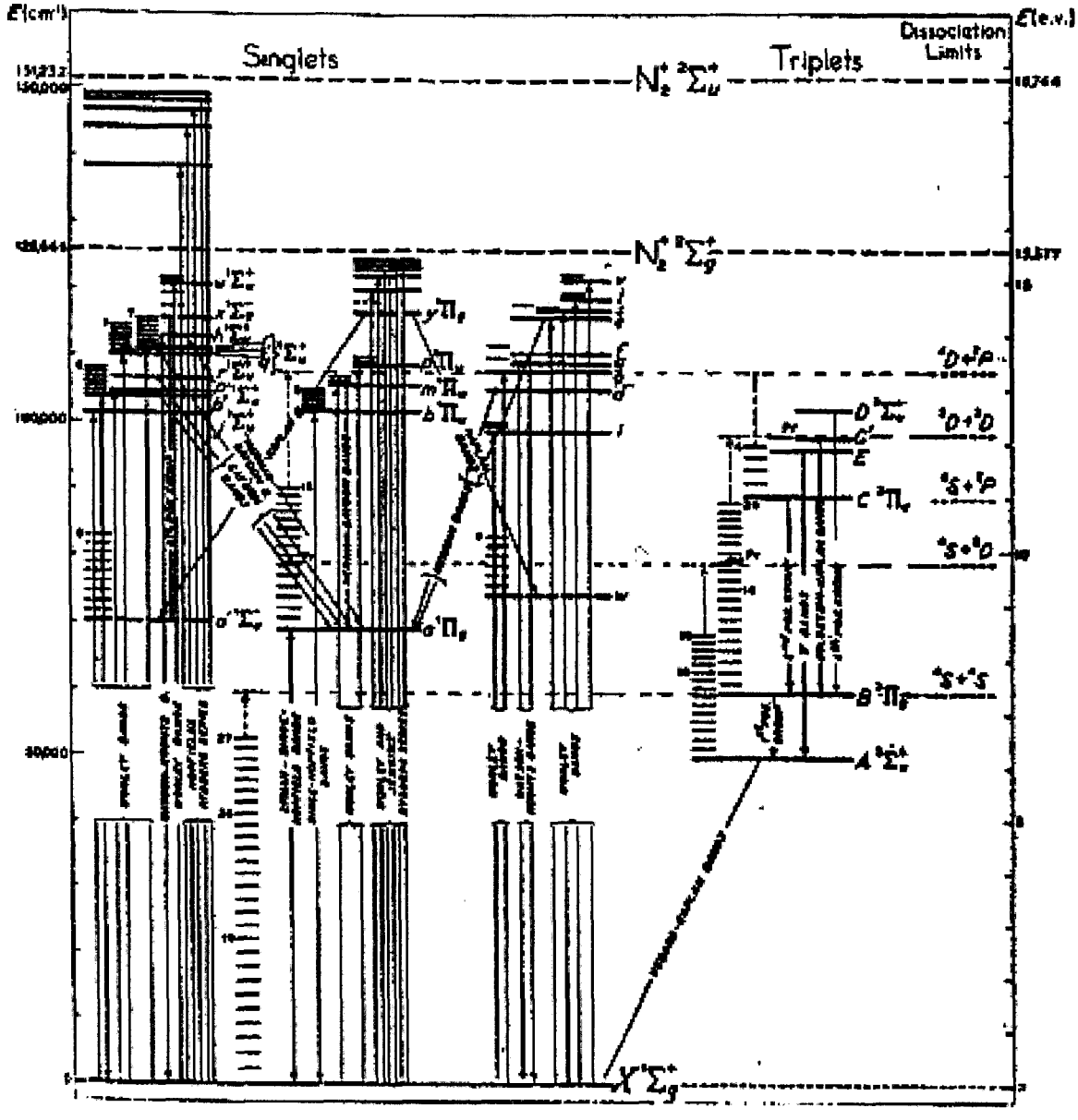

FIG. 16: Energy level diagram of N_2 [40].

where B_v and D_v are the rotational constants, Y_v is the spin-axis coupling constant listed in Table 1, and

$$\begin{aligned} Z_1 &= Y_v(Y_v - 4) + \frac{4}{3} + 4J(J+1) \\ Z_2 &= \frac{1}{3Z_1}[Y_v(Y_v - 1) - \frac{4}{9} - 2J(J+1)]. \end{aligned}$$

TABLE 1: N_2 rotational term constants [6].

	$C^3\Pi_u$			$B^3\Pi_g$		
v	B_v	Y_v	$D_v \times 10^6$	B_v	Y_v	$D_v \times 10^6$
0	1.8149	21.5	6.7	1.62849	25.9	6.4
1	1.7933	21.5	6.8	1.61047	26.2	6.5
2	1.7694	21.4	7.3	1.59218	26.4	6.7
3	1.7404	21.1	8.5	1.57365	26.8	6.8
4	1.6999	20.3	12.5	1.55509	27.0	6.9
5	–	–	–	1.53676	27.3	7.0
6	–	–	–	1.51787	27.6	7.2
7	–	–	–	1.49896	27.9	7.3
8	–	–	–	1.47940	28.2	7.5
9	–	–	–	1.46016	28.5	7.7
10	–	–	–	1.44124	28.8	8.0

The wavenumbers of the rotational lines for a band $v' - v''$ are then obtained from

$$\begin{aligned} &\text{P branches}: \quad v^P_{\Omega,J} = F'_{\Omega,J-1} - F''_{\Omega,J} \\ &\text{Q branches}: \quad v^Q_{\Omega,J} = F'_{\Omega,J} - F''_{\Omega,J} \\ &\text{R branches}: \quad v^R_{\Omega,J} = F'_{\Omega,J+1} - F''_{\Omega,J} \end{aligned} \tag{24}$$

where v_0 is the band head for the system, F' and F'' are the multiplet terms for the upper and lower levels, respectively, and J is the rotational quantum number of lower level v''. For the $C^3\Pi_u$ - $B^3\Pi_g$(0-2) system, v_0 is 26281.2 cm^{-1}. From the previous set of equations, we calculated the Fortrat diagram for the N_2 (0-2) system and presented in Fig. 17. From this figure, the rotational bands associated with specific quantum numbers can be identified.

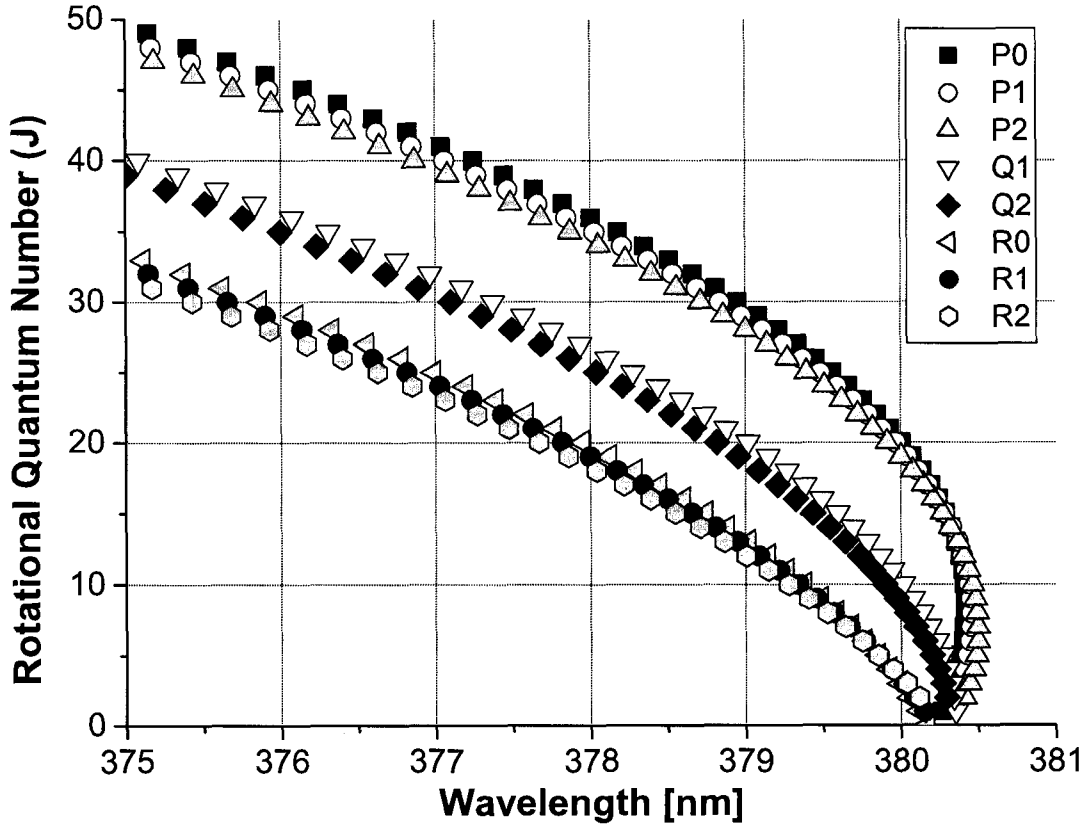

FIG. 17: Fortat diagram for the N_2 (0-2) band of the $C^3\Pi_u$ - $B^3\Pi_g$ system.

As mentioned previously, the rotational temperature is equivalent to the gas temperature if the molecularly excited states are produced by direct electron excitation from the ground state. For the N_2 system, this means that the $C^3\Pi_u$ level is populated by excitation from the ground state level $X^1\Sigma_g^+$. The distribution is assumed to be unchanged by the excitation from the ground state. It was assumed that the population distribution of the $C^3\Pi_u$ level is the same as in the ground state at a particular rotational temperature (T_r) [6]. appliying the Boltzmann law to the ground state, the population distribution term, $f_{J'}$, of the $C^3\Pi_u$ state for any v' is

$$f_{J'} = (2J'+1)\exp\left(-J'(J'+1)\frac{hcB_x}{k_B T_r}\right). \tag{25}$$

Here J' is the rotational number of the excited state, h is Plank's constant, c is the speed of light, B_x is the rotational constant for the ground state (1.9898 cm^{-1}), and k_B is the Boltzmann constant. Dividing $f_{J'}$ by the partition function

$$Q_r = \sum_{J'} f_{J'}, \tag{26}$$

we find the normalized population, $P_{J'}$,

$$P_{J'} = \frac{f_{J'}}{Q_r} = \frac{(2J'+1)}{Q_r}\exp\left(-J'(J'+1)\frac{hcB_x}{k_B T_r}\right). \tag{27}$$

The line strengths (Hönl-London factors) for the P, Q, and R branches of the N_2 second positive system are given by

$$S^P_{\Omega,J'} = \frac{(J'+1+\Omega)(J'+1-\Omega)}{(J'+1)} \tag{28}$$

$$S^Q_{\Omega,J'} = \frac{(2J'+1)\Omega^2}{J'(J'+1)} \tag{29}$$

$$S^R_{\Omega,J'} = \frac{(J'+\Omega)(J'-\Omega)}{J'} \tag{30}$$

and obey the sum rule

$$\sum_{\Omega}(S^P_{\Omega,J'} + S^Q_{\Omega,J'} + S^R_{\Omega,J'}) = 2J'+1. \tag{31}$$

Combining Eqs. (25) to (31), we find the normalized intensity of any line for the branch i (where i = P, Q, or R) to be

$$I^i = S^i_{\Omega,J'} \frac{1}{Q_r} \exp\left(-J'(J'+1)\frac{hcB_x}{k_B T_r}\right). \tag{32}$$

Assuming a rotational temperature of 1500 K, we used Eq. (32) to plot the relative intensity of the P, Q, and R branches of the N_2 $C^3\Pi_u$ - $B^3\Pi_g$ (0-2) as function of the wavelength. From Fig. 18, we observe that at the higher wavelengths, which correspond to lower J' values, the P branch is dominant and at lower wavelengths the R branch is dominant.

As mentioned previously, self-absorption can be a serious problem in plasmas. For the N_2 rotational system, the lines with lower J' values will have more self-absorption then those at higher values. Taking this into account along with Figs. 17 and 18, we have determined that the R0 sub-branch is the most useful to calculate the rotational temperature.

By applying Eq. (32) with the line strength for the R0 sub-branch and the value for the partition function (Q_r) substituted in, we found the rotational temperature from an exponential fit of the normalized line intensity ($I/2J'+1$) versus $J'(J'+1)$, see Fig. 19. Statistical error bars are given for uncertainties in the intensity measurements. In Fig. 20, we show the rotational spectrum of the 380.5 nm band head for N_2 $C^3\Pi_u$ - $B^3\Pi_g$ (0-2) system.

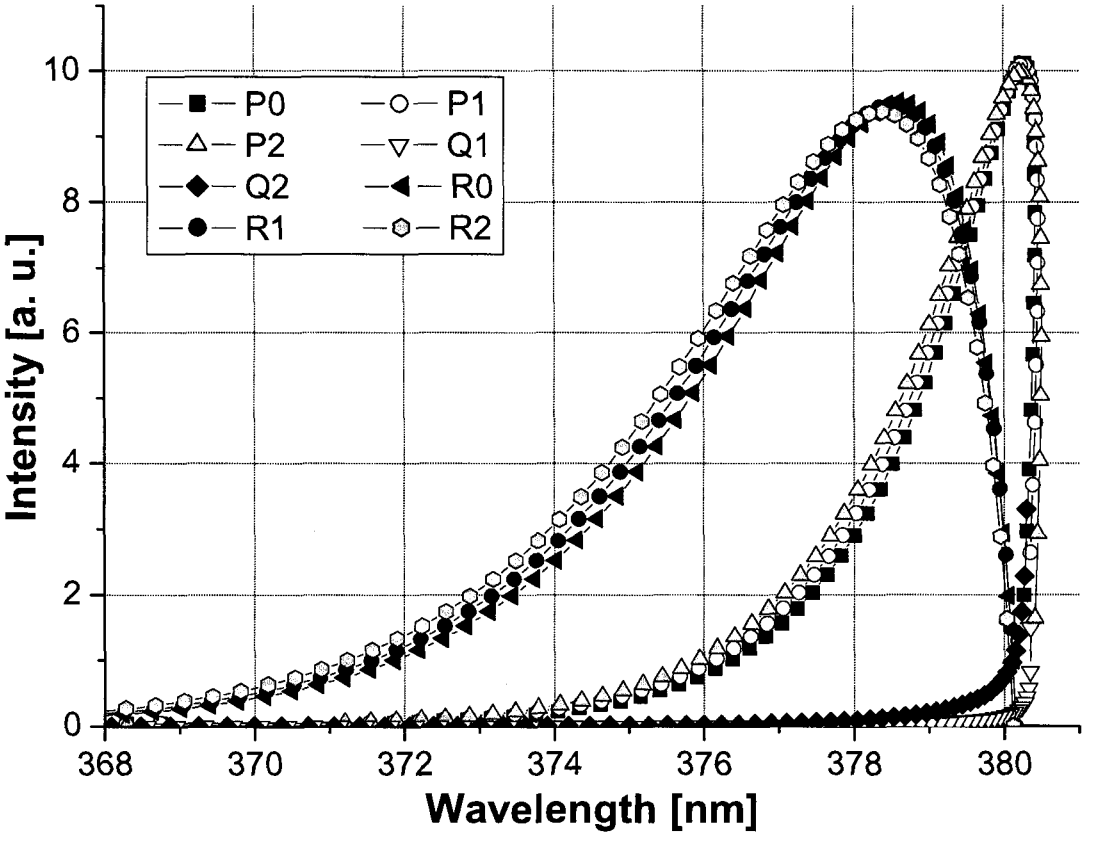

FIG. 18: Individual branch intensities of the N_2 $C^3\Pi_u$ - $B^3\Pi_g$ (0-2) for the band head at 380.5 nm and a temperature of 1500 K.

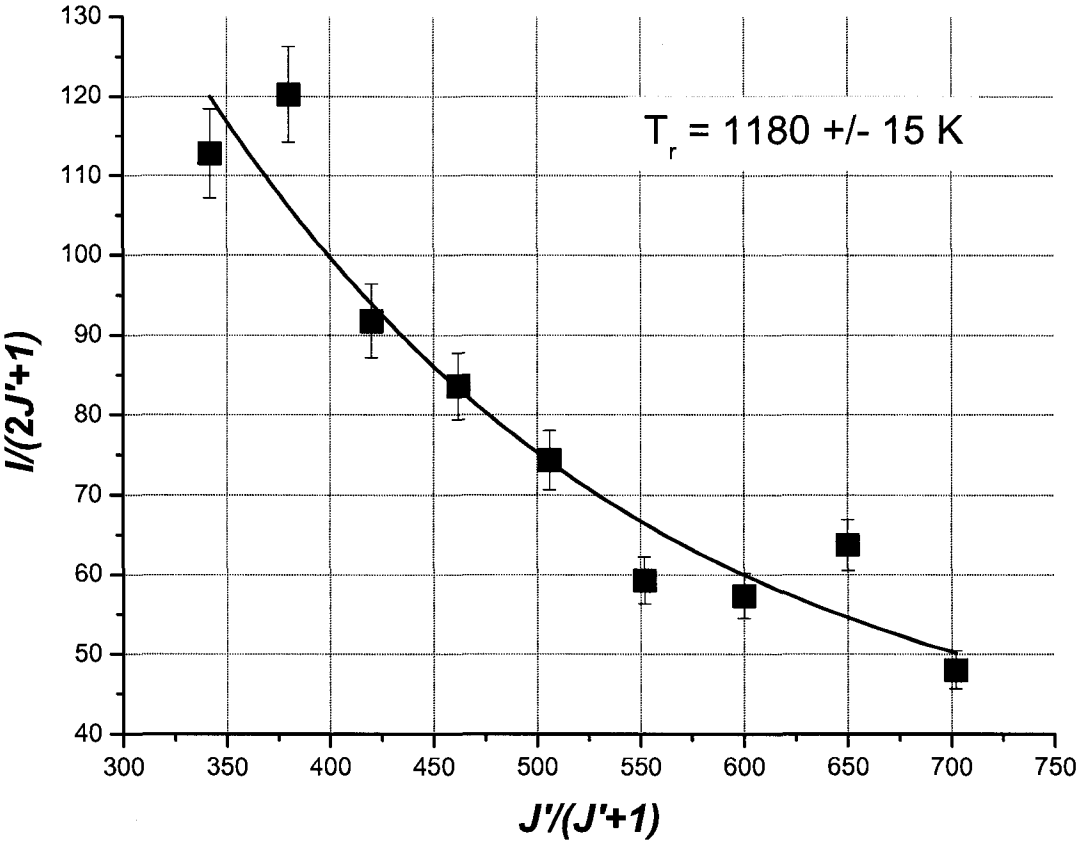

FIG. 19: Rotational temperature as determined from the exponential fitting of the intensity of the R0 sub-branch of N_2 (0-2) in a mixture of 86.55% Ar, 4.55% H_2, and 8.9% air at a pressure of 2.5 Torr and a power density of 1.15 W/cm^3.

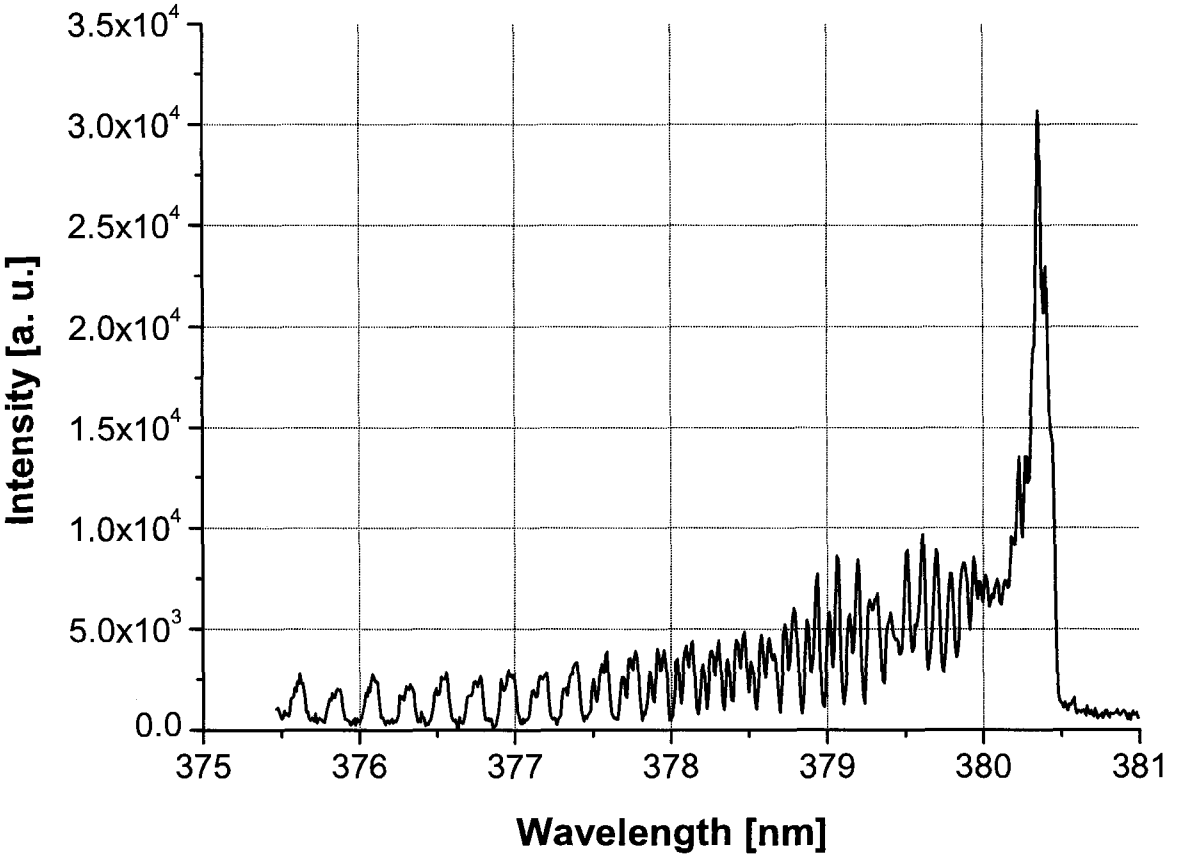

FIG. 20: Rotational spectrum for the N_2 $C^3\Pi_u$ - $B^3\Pi_g$ (0-2) band in a mixture of 86.55% Ar, 4.55% H_2, and 8.9% air at a pressure of 2.5 Torr and a power density of 1.15 W/cm^3.

The next parameter we considered is the pressure in the discharge region, inside the microwave cavity. From Fig. 21, we see that the rotational temperature varied little with the pressure.

We observed the change in the rotational temperature when 0%, 1%, 5%, and 10% H_2 was added to an Ar discharge. We also estimated how the amount of air in the system would affect these types of discharges. We measured the N_2 $C^3\Pi_u$ - $B^3\Pi_g$ (0-2) second positive system and found that the rotational temperature decreased with increasing amounts of air and H_2 in the discharge (see Fig. 22). After careful measurements we determined that the value of a pure air discharge was 910 $\pm$ 50 K. The high value of the rotational temperature when small amounts of air and H_2 were in the discharge and the results for the pure air discharge indicate that the decrease observed in Fig. 22 is an artifact of the mixing of the four species in the gas (Ar, H_2, N_2, and O_2).

Finally, we observed how the rotational temperature varied with the power density in discharges of 93.55% Ar, 1% H_2, and 5.45% air and 89.85% Ar, 4.7% H_2, and 5.45% air. From Fig. 23, we observe that the rotational temperature increased with increasing power with the average temperature increasing by nearly 150 K.

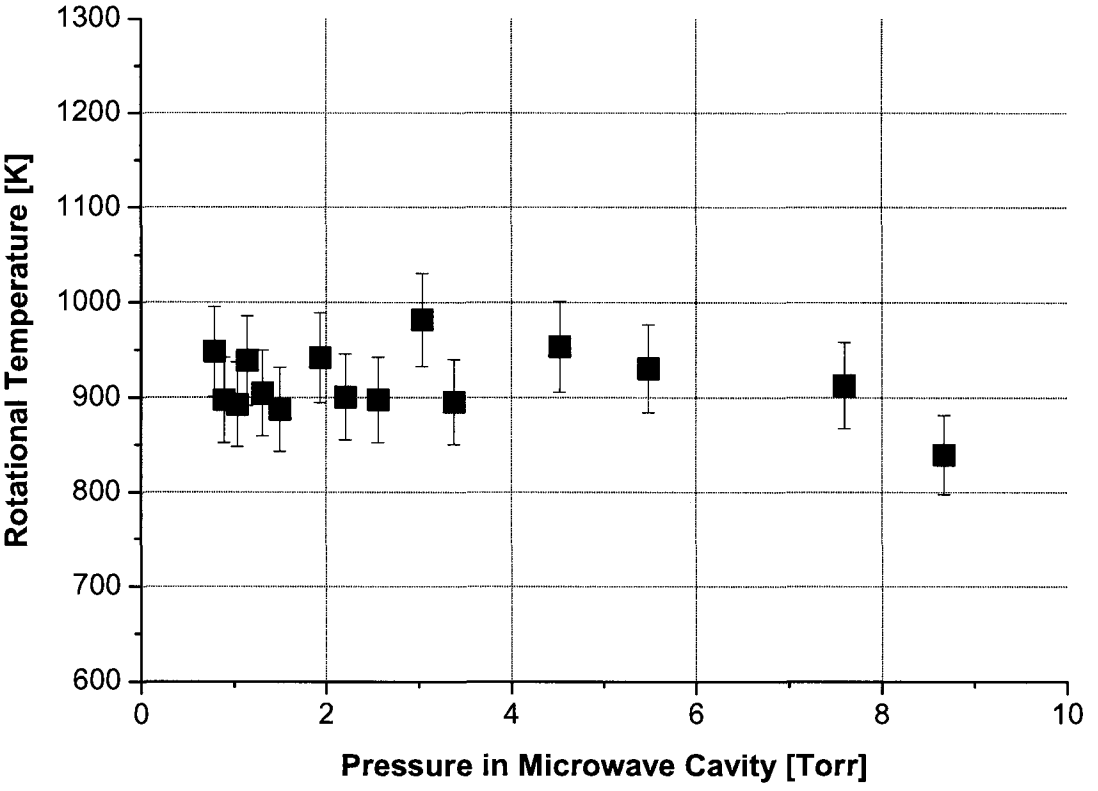

FIG. 21: Rotational temperature as function of the pressure in the microwave cavity region for a mixture of 68.4% Ar, 3.6% H_2, and 28.1% air at a power density of 1.15 W/cm^3.

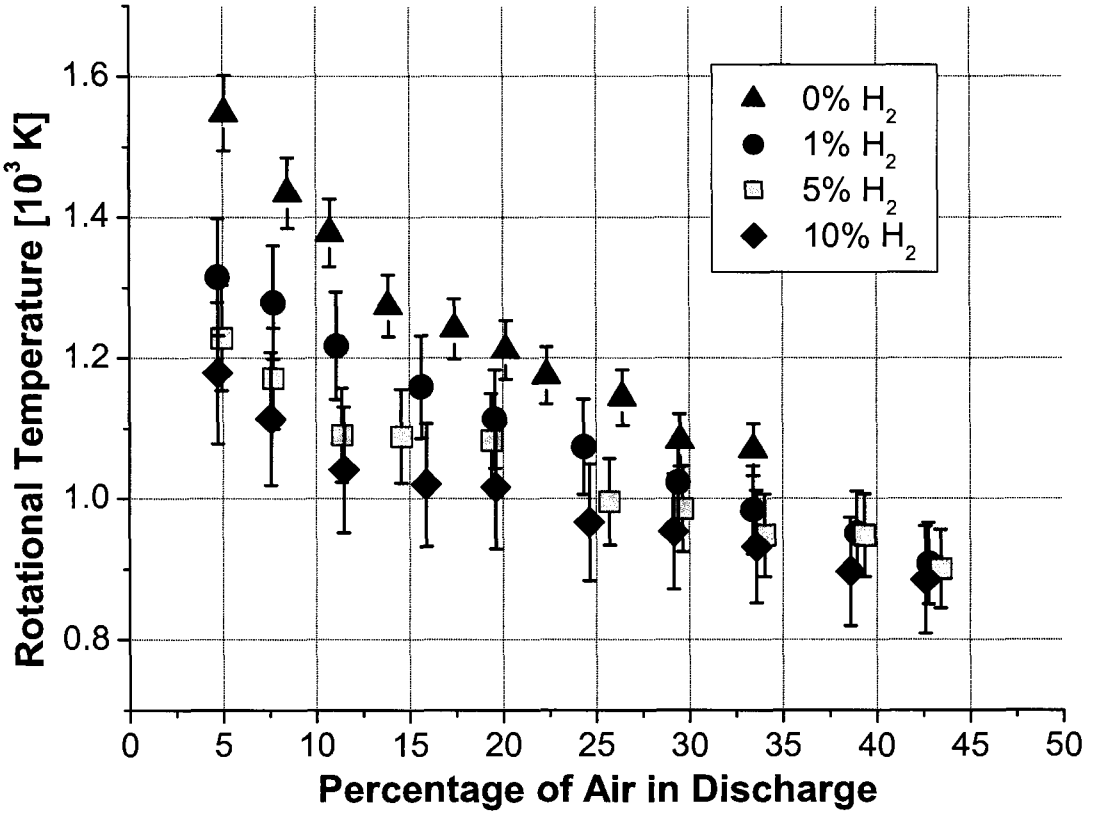

FIG. 22: Rotational temperature as a function of the percentage of H_2 and air in the discharge [18] at a pressure of 2.3 Torr and a power density of 1.15 W/cm^3. Statistical error bars are indicated.

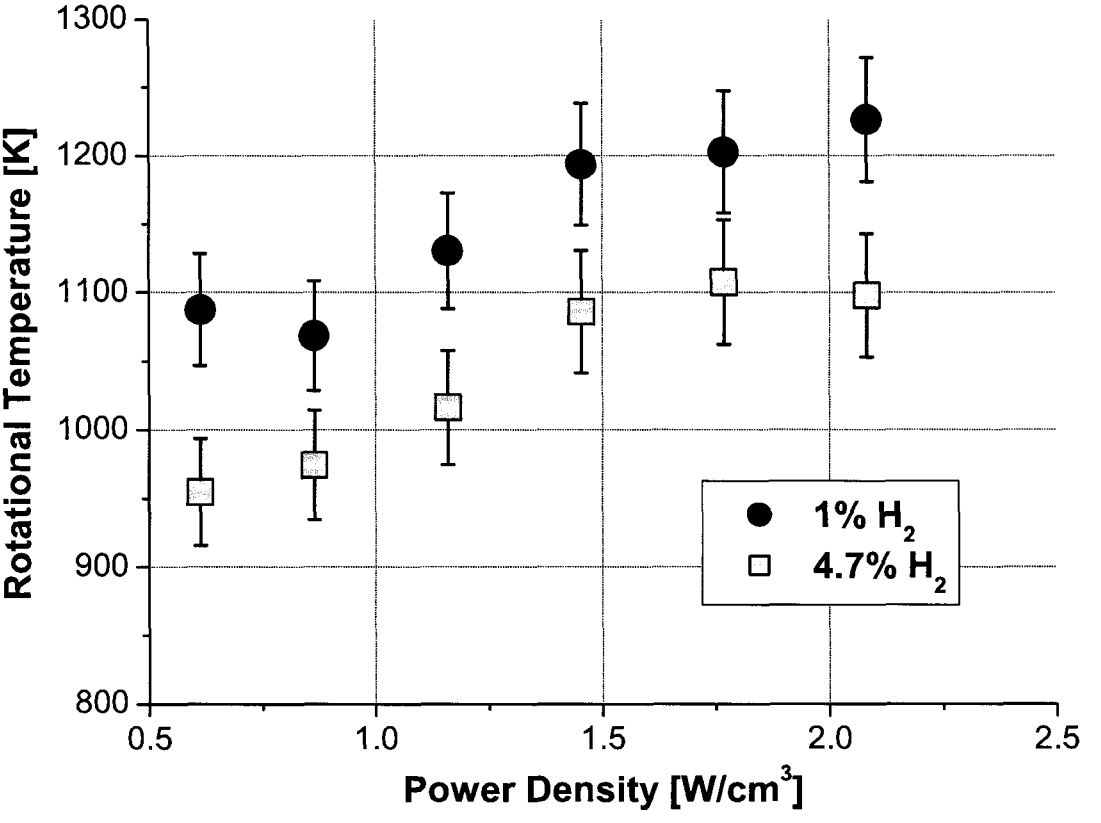

FIG. 23: Rotational temperature as a function of the power density at a pressure of 2.4 Torr. Statistical error bars are indicated.

Carbon Monoxide Rotational System

Ionization of our Martian simulated gas mixture causes the CO_2 to dissociate into CO and O. The rotational temperature can most easily be determined from the rotational bands of the CO ($B^1\Sigma^+ - A^1\Pi$) Ångstrom system. In a discharge the $B^1\Sigma^+$ state of CO is populated by direct electron excitation from the ground state [41]. Thus the rotational temperature can be assumed to be equivalent to the gas temperature. As in the case of N_2, there are many rotational transitions in each vibrational band for CO, see Fig. 24. In addition, these bands are split into three branches (P, Q, and R) due to the triplet splitting of the rotational quantum number J'.

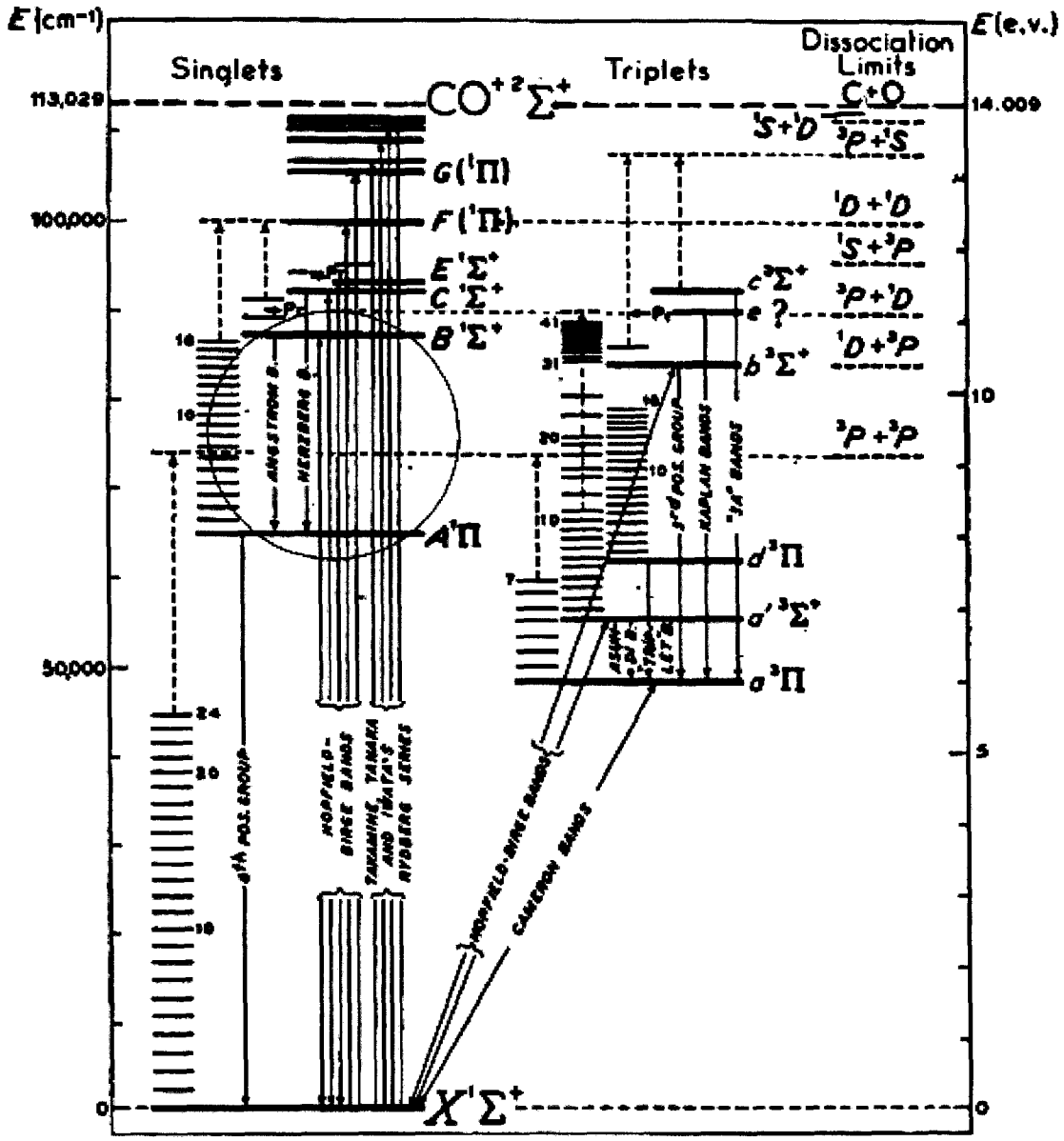

FIG. 24: Energy level diagram of CO [40].

Following the procedure outlined in Herzberg [40], the wavenumber for each of the branches can be determined accurately, including the second order corrections, for the rotational constants from

$$\begin{aligned} v_p &= v_0 - (B' + B'')J' + (B' - B'')J'^2 - (D' - D'')(J'^2 + 1)^2 J'^2 + 2(D' + D'')J^3 \\ v_q &= v_0 + (B' - B'')J' + (B' - B'')J'^2 - (D' - D'')(J' + 1)^2 J'^2 \\ v_r &= v_0 + 2B' + (3B' - B'')J' + (B' - B'')J'^2 - 4D'(J' + 1)^3 - \\ & \quad (D' - D'')(J' + 1)^2 J'^2. \end{aligned} \tag{33}$$

Here v_0 is the band head for the system (19240.3 cm^{-1}), B is the rotational constant for the first order correction, D is the rotational constant for the second order correction, and the single and double prime represent the upper and lower states, respectively. For the CO ($B^1\Sigma^+ - A^1\Pi$) Ångstrom system, the rotational constants are given in Table 2 [42].

TABLE 2: Constants for the CO ($B^1\Sigma^+ - A^1\Pi$) Ångstrom rotational system [42]. Here $B_v = B_e - \alpha_e(v + 12)$ and $D_v = D_e$.

$B^1\Sigma^+$		$A^1\Pi$	
B'_e	1.961	B''_e	1.6116
α'_e	0.027	α''_e	0.2229
D'_e	6.958E-06	D''_e	7.289E-06
$B'_{(v=0)}$	1.9475	$B''_{(v=2)}$	1.5558
$D'_{(v=0)}$	6.958E-06	$D''_{(v=2)}$	7.289E-06

Using Eq. (33), we plotted the rotational quantum number as a function of the wavelength and present these results in Fig. 25. From this figure, the rotational lines associated with specific quantum numbers can be identified, given the wavelength for each of the rotational lines.

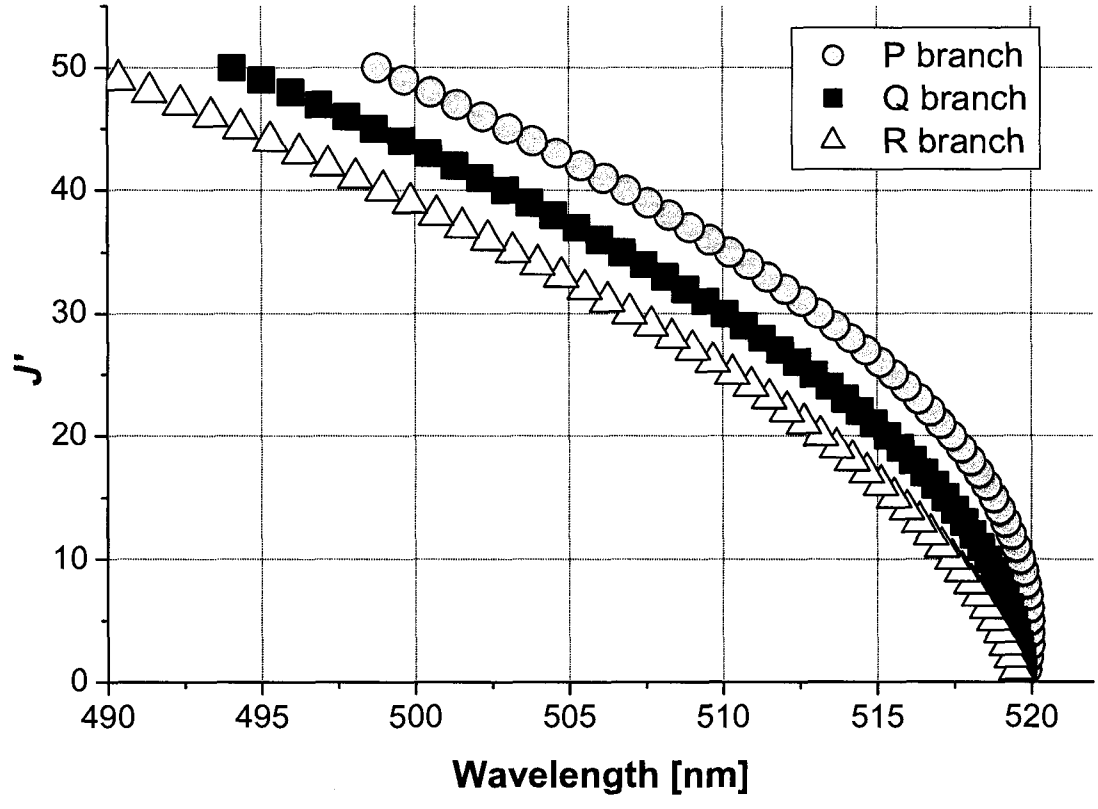

FIG. 25: Fortrat diagram of the CO (0-2) Ångstrom system for the $B^1\Sigma^+ - A^1\Pi$ state.

The relationship between the rotational temperature and the rotational quantum number J' [40] is given by

$$I(J') = \frac{2C_E\nu^4}{Q_r} S_{J'} \exp\left(-\frac{B'J'(J'+1)hc}{k_B T_e}\right). \tag{34}$$

Here C_E is a constant which depends on the change in the dipole moment and the total number of excited molecules, B' is the rotational constant listed in Table 2, and the line strengths for each of the branches ($S_{J'}$) are given by the Hönl-London factors [43]:

$$\begin{aligned} S_{J'}^{Q} &= \frac{2J+1}{4} \\ S_{J'}^{P} &= \frac{J}{4} \\ S_{J'}^{R} &= \frac{J+1}{4}. \end{aligned}$$

Assuming a rotational temperature of 300 K, we used Eq. (34) to plot the relative intensity of the P, Q, and R branches of the CO ($B^1\Sigma^+ - A^1\Pi$) system as function of the wavelength. From Fig. 26, we observe that the Q branch has a peak intensity twice that of the P or R branches. In Fig. 27, we show the rotational spectrum of the 519.8 nm band head for system.

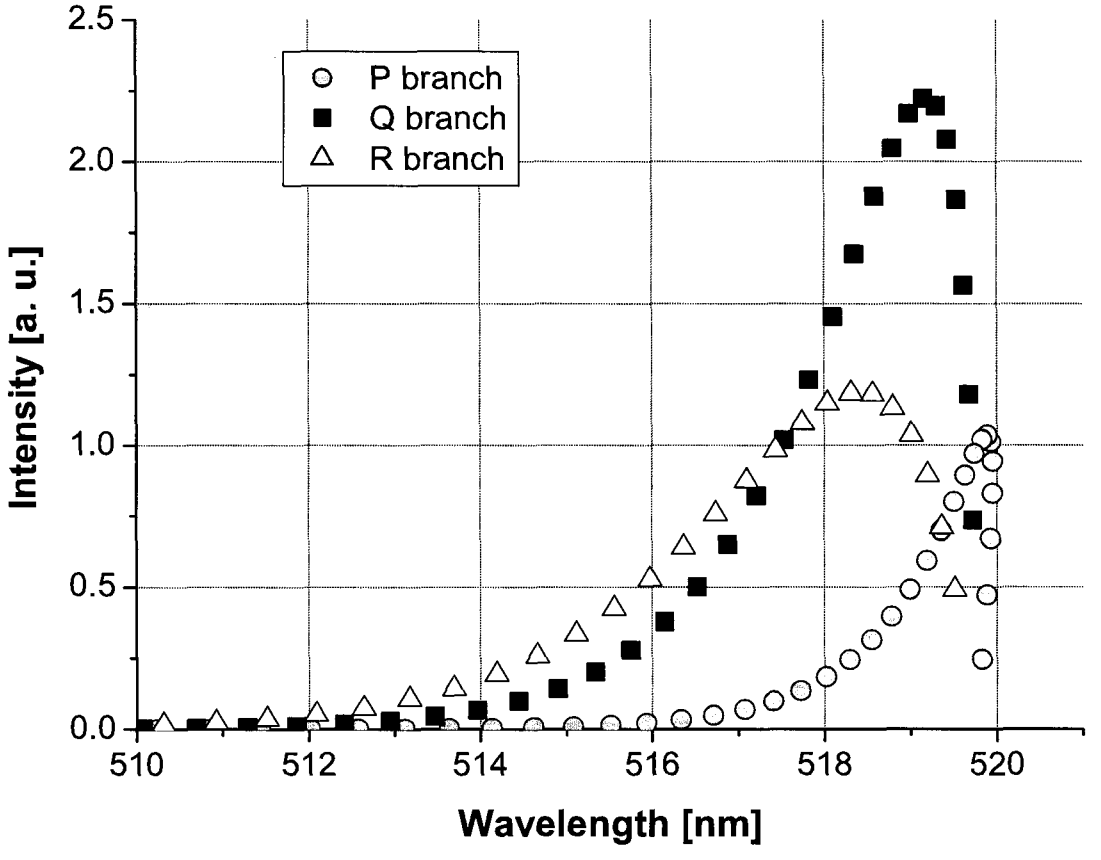

FIG. 26: Branch intensity distribution of the CO (0-2) Ångstrom system for the $B^1\Sigma^+ - A^1\Pi$ state at T = 300 K.

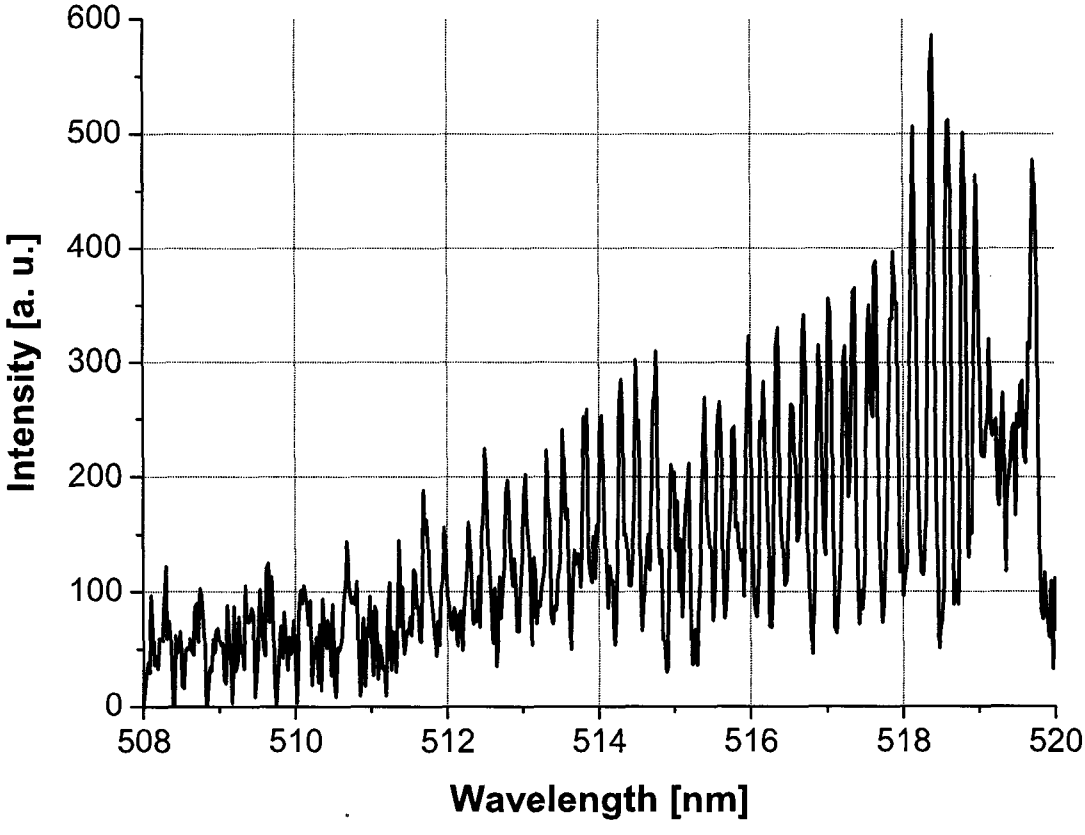

FIG. 27: Rotational spectrum of the CO $B^1\Sigma^+ - A^1\Pi$ (0-2) Ångstrom system.

To determine the rotational temperature, we employed Eq. (34) to our Martian simulated mixture. Results presented in Fig. 28 show that the rotational temperature did not vary greatly with the power density. We also observed that the rotational temperature was lower in the pure CO_2 discharge. Therefore we can say that the addition of Ar and N_2 to the discharge caused an increase in rotational temperature.

Another important thing to note is the difference in the rotational temperature for the $Ar/H_2/Air$ mixtures (see Fig. 22) and that of the Martian simulated mixture. In both mixtures, N_2, Ar, and O_2 are present, but in one of them there is H_2 and in the other CO, from the dissociation of CO_2. Therefore, this vast difference in rotational temperature between the mixtures correspond to the presence of H_2 or CO in discharge.

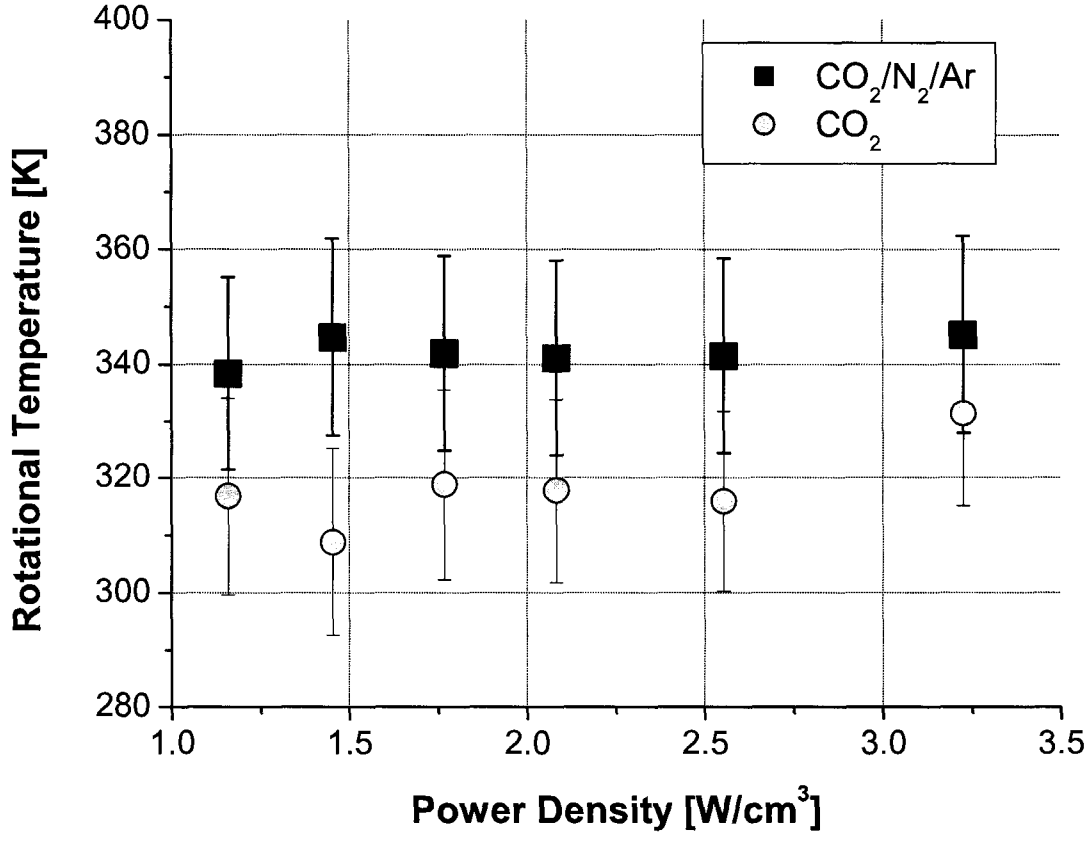

FIG. 28: Rotational temperature of the Martian simulated mixture and pure CO_2 as function of the power density at a pressure of 2.7 Torr. Statistical error bars are indicated.

II.3.3 Vibrational Temperature

In this research we are using two different complex molecular gases. The bonds between the atoms in different molecules can break at high vibrational energies (temperatures) which generates new species in the discharge. Thus, determination of vibrational temperature is important for detailed understanding of the physical and chemical properties of a discharge. For the $Ar/H_2/Air$ mixtures, we used the vibrational bands of the N_2 second positive system to determine the temperature. For the Martian simulated mixture, we used the ratio of the intensities of two vibrational transitions of the CO Ångstrom system.

Nitrogen Vibrational System

In Fig. 29 we show different vibrational bands of the N_2 second positive system. Self absorption is a problem for most of the N_2 bands. In addition, the presence of OH bands and Ar lines perturb some the N_2 bands. Thus, we have chosen to use the $\Delta = 2$ system for determination of the vibrational temperature since the self absoprtion will be minimal and there are not alot of other molecular bands or atomic lines around it. It is apparent from the figure that at higher J values, the intensity of the next band will be increased due to the presence of the previous band. As such, we determined that we must correct for this by extrapolating the intensities of lower v' bands over the whole series [18]. For instance, the intensity of the (1-3) band at 375.5 nm had to be decreased by the extrapolated intensity of the (0-2) band at 380.5 nm. For the (2-4) at 371.0 nm band both the (1-3) and the (0-2) band had to be included. In this manner, a much more accurate vibrational Boltzmann plot could be produced.

To determine the vibrational temperature, T_v, we assumed a Boltzmann distribution of the spectral line intensity, I,

$$I = C_1 A v(v') \exp\left(-G(v')\frac{hc}{k_B T_v}\right) \tag{35}$$

where C_1 is a fitted constant, A is the Frank-Condon factor, $v(v')$ is defined as

$$v(v') = \frac{2c\pi}{\lambda}, \tag{36}$$

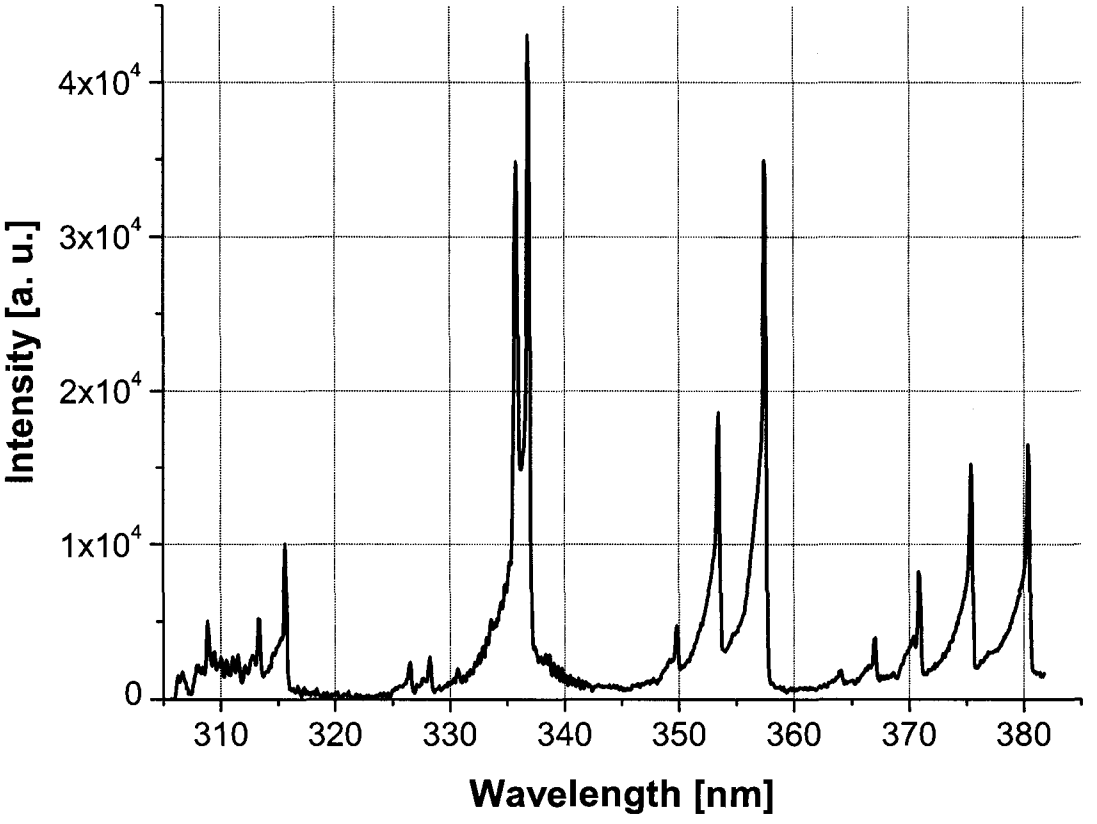

FIG. 29: Rotational-vibrational spectrum of the N_2 second positive system in a mixture of 86.55% Ar, 4.55% H_2, and 8.9% air at a pressure of 2.7 Torr and a power density of 0.85 W/cm^3.

and $G(v')$ is defined as

$$G(v') = w_e\left(v' + \frac{1}{2}\right) - w_e x_e\left(v' + \frac{1}{2}\right)^2 + w_e y_e\left(v' + \frac{1}{2}\right)^3 + w_e z_e\left(v' + \frac{1}{2}\right)^4. \quad (37)$$

Using the N_2 $\Delta = 2$ vibrational system, we determined the vibrational temperature. Specific constants for the $\Delta = 2$ vibrational system are presented in Table 3.

TABLE 3: Constants of the N_2 $\Delta = 2$ vibrational system [40].

λ [nm]	ν'	$A_{ki}[10^6\ s^{-1}]$	G(ν')
364.2	4	0.0518	6.633E+05
267.2	3	0.0868	6.103E+05
371.0	2	0.151	4.764E+05
375.5	1	0.185	2.987E+05
380.5	0	0.134	1.016E+05

The vibrational temperature was thus determined as a function of the amount of H_2 and air in the system (see Fig. 30). Although the amount of H_2 has little effect, we see in the graph that the amount of air in the system caused a decrease in the temperature. We determined, under the same experimental conditions, that the vibrational temperature of an air discharge was 5000 $\pm$ 300 K. This indicates that the observed decrease was primarily due to the mixing of the different gas species.

We also observed the vibrational temperature as a function of the power density in order to understand the power balance in the discharge. In Fig. 31 we see that at higher power densities the vibrational temperature decreases till it reaches a plateau at 1.4 W/cm^3. Observing the length of the plasma as the power was increased, we found that the discharge extended far outside of the microwave cavity. In fact, unlike in the case of the Martian mixture, the discharge covered the entire length of the tube from the edge of the cavity to the inlet for the roots blower/vacuum pump system. Thus, the power is dissipated over a larger area of flow at higher power densities causing this apparent decrease in temperature.

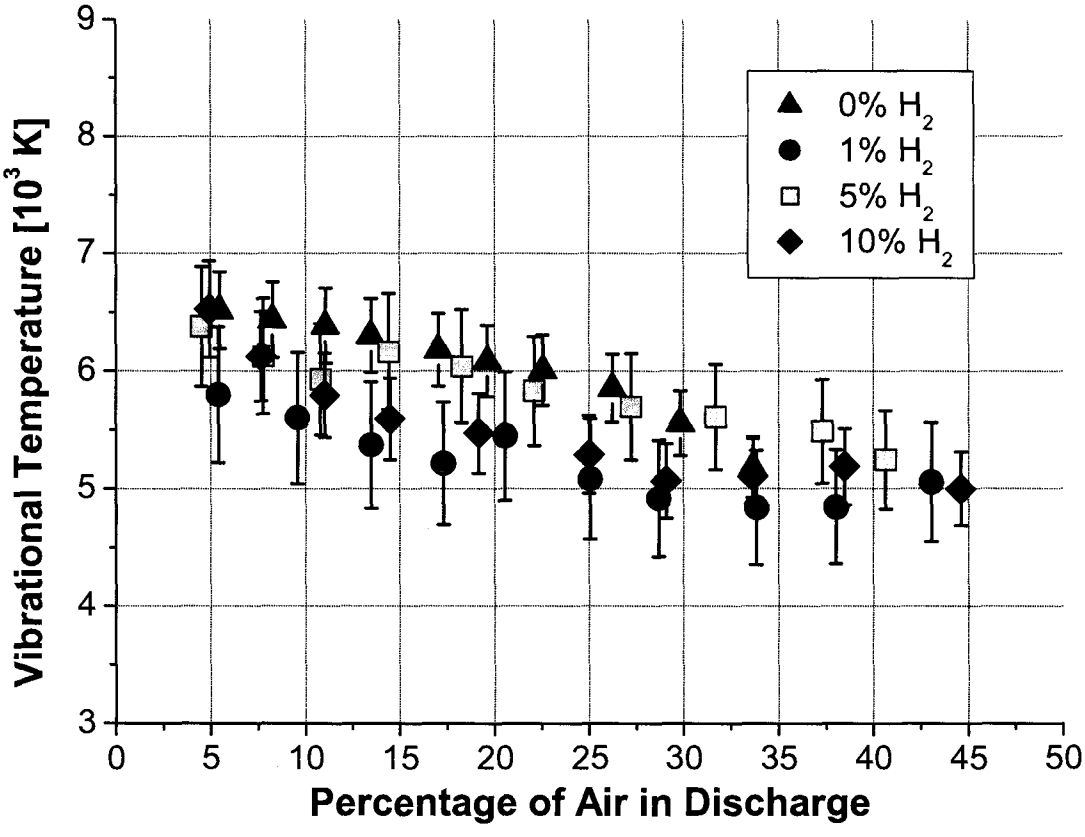

FIG. 30: Vibrational temperature as a function of the percentage of H_2 and air in the discharge at a power density of 0.85 W/cm^3 [18]. Statistical error bars are indicated.

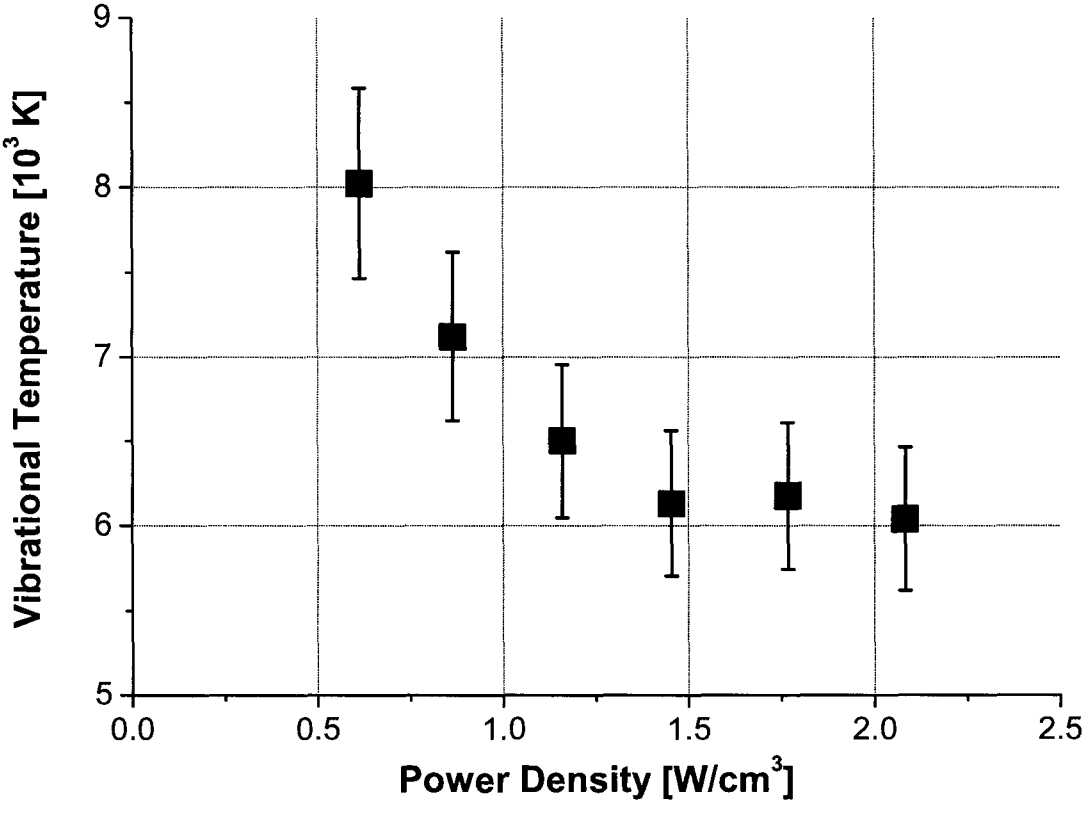

FIG. 31: Vibrational temperature as a function of the power density in a mixture of 86.55% Ar, 4.55% H_2, and 8.9% air at a pressure of 2.4 Torr.

Carbon Monoxide Vibrational System

As in the case of the rotational temperature, the vibrational temperature for our Martian simulated gas can be determined from the electron vibrational bands of the CO ($B^1\Sigma^+ - A^1\Pi$) Ångstrom system. Following the procedure outlined in Ref. [44], we determined the vibrational temperature from the ratio of the intensities of the vibrational levels 1 and 0 for the $B^1\Sigma^+$ state,

$$T_v = \Delta E_{10}[k_B \cdot \ln[(I_1/I_0)(\lambda_1^4/\lambda_0^4)(q_0/q_1)]]^{-1}. \tag{38}$$

Here ΔE_{10} is the energy of the vibrational quantum of the $X^1\Sigma$ state (0.2691 from Ref. [40]), I is the intensity, λ is the wavelength for the vibrational level in Ångstroms, and q is the Frank-Condon factor. Employing Eq. (38), we can determine the vibrational temperature of our mixture as a function of the power density (see Fig. 32). From this figure, we observe that the temperature is around 2600 K at low power densities and then decreases till it reaches a plateau at 1.75 W/cm^3. This is similar to the results of the Ar/H_2/Air mixture in the previous section. The decrease however is 300 K as opposed to 2000 K in the Ar/H_2/Air mixture. From analysis of the spectra, we found that this decrease at the lower values of the power denisty was due to a low signal to noise ratio. Therefore, the data at these lower power densities is less reliable.

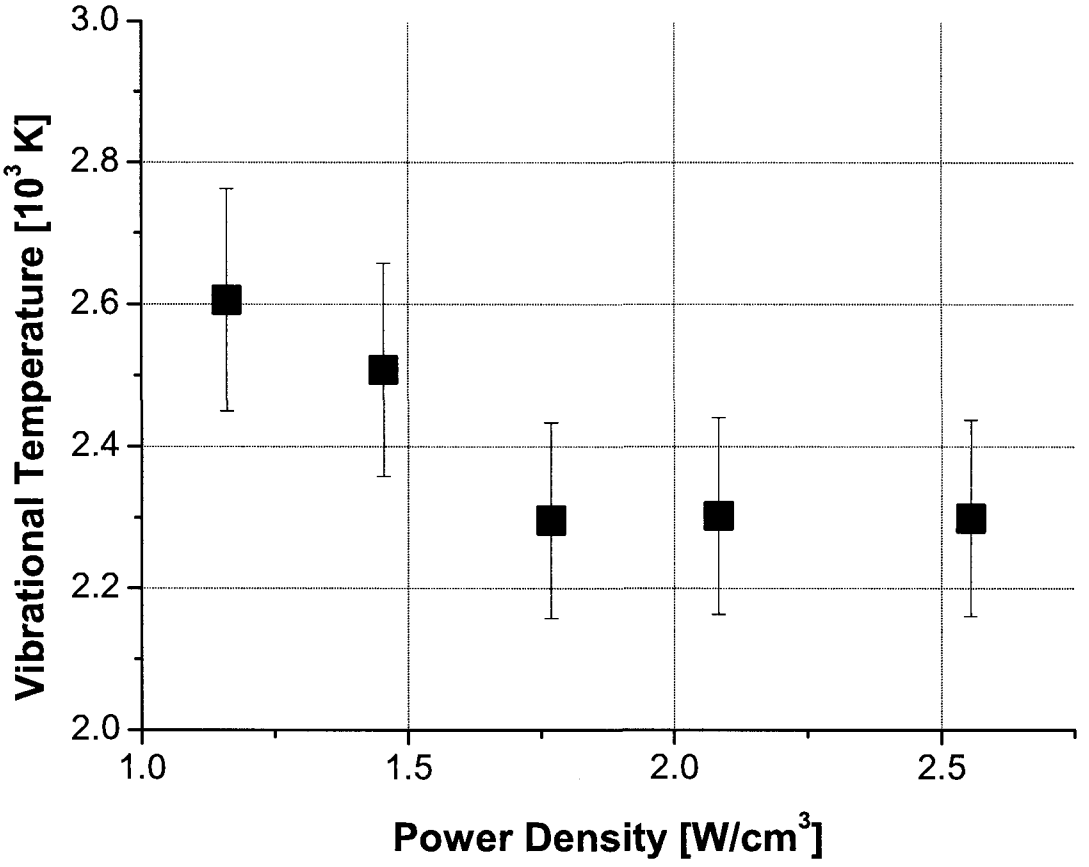

FIG. 32: Vibrational temperature as a function of the power density for the Martian simulated discharge at a pressure of 2.5 Torr.

II.3.4 Electron Excitation Temperature

The electron excitation temperature can be determined by a variety of spectroscopic techniques. However, the most common way is by the Boltzmann plot method, since it provides better accuracy [45]. In this method we assume that the intensities (I) of electronicly excited states having the same lower level energy but different threshold excitation energies (E_k) follow a Boltzmann distribution

$$I = \frac{A_{ki} g_k}{\lambda} \exp\left(-\frac{E_k}{k_B T_e}\right). \tag{39}$$

Here λ is the wavelength, A_{ki} is the transition probability, and g_k is the statistical weight of the upper level. By plotting $(I\lambda)/(A_{ki}g_k)$ versus the threshold excitation energies on a semilogarithmic plot the electron temperature can be determined from an exponential fitting of the experimental data. For the $Ar/H_2/Air$ mixtures, we are using the Ar I excited states since they could easily be identified in the spectra. Transition prpbabilities and statistical weights of the observed Ar I lines are given in Table 4 [3].

TABLE 4: Transition probabilities and statistical weights of Ar I lines [3].

λ [nm]	g_k	$A_{ki}[10^6\ s^{-1}]$	$E_k[cm^{-1}]$
427.21	3	0.797	117 151.32
667.72	1	0.236	108 722.61
727.29	3	1.830	107 496.41
738.39	5	8.470	107 289.70
751.46	1	40.00	107 054.27

In Fig. 33 we present the electron excitation temperature as a function of the power density. One can see that the temperature varies weakly with the amount of H_2 in the system. The figure also indicates that the average energy for electron excitation is decreasing at the high power densities. This is consistent with the results presented Fig. 13 which indicated that the temperature would be decreasing since the populations of the electronicly excited states decreased faster with the higher power.

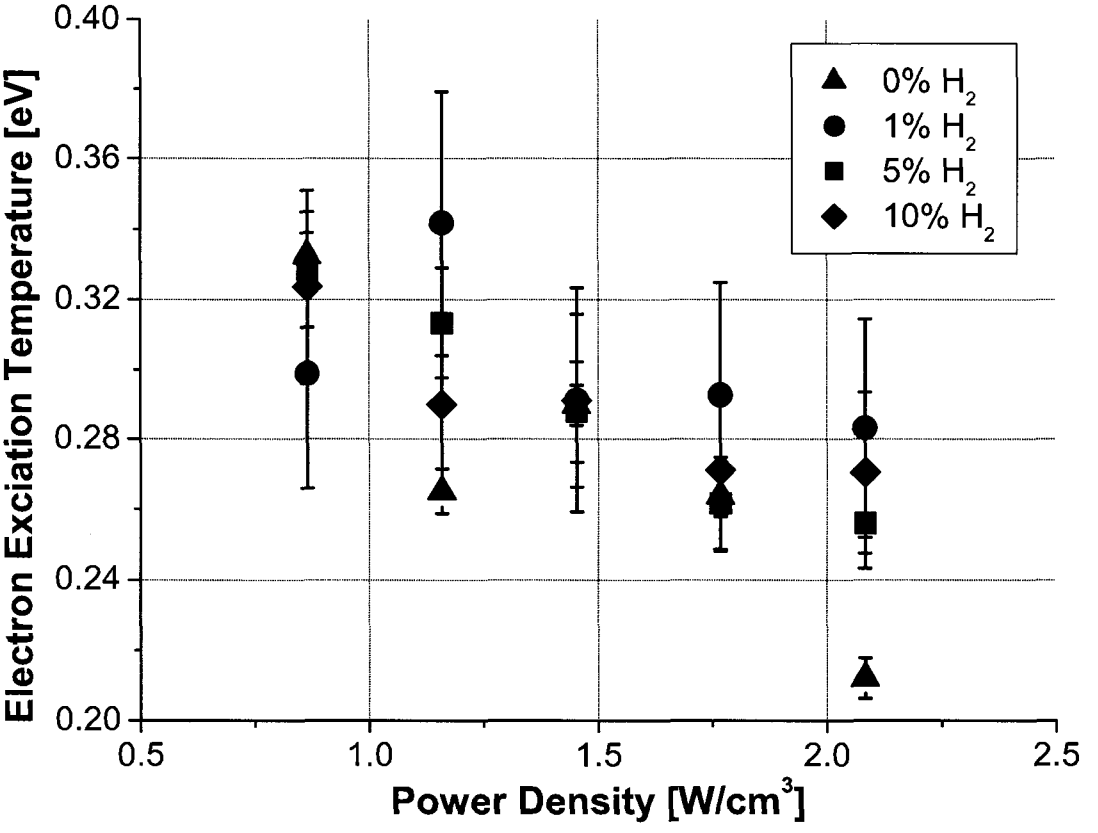

FIG. 33: Electron excitation temperature as a function of the power density at different percentages of H_2 in the gas mixture at a pressure of 2.4 Torr [18]. Statistical error bars are indicated.

II.3.5 Electron Density

In hydrogen rich discharges, the hydrogen Balmer lines are the most commonly used for determination of the electron density since they are usually very strong. When gas contains nitrogen, the N_2 second positive system can be used to determine the electron density. Thus, for the $Ar/H_2/Air$ mixtures, we used both methods of calculation in order to compare the results. For the Martian simulated mixture, we used only the nitrogen method.

Hydrogen Balmer Series

The electron density can be obtained by measuring the Stark broadening of the hydrogen Balmer lines listed in Table 5.

TABLE 5: The hydrogen Balmer lines.

Line Name	λ [nm]
H_α	656.21
H_β	486.08
H_γ	434.00
H_δ	410.12
H_ϵ	396.97

Although the H_β line is the most frequently used spectral line, in our research we chose to use the H_δ line since the H_β, as well as the H_α, line were saturated. In addition, we observed that, unlike the H_γ and H_ϵ lines, the H_δ line did not have any interference with the Ar lines as seen in Fig. 34. It also has a measurable linewidth for better evaluation of the electron density that is shown in Fig. 35.

Stark broadening in a supersonic flowing discharge is always accompanied by Doppler broadening due to thermal motion of thobservation was perpendicular to the direction of the gas flow. Correspondingly, the second Doppler effect was eliminated [18]. Following the procedure outline by Ivković *et al.* [46], the Doppler broadening term (W_D) can be expressed in terms of the wavelength (λ), the mass of the hydrogen atom (M_H), and the gas temperature (T_g) since the hydrogen atoms are assumed to be in thermodynamic equilibrium at a specific gas temperature,

$$W_D = 3.58 \times 10^{-7} \lambda \left(\frac{T_g}{M_H}\right)^{0.5}. \tag{40}$$

Instrumental broadening adds to the line widths shown in Figs. (34) and (35). This broadening is due to the sensitivity of the diffraction grating and the size of a single pixel in the CCD camera. We therefore corrected instrumental broadening by including the corresponding half width, W_I. The Stark broadening of a single Balmer line can then be determined by

$$W_S = \left(W_M^{1.4} - W_{DI}^{1.4}\right)^{\frac{1}{1.4}} \tag{41}$$

where W_M is the measured half width half maximum for the line and

$$W_{DI} = \left(W_D^2 + W_I^2\right)^{0.5}. \tag{42}$$

The electron density can then be determined by

$$N_e = 8.0 \times 10^{18} \left(\frac{W_S}{\alpha_{1/2}}\right)^{1.5} \tag{43}$$

where $\alpha_{1/2}$ is a parameter specific to each hydrogen Balmer line and in the present case $\alpha_{1/2} = 0.150$ for the H_δ line.

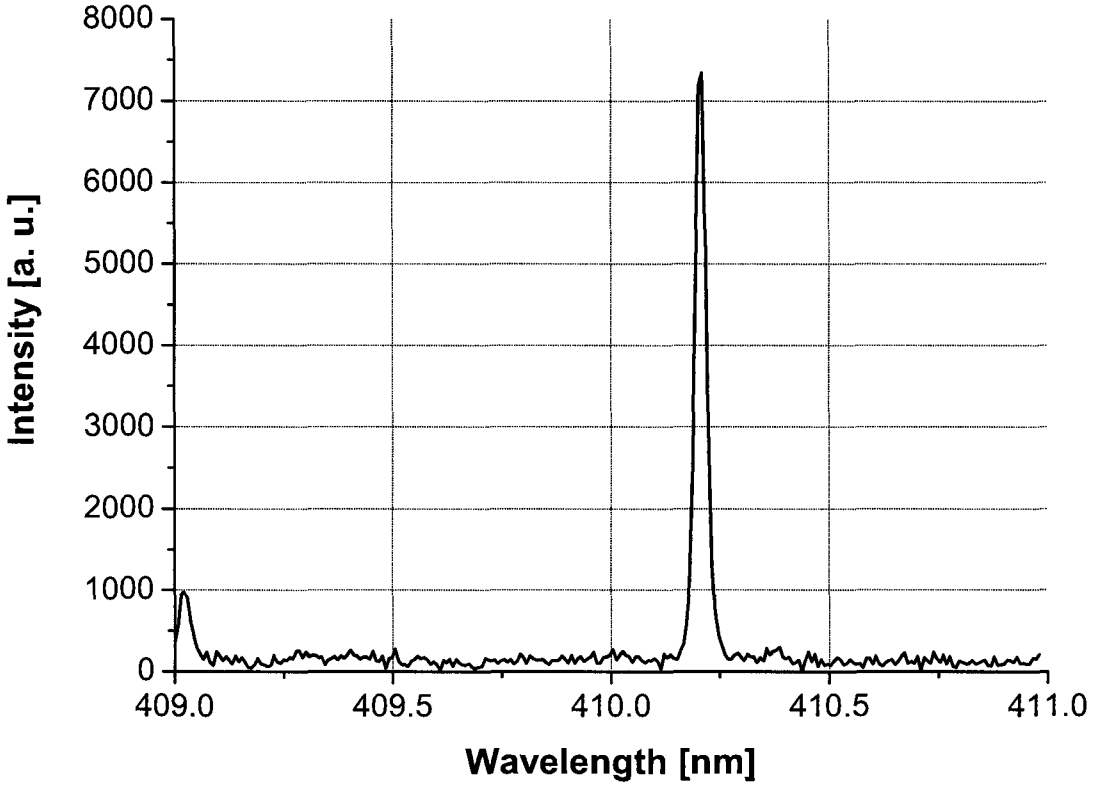

FIG. 34: H_δ line in a mixture of 95% Ar and 5% H_2 at a pressure of 2.5 Torr and 1.45 W/cm^3.

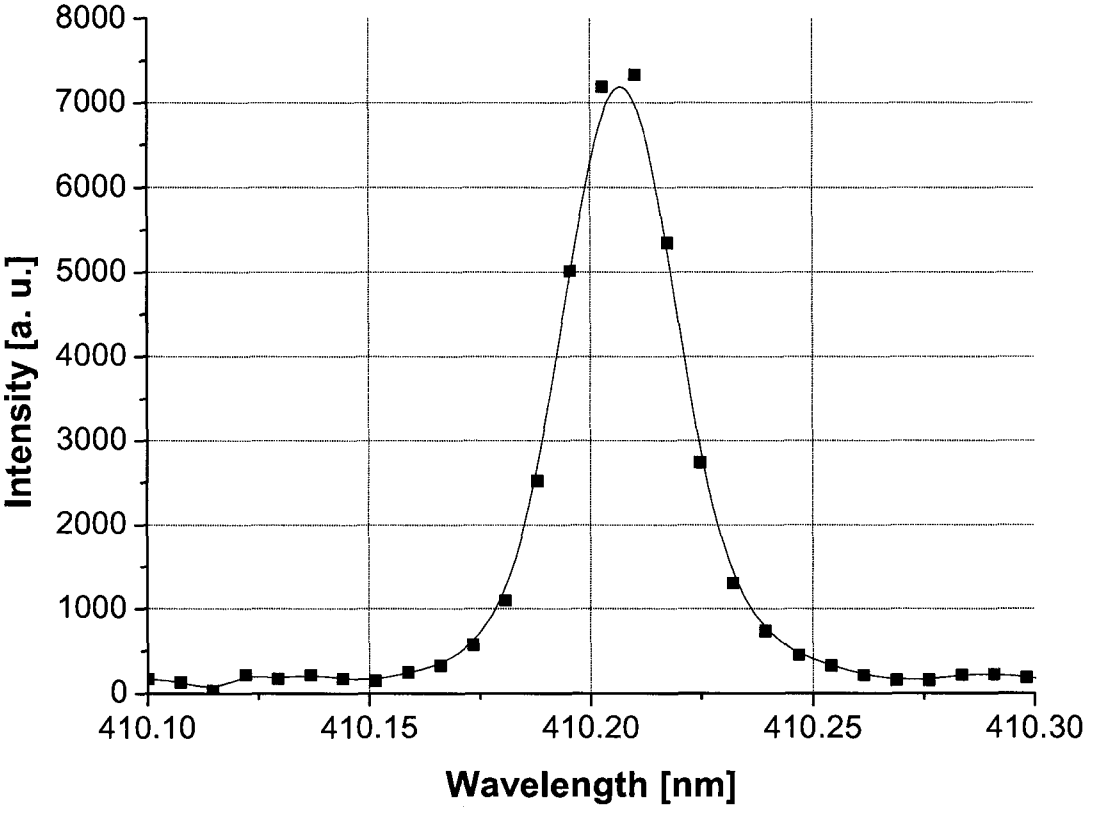

FIG. 35: H_δ line with pixels in a mixture of 95% Ar and 5% H_2 at a pressure of 2.5 Torr and a power density of 1.45 W/cm^3.

In Fig. 36 we present the electron density as a function of the pwer density. It can be seen that the electron density is constant as the power is increased. On the other hand, the electron density decreases with increasing amounts of H_2 in the system. This is an indication of ionization loss in our Ar/H_2 discharges and is consistent with the experiments performed by Meulenbroeks *et al.* [47] and with the Monte Carlo model for Ar and Ar/H_2 discharges by Bogaerts and Gijbels [8]. In addition, we observed how the electron density varied in the afterglow region outside of the cavity and presented in Fig. 37. it can be seen that the the electron density was fairly constant up to 15 mm outside of the cavity for a discharge of 95% Ar and 5% H_2 at a power density of 1.75 W/cm^3. After this point the electron density began to decrease sharply.

The model was then added into the discharge and the same measurements were repeated. We observed the change in the electron density in front of the model for a discharge of 95% Ar and 5% H_2 (see Fig. 38). From the figure it is obvious that the electron density does not vary greatly across the shock front given a statistical error of $\pm 3.8\%$. In addition, it is evident from comparison of this figure with the model free density measurments that the electron density decreased when the model was placed in the discharge. After careful evaluation, we found that this was beacuse the teflon spheres where attached to an aluminum rod inside of the cavity. The addition of the sphere and rod to the discharge caused the cavity to detune which resulted in the observed decrease in electron density.

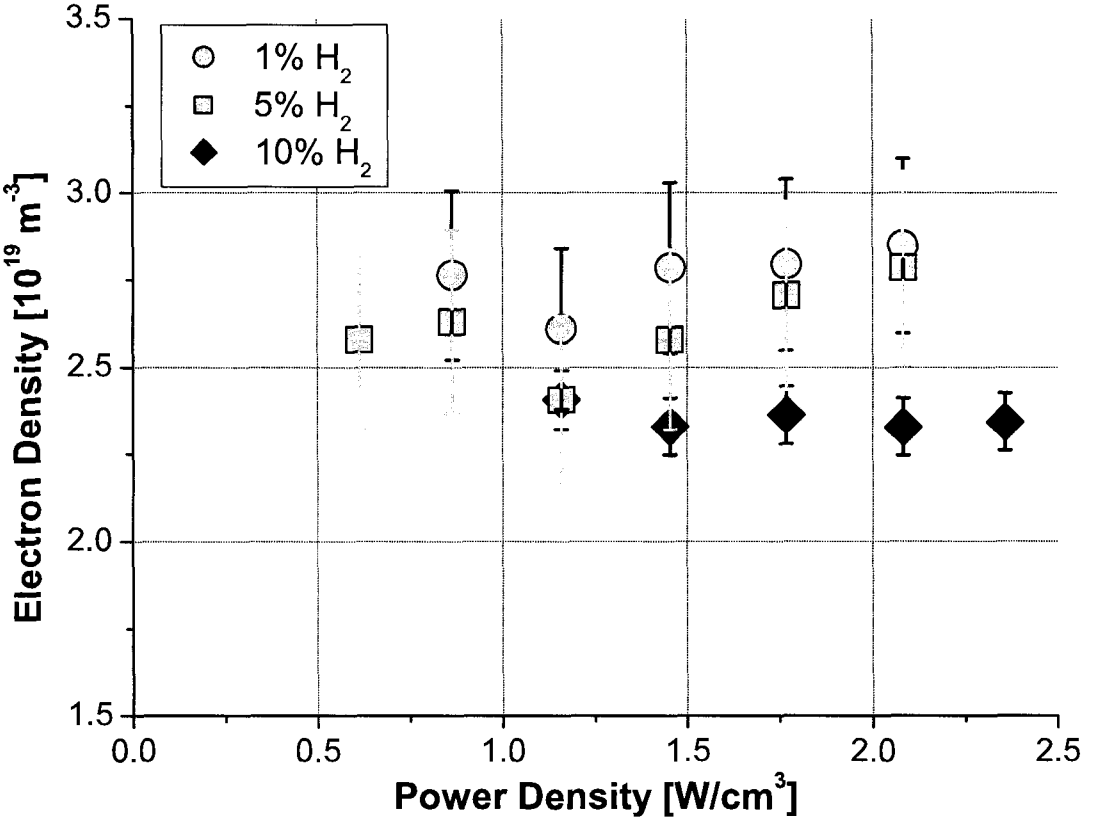

FIG. 36: Electron density as function of the power density in the cavity at a pressure of 2.3 Torr and with different amounts of H_2 in the gas mixture. Statistical error bars are indicated.

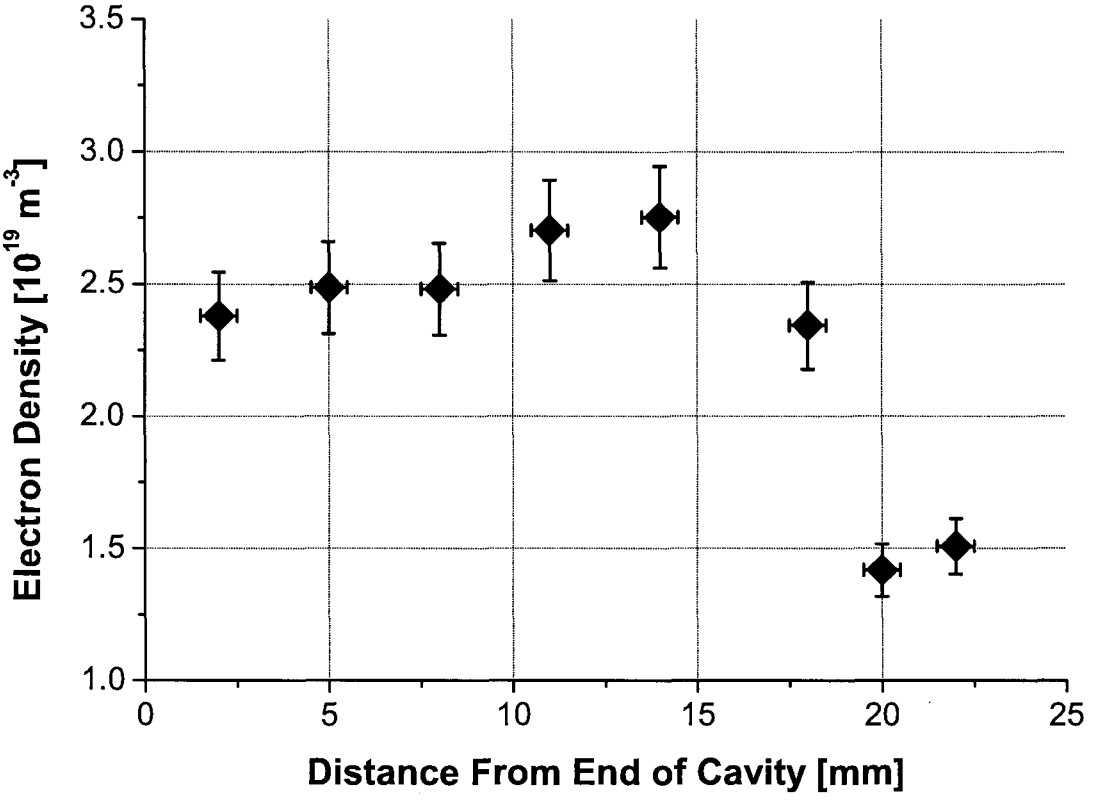

FIG. 37: Electron density as a function of the distance from the end of cavity at a pressure of 2.3 Torr and a power density of 1.75 W/cm^3 in a discharge of 95% Ar and 5% H_2. Statistical error bars are indicated.

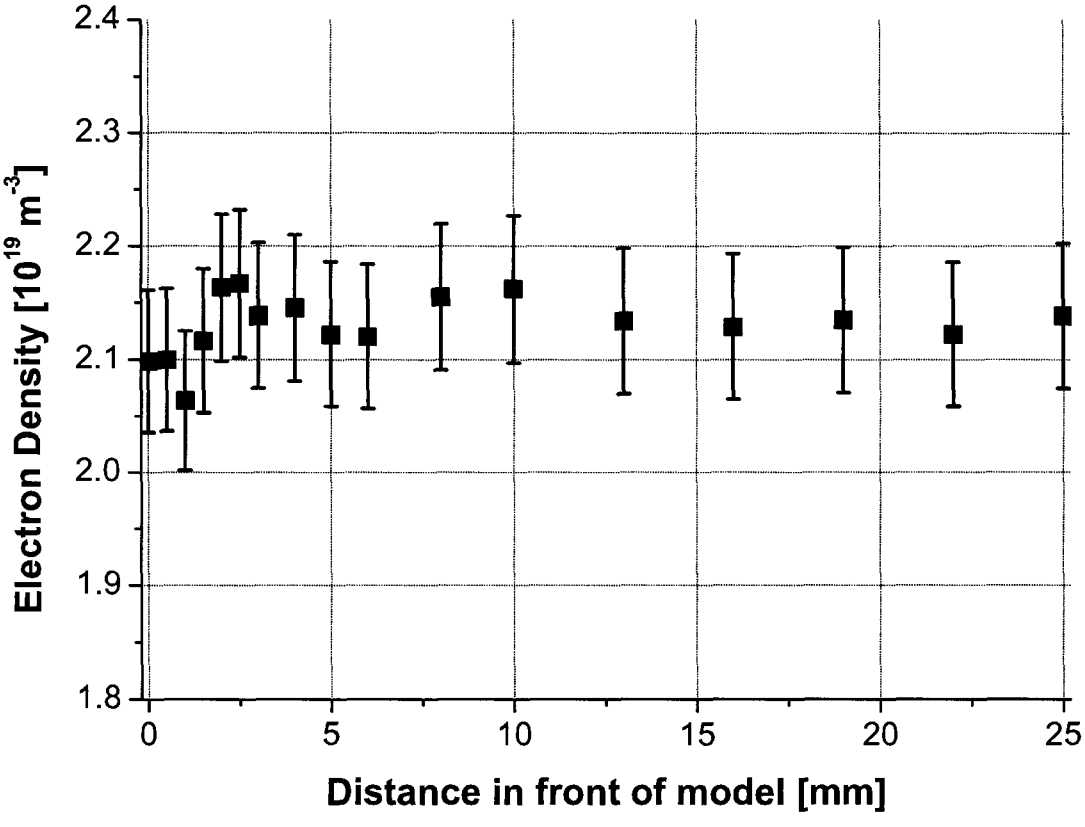

FIG. 38: Electron density as a function of the distance in front of the model for a power density of 1.75 W/cm^3 in a discharge of 95% Ar and 5% H_2 at a pressure of 2.4 Torr.

Nitrogen Spectra

Another method for determining the electron density is by observing the intensity of the N_2 second positive system. The population of the $N_2(C^3\Pi_u)$ state is predominantly determined through three process [48]:

1. electron impact excitation

$$e + N_2(X^1\Sigma_g^+) \rightarrow e + N_2(C^3\Pi_u), \tag{44}$$

2. radiative transition

$$N_2(C^3\Pi_u) \rightarrow N_2(B^3\Pi_g) + h\nu, \tag{45}$$

3. quenching

$$N_2(C^3\Pi_u) + N_2(X^1\Sigma_g^+) \rightarrow 2N_2(X^1\Sigma_g^+). \tag{46}$$

Employing these three equations, we can determine the population rate of the $N_2(C^3\Pi_u)$ state,

$$\frac{d[N_2(C)]}{dt} = k_e^C N_e N - \frac{[N_2(C)]}{\tau} - k_3[N_2(C)]N. \tag{47}$$

Here $[N_2(C)]$ is the concentration of the excited nitrogen molecules in state $N_2(C^3\Pi_u)$, k_e^C is the electron excitation coefficient, N_e is the electron density, N is the concentration of molecules in the ground state, τ is the lifetime of the $N_2(C^3\Pi_u)$ state, and k_3 is the rate constant for collisional deexcitation. If we assume that the population of the $N_2(C^3\Pi_u)$ state does not change with time, then

$$\frac{d[N_2(C)]}{dt} = 0 \tag{48}$$

and

$$[N_2(C)] = \frac{\tau k_e^C N}{1 + \tau k_3 N} N_e. \tag{49}$$

Here $[N_2(C)]$ can be determined from calculation of the population as described in section II.3.1, $\tau = 46$ ns, $k_3 = 4.6 \times 10^{-11}\text{cm}^3/\text{s}$, and N is assumed to be equal to the neutral particle density since the apparatus was kept constantly under vacuum.

The excitation rate coefficient is a function of the reduced electric field (E/N) for the system which is about 10 Td in our experiment [28]. From Ref. [49], we determined that $k_e^C = 4.6 \times 10^{-15}\text{cm}^3/\text{s}$.

Comparing the results in Fig. 39, we found that there was a large difference in the electron density as determined from the two different methods. In addition, we observe that the electron density is increasing with power density when calculated from the N_2 spectrum. This increase was expected, since the possibility of ionization of different atoms and molecules should increase when the energy of the system increases. Yet the data taken from the hydrogen lines appears to be constant. This result was consistent for discharges with 1% and 10% H_2 in the gas mixture.

The analysis of the N_2 spectrum in the Martian simulated mixture shows interesting results. In Fig. 40 we see that the electron density again increases with power density. A comparison with the data for the Ar/H_2 discharge in Fig. 39 showed that the electron density was nearly two orders of magnitude lower in the Martian simulated mixture. This difference can be accounted for by the presence of negative ions in the discharge. In particular, the presence of O_2 from the dissociation of CO_2 leads to the production of O^-, O_2^-, and O_3^- in the discharge. These negative oxygen ions are expected to contribute to the overall charge balance of the discharge [50]. Thus the electron density in the discharge could decrease due to recombination through the following processes:

$$
\begin{aligned}
O + O^- &\rightarrow O_2 + e \\
O^- + O_2^+ &\rightarrow O(^3P) + O_2 \\
O_2^- + O^+ &\rightarrow O_2 + O(^3P) \\
O_2^- + O_2 &\rightarrow 2O_2 + e \\
O_2 + O^- &\rightarrow O_3 + e \\
O_3^- + O(^3P) &\rightarrow 2O_2 + e \\
O_3^- + O_2^+ &\rightarrow O_2 + O_3 \\
O_2^- + 2O(^3P) &\rightarrow O_3 + O(^3P).
\end{aligned}
$$

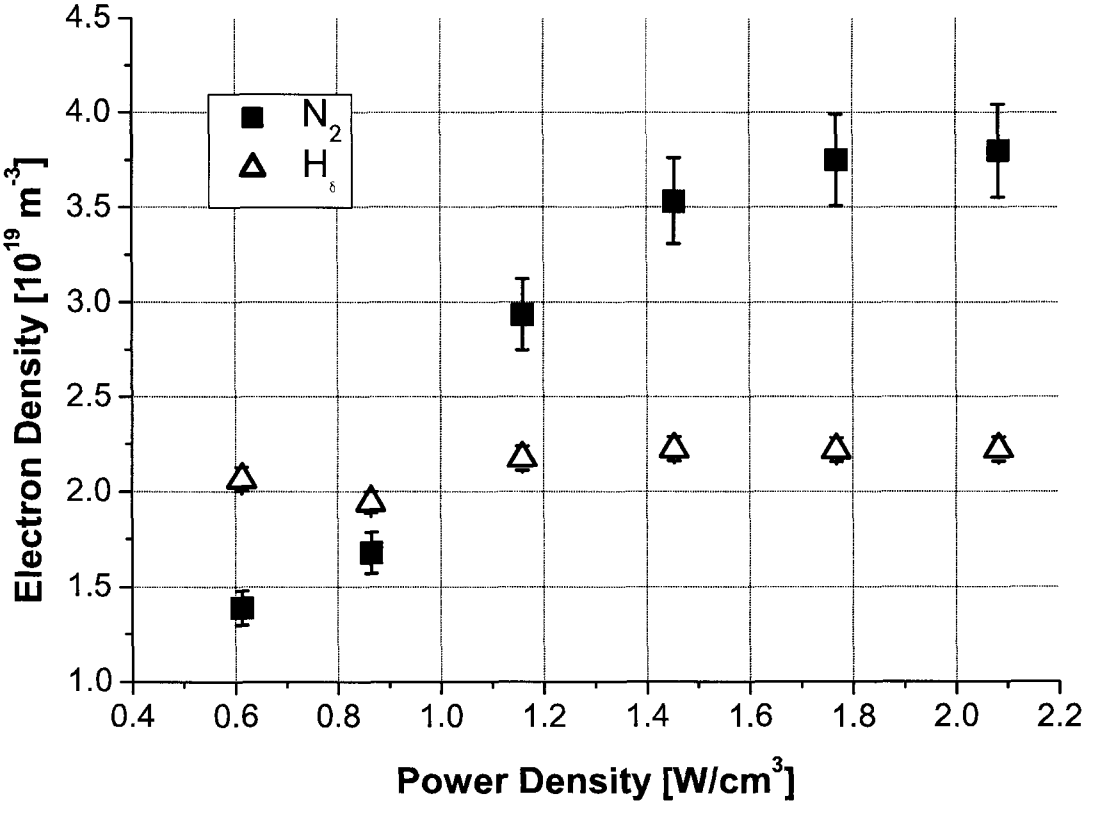

FIG. 39: Electron density as function of the power density calculated from the hydrogen Balmer lines and the N_2 second positive system in a discharge of 89.85% Ar, 4.7% H_2, and 5.45% air.

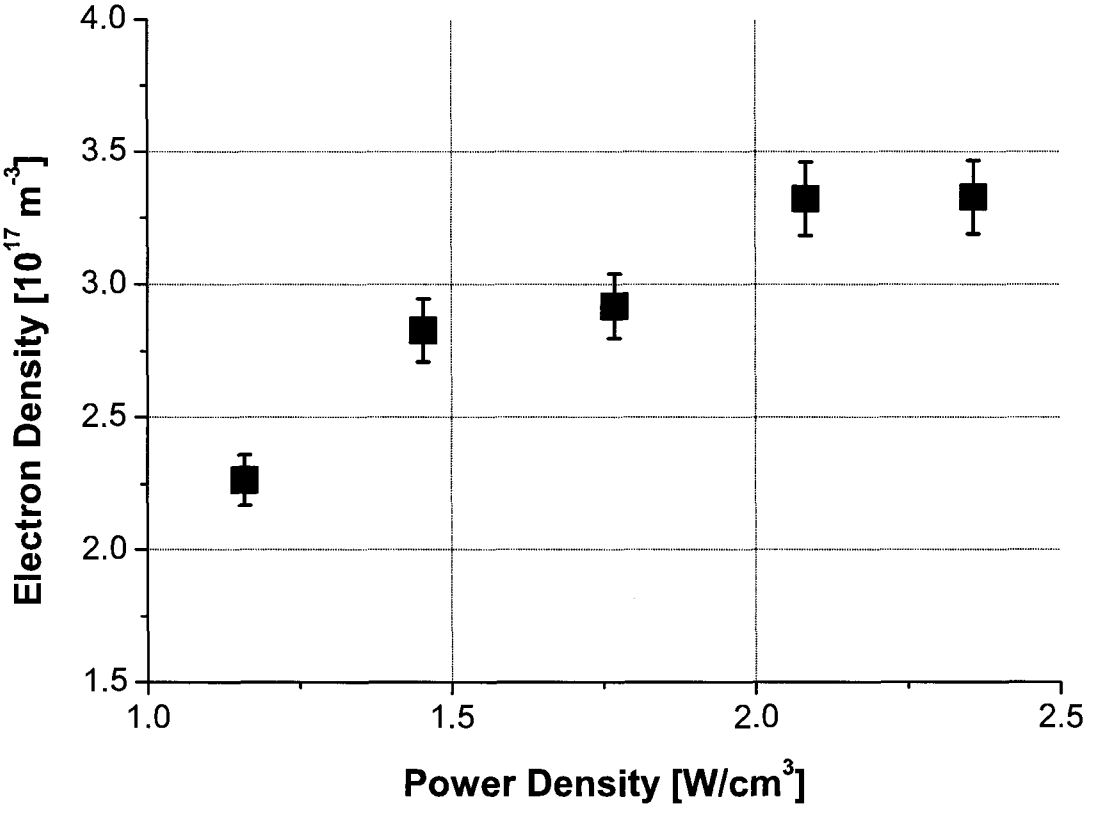

FIG. 40: Electron density as function of the power density calculated from the N_2 second positive system in a Martian simulated discharge at a pressure of 3.3 Torr.

II.3.6 Electron Temperature

The electron temperature was obtained from the intensity ratio of an Ar atomic and an Ar ionic spectral line. For the $Ar/H_2/Air$ discharge we used the Ar I $5p\left[\frac{1}{2}\right] \rightarrow 4s'\left[\frac{1}{2}\right]^o$ transition at 470.232 nm and the Ar II $4p^2P^0 \rightarrow 4s^2P$ state at 476.487 nm shown in Fig. 41. Then by assuming chemical equilibrium between the Ar neutrals and Ar ions, we can apply the Saha-Boltzmann equation to determine the electron temperature (T_e) [51],

$$\frac{N}{N^+} = \frac{N_e}{2}\frac{g}{g^+}\left(\frac{h^2}{2\pi m_e k_B T_e}\right)^{3/2} \exp\left(\frac{E_{ion} + E_{exc}^+}{k_B T_e}\right). \tag{50}$$

Here N is the population of each state as described in section II.3.1, g is the statistical weight, h is Planck's constant, m_e is the mass of the electron, k_B is the Boltzmann constant, E_{ion} is the ionization energy of the electron in the $5p\left[\frac{1}{2}\right]$ state for the Ar I transition that is 1.2956 eV, and E_{exc}^+ is the excitation energy of the $4p^2P^o$ state of the Ar II transition that is 19.867 eV.

In Fig. 42 we present the electron temperature as a function of the power density in a discharge of pure Ar and a mixture of 95% Ar and 5% H_2. In the figure we observe that the variations in the electron temperature were not significant since the statistical error was about 10%. The main source of error in this dat comes from a low signal to noise ratio in this region. The implications of this figure are that as the power increases the average energy of the electrons in the discharge do not change. In addition, we noticed that the electron temperature decreased when 5% H_2 was added to the discharge. This decrease is a direct indication of ionization loss due to the presence of H_2 in the discharge.

In the second part of the experiment, the model was added to the discharge and we scanned a 10 mm distance in front of the model where the shock front should be located (see Fig. 43). As can be seen from the figure, the electron temperature did not vary greatly for a discharge of Ar at a power density of 1.45 W/cm^3 and a pressure of 3.6 Torr. Comparing this figure with the previous one we see that when the model was added to the discharge the electron temperature decreased by nearly 150 K.

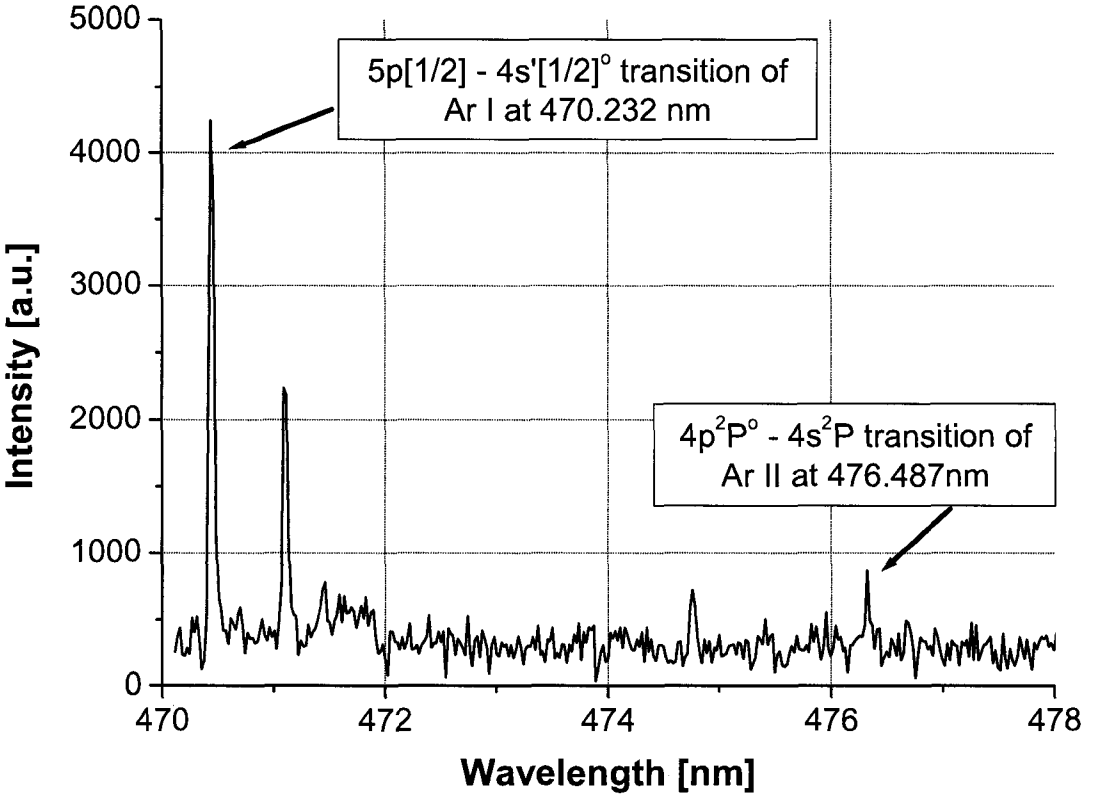

FIG. 41: Spectra of the Ar I and Ar II lines used for determination of the electron temperature in a gas discharge of 95% Ar and 5% H_2 at a pressure of 2.5 Torr and a power density of 1.45 W/cm^3.

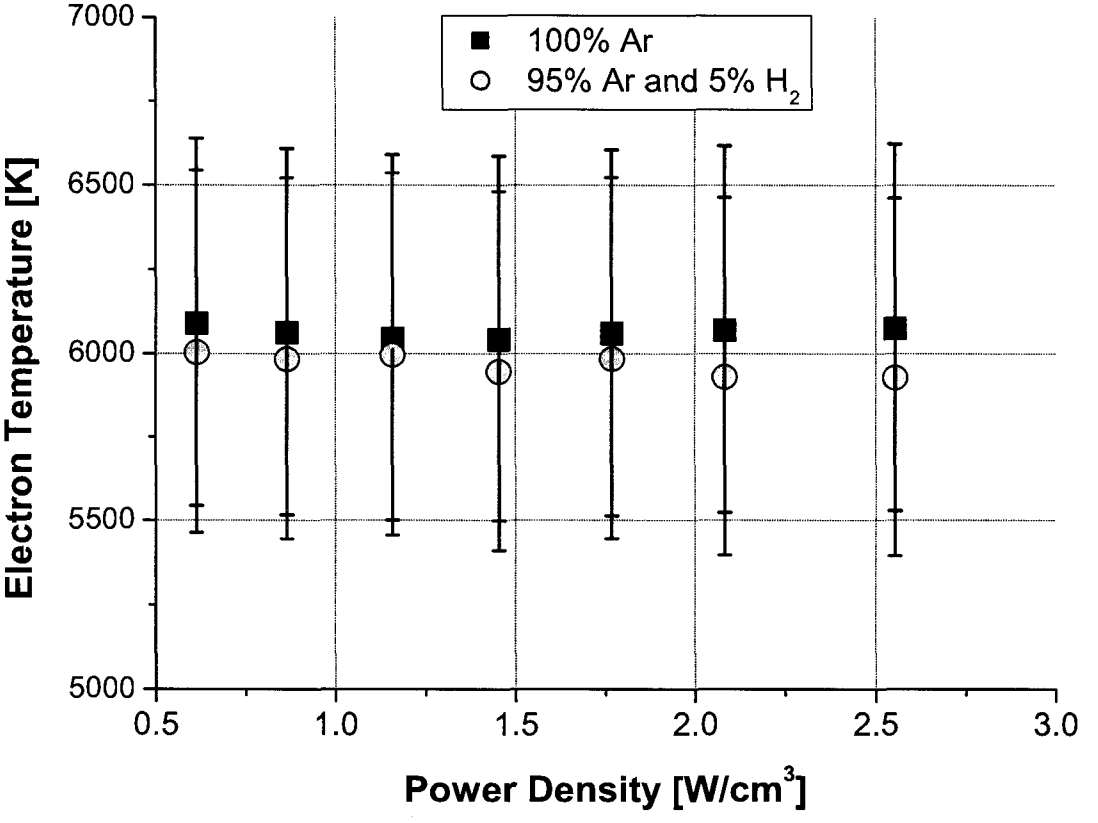

FIG. 42: Electron temperature as function of the power density for discharges of pure Ar and a mixture of 95% Ar and 5% H_2 at a pressure of 2.5 Torr. Statistical error bars are indicated.

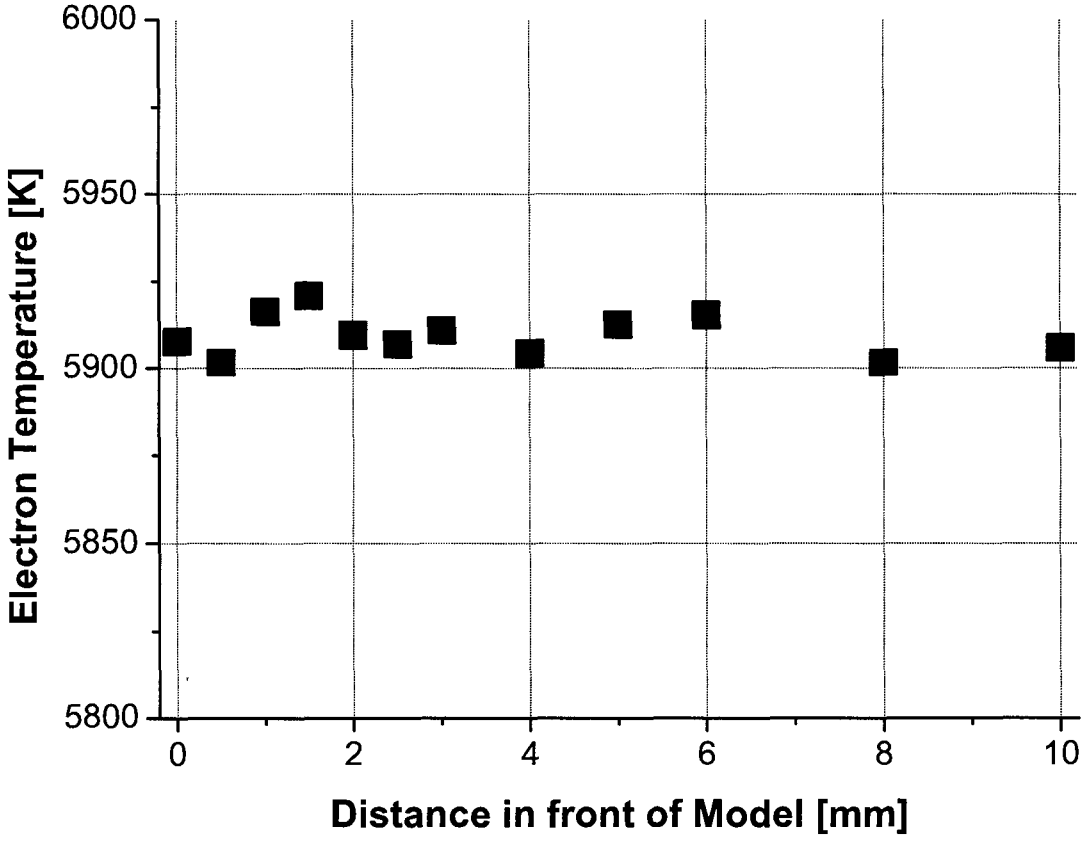

FIG. 43: Electron temperature as function of the distance in front of the model for a discharge of pure Ar at a power density of 1.45 W/cm^3 and a pressure of 3.6 Torr. Statistical error was $\pm$ 10%

CHAPTER III

GAS KINETIC MODELING OF AN AR/H_2/AIR DISCHARGE

A supersonic microwave discharge of Ar/H_2/Air is a complex mixture of three initial component: a noble gas (Ar), hydrogen, and air which contains several molecular species. As explained in Chapter I, Ar is added in the mixture to help control the combustion which occurs in these mixtures. The presence of hydrogen, nitrogen, and oxygen molecules in the discharge leads to complex branching inter-radical chemistry, which may result in the decrease of the degree of ionization [18]. All these processes are poorly understood. However, effects on plasma parameters for an Ar/H_2 discharge have been studied by many researchers.

In an early experiment, Capitelli and Dilonardo [23] observed that the dissociation rate for H_2 decreased when the amount of H_2 added to an Ar discharge was increased. Bogaerts and Gijbels [8] constructed a combination of Monte Carlo and fluid dynamics model for a glow discharge of Ar with 1% H_2. By observation of the spectral line intensities, they found that the densities of the Ar^+ ions, electrons, and Ar metastable atoms decreased considerably with the addition of H_2. Part of the decrease in the Ar^+ ion density was due to an increase in ArH^+ ion production, which affected the use of admixture hydrogen for spectral diagnostic purposes. The strong effect of the addition of molecular hydrogen was also observed in the enhancement of physical sputtering, which was again explained by the increase of heavy ion (ArH^+) population with respect to light charged particles (H^+) [54]. Further evidence of ionization loss in Ar/H_2 plasmas was found by mass spectrometry in a fast flow (subsonic) glow discharge [24]. However, the mechanism of the effect was attributed to the quenching by molecular hydrogen of excited Ar states with energies higher than 4p, which were considered as precursors in Ar^+ and ArH^+ formation.

In this chapter, we will discuss the use of gas kinetic modeling for determination of the electron transport coefficients. In this type of modeling the Boltzmann transport equation is solved to determine the electron energy distribution functions. From these functions the average electron energy and rate coefficients for different processes within the discharge can be determined. This is important since in a microwave discharge the electrons gain energy from the microwaves and then transfer that energy to the surrounding atoms and molecules through excitation, ionization, and dissociation. In the following we discuss the effects associated with the addition

of H_2 and air to the discharge on these parameters.

III.1 BOLTZMANN EQUATION AND TRANSPORT COEFFICIENTS OF ELECTRONS

In the absence of a magnetic field, the flow of electrons through a unit velocity phase space is described by the Boltzmann transport equation [55]

$$\frac{\partial f(\vec{r},\vec{v},t)}{\partial t} + \vec{v}\cdot\vec{\nabla} f(\vec{r},\vec{v},t) - \frac{e\vec{E}}{m}\cdot\vec{\nabla} f(\vec{r},\vec{v},t) = \left(\frac{\partial f(\vec{r},\vec{v},t)}{\partial t}\right)_{coll}. \qquad (51)$$

Here the distribution of electrons in their velocity space $\vec{v}$ at the space coordinate $\vec{r}$ and at time t is given by the electron velocity distribution function $f(\vec{r},\vec{v},t)$. In the case of a weakly ionized plasma, the right hand side of Eq. (51) will take into account the elastic and inelastic collisions between electrons and neutral atoms or molecules.

Due to the complexity of Eq. (51), only approximate solutions are applied for selected cases. We begin by assuming that the electrons are drifting through a gas with temperature T and electric field E. The homogenous solution is assumed for the electrons in the bulk region of the discharge. Additionally, a steady state solution is valid when the electron collision frequency in the discharge is approximately two or three orders of magnitude larger than the driving frequency. In the case of our study, the solution can be further simplified by assuming symmetry about the discharge axis. By applying these conditions, a steady state isotropic solution can be obtained [56]

$$\frac{1}{3}\left(\frac{eE^2}{N}\right)\left(\frac{\epsilon}{Q_m}\frac{df}{d\epsilon}\right) + \frac{2m}{M}\frac{d}{d\epsilon}(\epsilon^2 Q_m f) + \frac{2mk_BT}{M}\frac{d}{d\epsilon}\left(\epsilon^2 Q_m \frac{df}{d\epsilon}\right) + \sum_j (\epsilon+\epsilon_j) f(\epsilon+\epsilon_j) Q_j(\epsilon+\epsilon_j) - \epsilon f(\epsilon)\sum_j Q_j(\epsilon) = 0. \qquad (52)$$

We have expressed, by convention, the solution in terms of the electron energy $\epsilon = mv^2/2$ and have neglected super-elastic collisions. In Eq. (52), Q_m is the total elastic collision cross section in the forward direction; Q_j is the cross section of the j^{th} inelastic collision; m, e are the mass and charge of the election; M, N, and T are the mass, density, and temperature of the neutral gas molecules; k_B is the Boltzmann

constant; and f is the isotropic electron distribution function in the energy space (EEDF).

For a gas mixture, an appropriate modification to the cross sections of all gas species in Eq. (52) should be taken into account: $Q_m = \sum_n Q_m^n G^n$ in the first term and $Q_m = \sum_n M Q_m^n G^n / M^n$ and $M = \sum_n M^n G^n$ in the second and third terms. Here Q_m^n is the momentum transfer cross section, G^n is the mole fraction, and M^n is the mass of the molecule of the n^{th} gas consituent [57]. In this research we used a numerical Boltzmann solver (Bolsig) to determine the EEDF. This program is based on the technique outlined in Ref. [58], which retains only the first two terms of the Legendre polynomial expansion. However, this program allows for calculation of a discharge with up to three species at a time.

Solutions of Eq. (52) can be used to calculate electron transport parameters of the discharge, which includes rate coefficients for the primary chemical kinetic processes, k, and the average electron energy, T_e.

$$k = \left(\frac{2e}{m}\right)^{1/2} \int_0^\infty \epsilon Q_j(\epsilon) f(\epsilon) d\epsilon \tag{53}$$

$$T_e = \frac{2}{3} \int_0^\infty \epsilon^{3/2} f(\epsilon) d\epsilon. \tag{54}$$

Evaluation of the EEDF, rate coefficients, and electron temperature depend on knowledge of the electron-molecule collision cross sections. However, the collision cross sections for most gas mixtures have not been determined by either experiment or calculation and a very limited set of data is available for use.

In a mixture of $Ar/H_2/Air$, the dominant neutral species are Ar, H_2, N_2, and O_2. Therefore, only the collision cross sections for these species will be used for determining the EEDF and associated transport parameters. The cross sections for these species have been compiled from many sources [59, 60, 61, 62]. In Fig. 44 we show the momentum transfer cross section for each species.

To determine the accuracy of the Bolsig program for determination of the EEDF, we compare the Bolsig results at a temperature of 300 K with values calculated by Ferreria and Loureiro [63]. Results presented in Fig. 45, show that the Bolsig results are in good agreement with the calculated ones at both values of the reduced electric field (E/N).

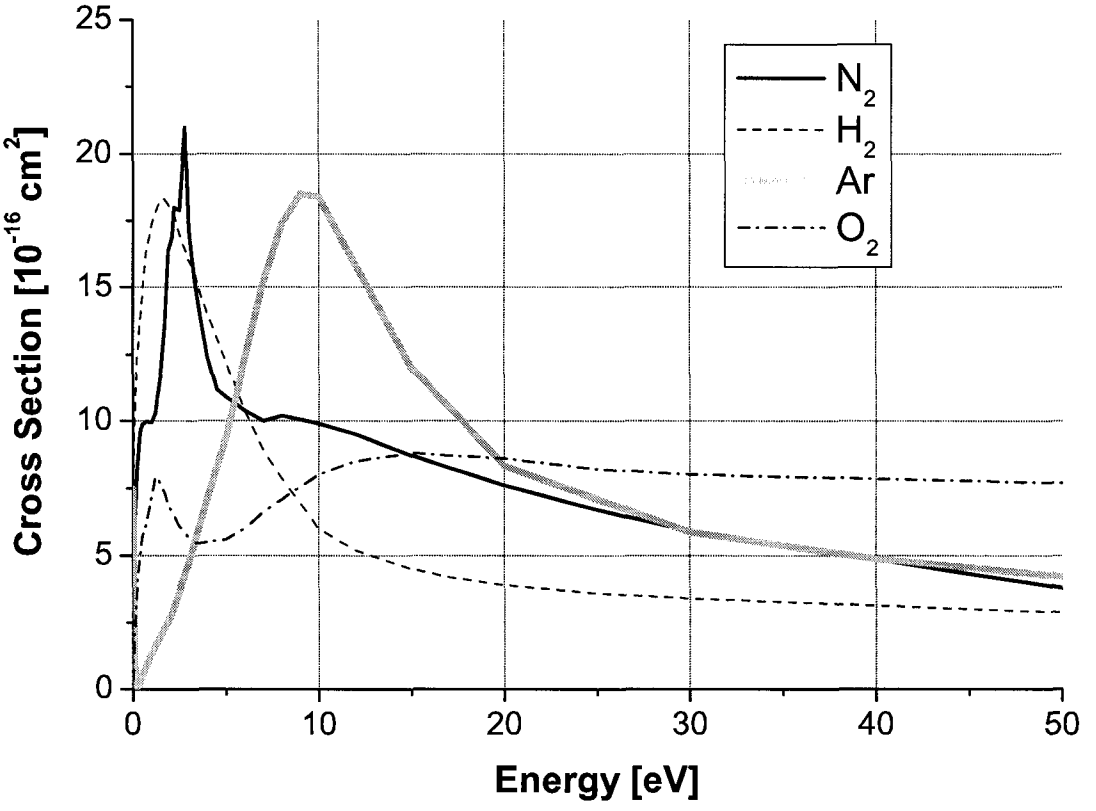

FIG. 44: Momentum transfer cross section for Ar [59], H_2 [60], N_2 [61], and O_2 [62] as a function of energy.

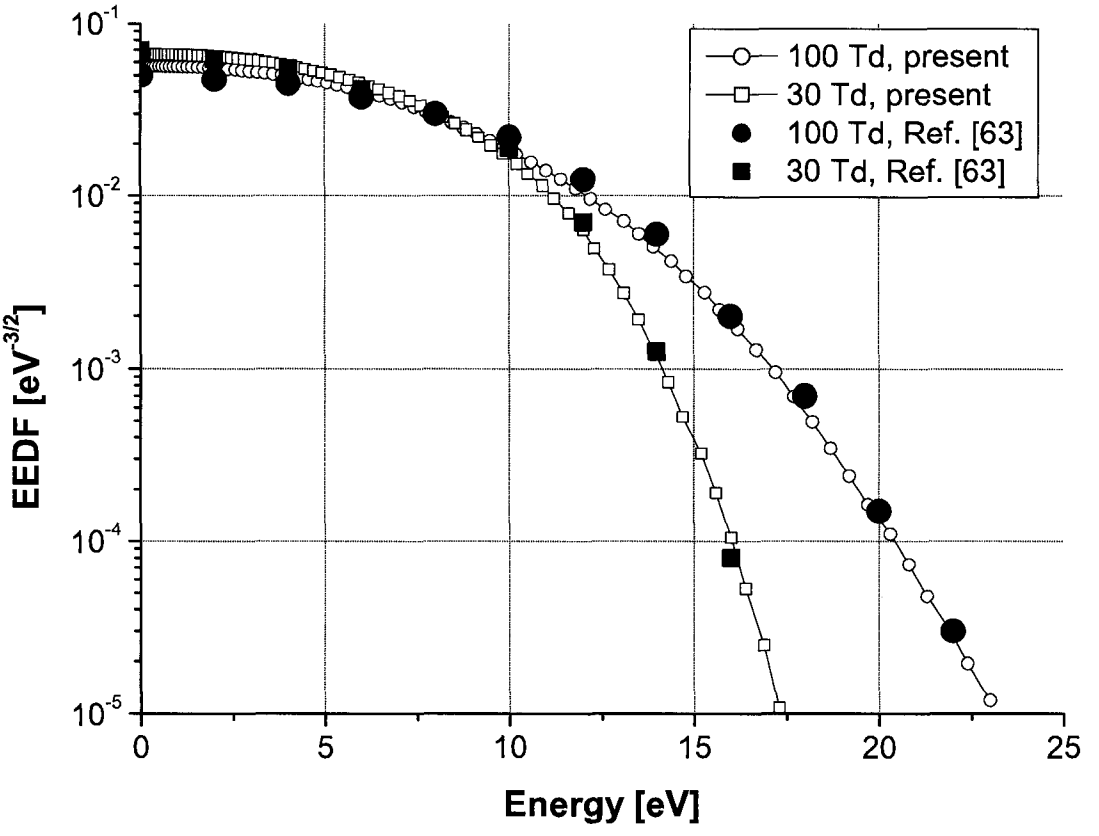

FIG. 45: Electron energy distribution functions for Ar from Ref. [63] and calculated by Bolsig (present data).

III.2 INFLUENCE OF H_2 ON AR DISCHARGES

As discussed previously, small amounts of H_2 added to an Ar discharge can have a major impact on the degree of ionization loss, ion intensities, and the dissociation rate of different species. Therefore, it is important to study the effects that H_2 will have on both the EEDF and the electron transport parameters.

In Fig. 46 we present the EEDF as a function of the energy at a reduced electric field of 25 Td and a temperature of 300 K. We see from the figure that at large values of the energy the EEDF drops by up to 2 orders of magnitude as the amount of H_2 in the system increases. This decrease of fast electrons is caused by an increase in vibrational and electronic excitations of H_2.

Using the results from Fig. 46, the electron temperature was determined employing Eq. (54). We show in Fig. 47 the electron temperature as a function of the reduced electric field for an Ar discharge with different amounts of H_2 added to it. In most supersonic flowing microwave discharges, the reduced electric field will be below 50 Td or 5.0×10^{-16} V cm^2. Considering this region of the reduced electric field in the figure, we see that the amount of H_2 in the system has a significant effect on the average electron temperature. In fact at very low values of the reduced electric field, the electron temperature can vary by approximately 2 eV or 23,000 K. This reduced temperature means that the dissociation rate of H_2 has to decrease since a smaller T_e indicates that there is a small amounts of energetic electrons in the discharge. In addition, the decrease in T_e with increasing amounts of H_2 is a direct indication of ionization loss in the discharge.

The rate coefficients for different processes in the discharge were determined from Eq. (53). We present in Fig. 48 the results of electron excitation of the Ar 4s'$[1/2]_1$ state. From the figure we observe that the rate coefficients below 50 Td depend strongly on the amount of H_2 in the discharge. These excitation rates are directly related to the number of energetic electrons in the discharge. From the previous figure, we observed that at low E/N there will be fewer energetic electrons. Thus it is very important in supersonic microwave discharges to know the exact composition in order to accurately model the discharge.

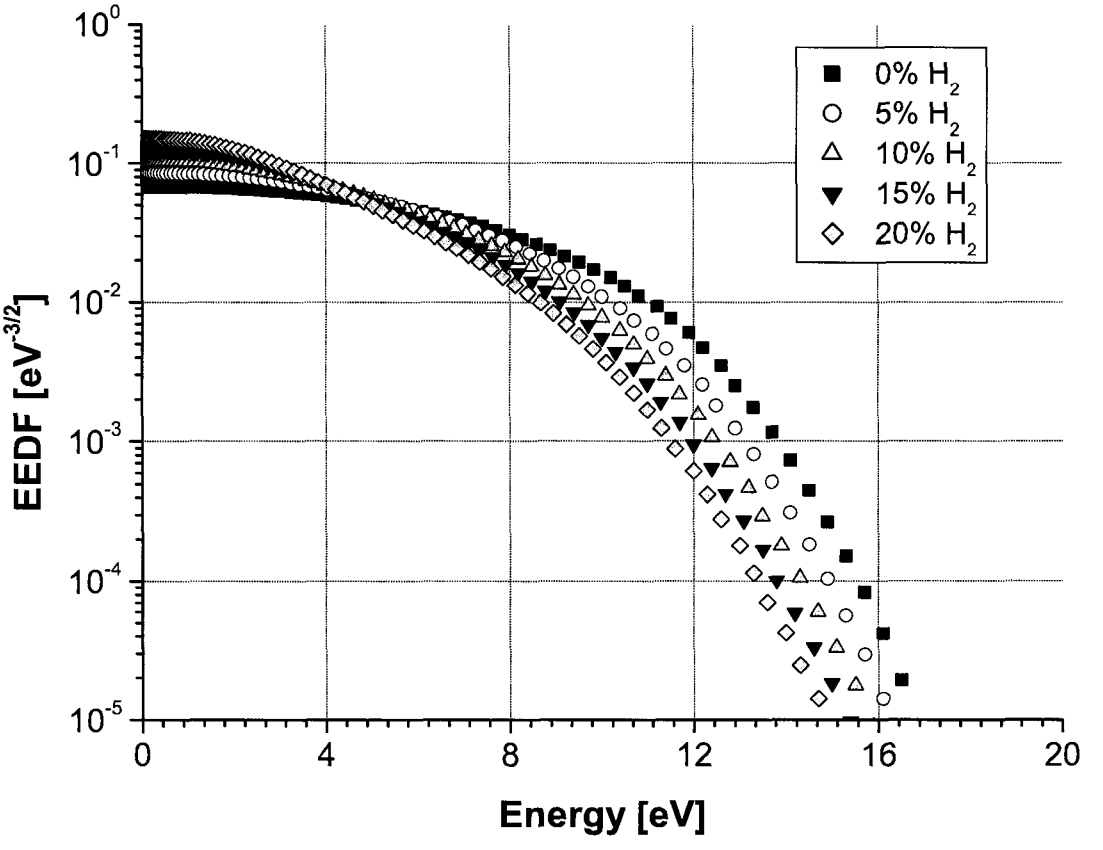

FIG. 46: Electron energy distribution functions for Ar discharge with different amounts of H_2 at a reduced electric field of 25 Td as a function of energy.

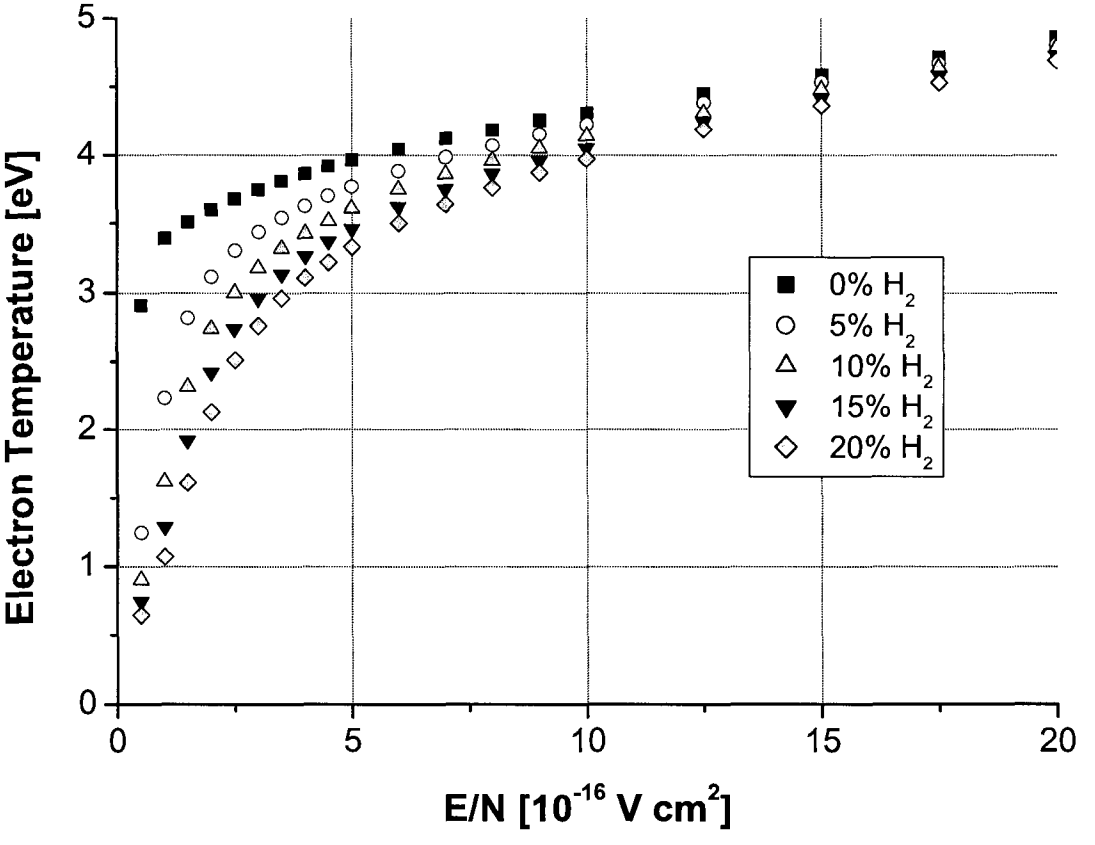

FIG. 47: Electron temperature for an Ar discharge with different amounts of H_2 as a function of the reduced electric field.

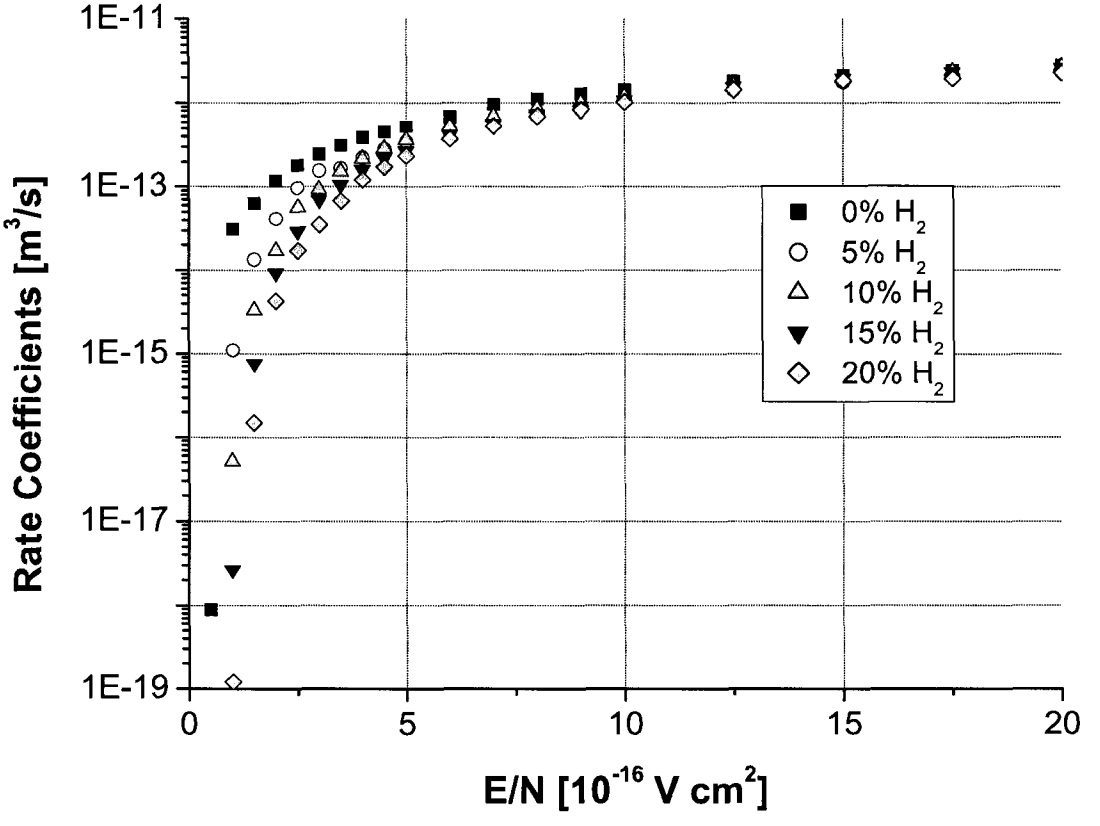

FIG. 48: Electron excitation rate coefficeints for the $4s'[1/2]_1$ state in an Ar discharge with different amounts of H_2 as function of the reduced electric field.

III.3 INFLUENCE OF AIR ON AR/H_2 DISCHARGES

There are a lot of data of Ar/H_2 discharges in the literature. However, studies on Ar/H_2/Air discharges, which are important for plasma-assisted supersonic combustion modeling, are nonexsistent. Thus, we have emoloyed Bolsig and determined the EEDF for a gas discharge containing an initial mixture of 95% Ar and 5% H_2 with different amounts of N_2 at a reduced electric field of 25 Td and present these results in Fig. 49. It is important to state that Bolsig allows only calculation of mixtures of up to three different species. Consequently, we determined separately the EEDF for mixtures of Ar/H_2 either with N_2 or O_2. We see in Fig. 49 that the EEDF decreased by more then two orders of magnitude with increasing amounts of N_2 at energies above threshold (11.55 eV) for electron impact excitation of Ar [64]. This decrease in the number of fast electrons is expected since N_2 has a large number of inelastic excitation processes. At energies between 3 and 11 eV, the decrease of the EEDF is smaller. At energies below 3 eV, the EEDF increases with increasing amounts of N_2. This change at around 3 eV is caused by vibrational energy loss due to the presence of the N_2, which has a high resonant electron-molecule vibrational excitation cross section [64]. This phenomena has been observed in many experiments [65] performed to determine the EEDF for gas mixtures containing N_2. Similar results were found for mixtures of $Ar/H_2/O_2$.

Additionally, we determined how the rate coefficients for different process will be effected by the addition of air to a discharge with an initial mixture containing 95% Ar and 5% H_2 and present these results in Fig. 50. From the figure we see that the rate coefficients for the Ar $4s'[1/2]_1$ state decrease with increasing amounts of both N_2 and O_2. The faster decrease due to the presence of O_2 in the discharge is mainly due to vibrational excitation of O_2. It has been shown [66] that this transition is dominant even in discharges with low concentrations of O_2.

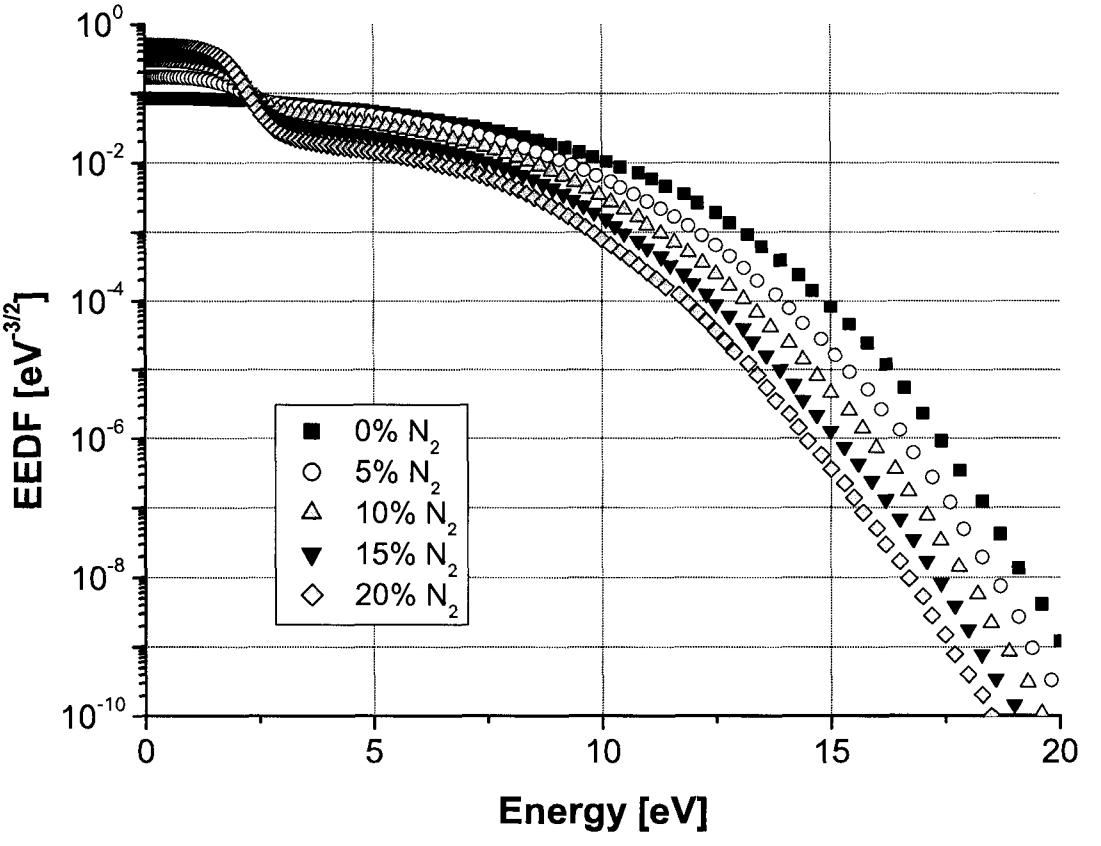

FIG. 49: Electron energy distribution functions for a gas discharge containing an inital mixture of 95% Ar and 5% H_2 with different amounts of N_2 at a reduced electric field of 25 Td as a function of the energy.

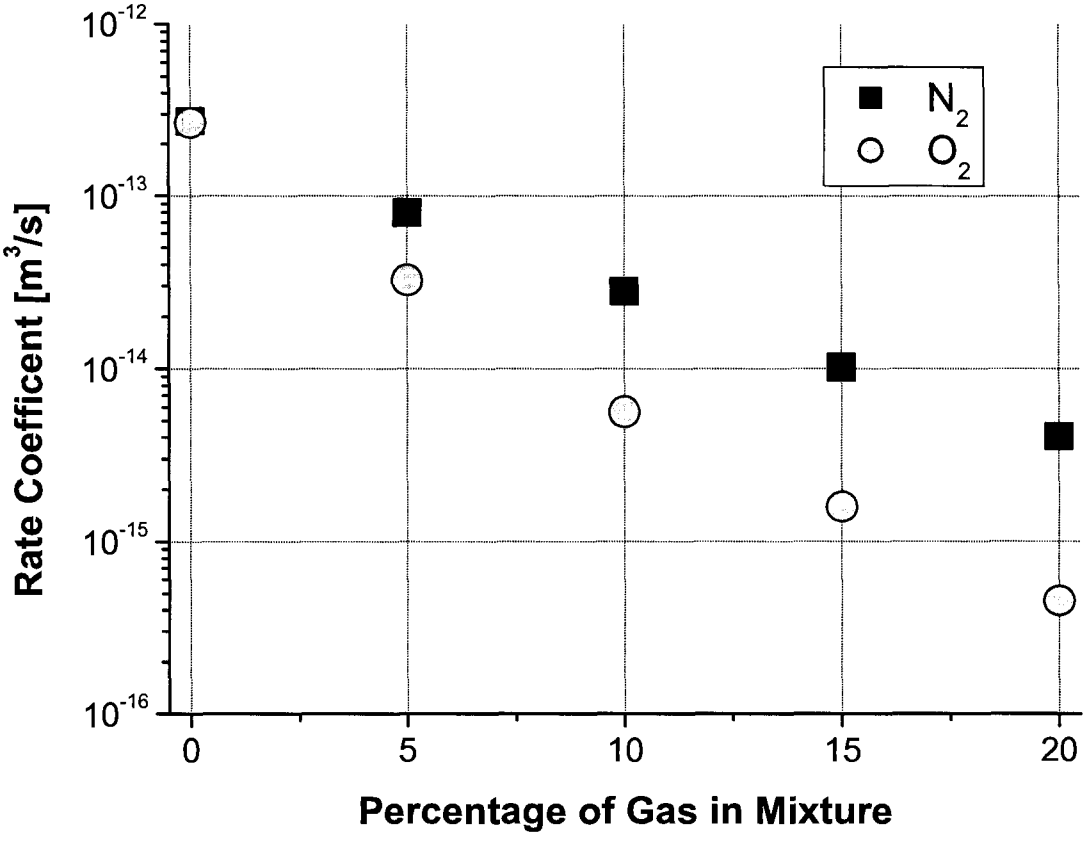

FIG. 50: Electron excitation rate coefficients for the Ar 4s'$[1/2]_1$ state in a gas discharge containing an inital mixture of 95% Ar and 5% H_2 with different amounts of N_2 or O_2 at a reduced electric field of 25 Td as a function of the energy.

CHAPTER IV

MODELING OF MARTIAN ATMOSPHERIC ENTRY CONDITIONS

NASA's Mars exploration program seeks to understand Mars as a dynamic system, including measuring the structure of the upper atmosphere and ionosphere, understanding the past and present climate, and its potential habitability [67]. Since the early 1970s NASA has sent numerous satellites and landers to Mars to accomplish these goals. Each of these probes faced numerous challenges on their long missions. Nearly half of all probes sent to Mars either crashed on the surface or burned up in the atmosphere.

In the case of satellites, one of the most challenging phases of the mission is the aerobraking phase. First used by the Magellan spacecraft while orbiting Venus in 1993 [68] and then by the Mars Global Surveyor in 1997 [69], the satellites skimmed the atmosphere of the planet using the friction between the atmosphere and the satellites to slow their velocity and thus decrease the orbit. This led to a decrease in the orbital radius for the satellite. The major benefit of this process is that the naturally occurring forces were used to decrease the orbit as opposed to a de-orbital burn which involved the use of fuel to ignite the engines. Since less fuel was needed for the mission to get the satellite into orbit, the cost was lower. But this friction also caused heating and ionization of the surrounding atmosphere.

The Mars Landers face many challenges during entry, descent, and landing on the Martian surface. These challenges during the entry and descent phases stem from the fact that Mars' atmosphere is thick enough to create thermal ionization and heating, but thin enough that the terminal descent velocity of a falling object is too high. During the landing phase, the Mars Landers faced many obstacles on the ground, including complex rock, terrain, and dust patterns [70]. One of the main challenges, which each probe faced during entry, is selection of the appropriate entry flight path angle. If the probe failed to enter the atmosphere at the correct angle, it could either burn up in the atmosphere or skip off into space. Thus, the angle of entry is essential to getting the landers safely on the ground. For the Pathfinder Lander, the maximum skipout angle was determined to be -11.2^o. To make sure that the angle of entry was accurate, NASA designed the system so that the worst-case flight path angle was at least 2^o steeper, which was 14.06^o [71].

As mentioned before, during entry the atmosphere will cause sufficient thermal

ionization and heating. Similar to the aerobraking phase for satellites, as a probe entered the atmosphere, the friction between the probe and the atmosphere caused ionization of the surrounding gases. A shock wave formed in front of the probe since it traveled faster then the speed of sound. The interaction between this shock wave and the Martian atmospheric entry plasma (MAEP), as well as similar plasmas, is a phenomenon that has been studied by many groups over the years.

The first report on hypersonic aerodynamic problems during Earth re-entry was by Hermann [25]. He stated how the changes in the altitude and the strong heating at the stagnation point would affect the chemical composition of the air flowing around the probe and eventually cause ionization. In addition, he discussed some results for the interactions of the ionized gas with a shock wave formed by a circular cylinder, sphere, and circular cone. Although this paper was focused on Earth re-entry, it helped to define the types of obstacles that the Mars exploration landers would face during entry. A more comprehensive review of the effects of planetary entry at hypersonic Mach numbers greater then 20 for Earth, Mars, and Jupiter are given in Ref. [72].

Martian entry plasma is a complex mixture consisting of numerous atomic and molecular species such as CO_2, O_2, O, CO, NO, N_2, CN, C_2, N, C, and Ar, ions such as C^+, O_2^+, Ar^+, O^-, CN^+, O^+, CO^+, and NO^+, and electrons. Modeling of these types of plasmas is very calculation intensive. Gorelov *et al.* [27] showed through a comparison of experiments and numerical simulations at shock speeds of 4-9 km/s that to model this type of discharge a weaker dissociation rate for CO_2 molecules, slower ionization rates for C and O atoms by electron impact, and the non-equilibrium distribution of the free electron temperature need to be taken into account for non-equilibrium ionization behind the shock fronts. In an earlier work by Park *et al.* [73], a thermochemical model using the previously identified molecular, atomic, and ionic species was used to show that the vibrational temperature approaches the translational temperature quickly behind the shock front. They concluded that this was caused by the fast relaxation of the vibrational modes of the CO_2 molecules.

In the last ten years, there have been many models and experiments of hypersonic flows in CO_2/N_2 employing a convergent-divergent nozzle to simulate Martian atmospheric entry. Using a thermochemical non-equilibrium Navier-Stokes solver [26, 74, 75], these researchers have shown how the rotational, vibrational, number

density, and molar fractions of the gases vary in a plasma arcjet under specific laboratory conditions. The main problems with these models and experiments are that they do not include argon as a significant constituent in the discharges and they do not take into account the correct geometry of the Mars probes which is important for understanding the interactions of the shock waves.

In this chapter we will describe the atmospheric composition and the free stream pressure, density, and temperature measurements from the NASA Mars Landers. The jump conditions across the shock layer, the parameters within the stagnation region behind the shock front, and the electron density were determined under entry conditions. We also describe a gas kinetic model and gas composition model used for determination of the transport parameters in the discharge and changes in composition of the atmosphere within the discharge region. The influence of water vapor on the model is also discussed.

IV.1 MARTIAN ATMOSPHERIC COMPOSITION

Observations made by several Martian probes and satellites [76] suggest that the atmosphere near the surface is primarily composed of CO_2 with minor components of Ar and N_2, see Table 6. The Viking Landers made measurements of the composition changes in the upper atmosphere between 120 km and 200 km. From this data Nier and McElroy [77] developed a simple model for the number density of the species for each of the Viking Landers. In Table 7 we present the composition changes for the upper atmosphere for Viking Lander 2. one can see that the composition changes greatly with altitude. Then the composition is comparable with that near the surface. Currently, we lack information about the altitudinal changes of the atmospheric composition below 120 km. Thus, we will assume for the present work that the composition changes below 120 km are negligible with altitude.

TABLE 6: Martian atmospheric composition at the surface [76].

Type of Gas	Percentage in Atmosphere
CO_2	95.32
N_2	2.7
Ar	1.6
O_2	0.13
CO	0.07
H_2O	0.03
Ne	0.00025
Kr	0.00003
Xe	0.000008
O_3	0.000003

TABLE 7: Martian atmospheric composition in the upper atmosphere [77].

Altitude	CO_2	O_2	N_2	CO	NO	Ar
125	94.92	0.162	2.37	1.12	0.0062	1.43
150	89.61	0.256	5.57	2.63	0.0145	1.93
175	79.14	0.379	12.24	5.78	0.0318	2.43
200	61.74	0.496	23.78	11.22	0.0618	2.71

In addition to the atmospheric composition, data from the Pathfinder and Viking Landers provide important information about the altitudinal changes in the free stream density and temperature of the Martian atmosphere. The data were taken during the entry phase into the atmosphere which begins at approximately 160 km above the surface and lasts until the parachutes are deployed for landing that is around 9 km. A a total elapsed time for these measurements was approximately 120 s.

The Viking Landers contained two diagnostic tools. The first of these is the Viking Upper Atmospheric Mass Spectrometer (VUAMS), which took measurements of the free stream atmospheric density, pressure, and temperature between 160 km and 130 km [78]. The second is the Viking Atmospheric Structure Instrument (VASI) which provided data from 120 km to 9 km. The Pathfinder Lander had three diagnostic tools, one set in each plane, for upper atmospheric measurements [79]. Each of these tools collected data for the density, pressure, and temperature from 160 km

to 130 km. In the region below 130 km only one of the tools continued to measure the free stream parameters. The free stream density measurements for the Martian atmosphere are shown in Fig. 51.

From Fig. 51 we observe that the Viking measurements are higher then the Pathfinder measurements at higher altitudes. This difference is due to seasonal density changes and diurnal variations within the thermosphere [80]. Two models were constructed for the Pathfinder data using the altitudinal density distribution

$$\rho = \rho_o e^{-\beta h}. \tag{55}$$

Model 1 represents altitudes from 160 km to 60 km with $\rho_o = 0.2447$ km/m^3 and $\beta = 6.6890$ km and model 2 was constructed for altitudes from 60 km to 9 km with $\rho_o = 0.02102$ km/m^3 and $\beta = 9.4894$ km. In addition to the free stream density, the number density of each constituent of the Martian atmosphere was determined from the ideal gas law and is presented in Fig. 52. The change in total number density at 60 km is not as pronounced as in the free stream density.

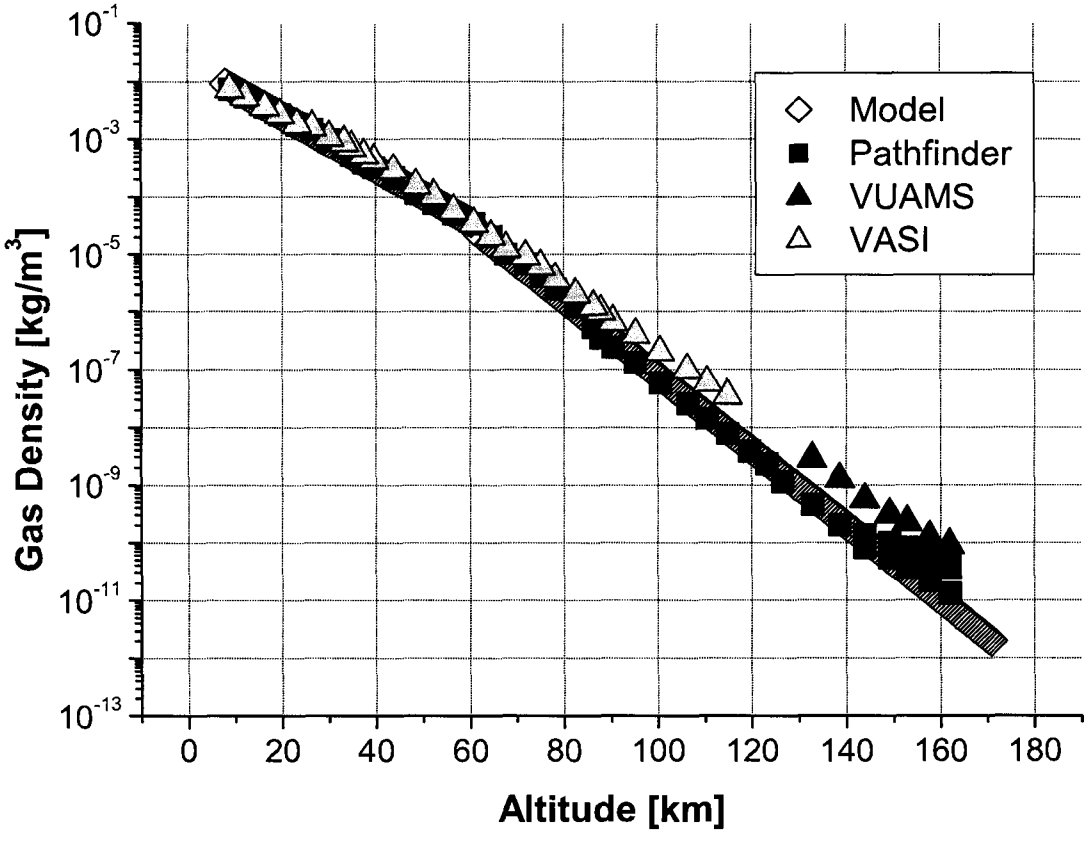

FIG. 51: Free stream density distribution for the Martian atmosphere. Data are take by the Pathfinder Lander that had three sensors in the upper atmosphere to measure the density as indicated by the data points above 140 km.

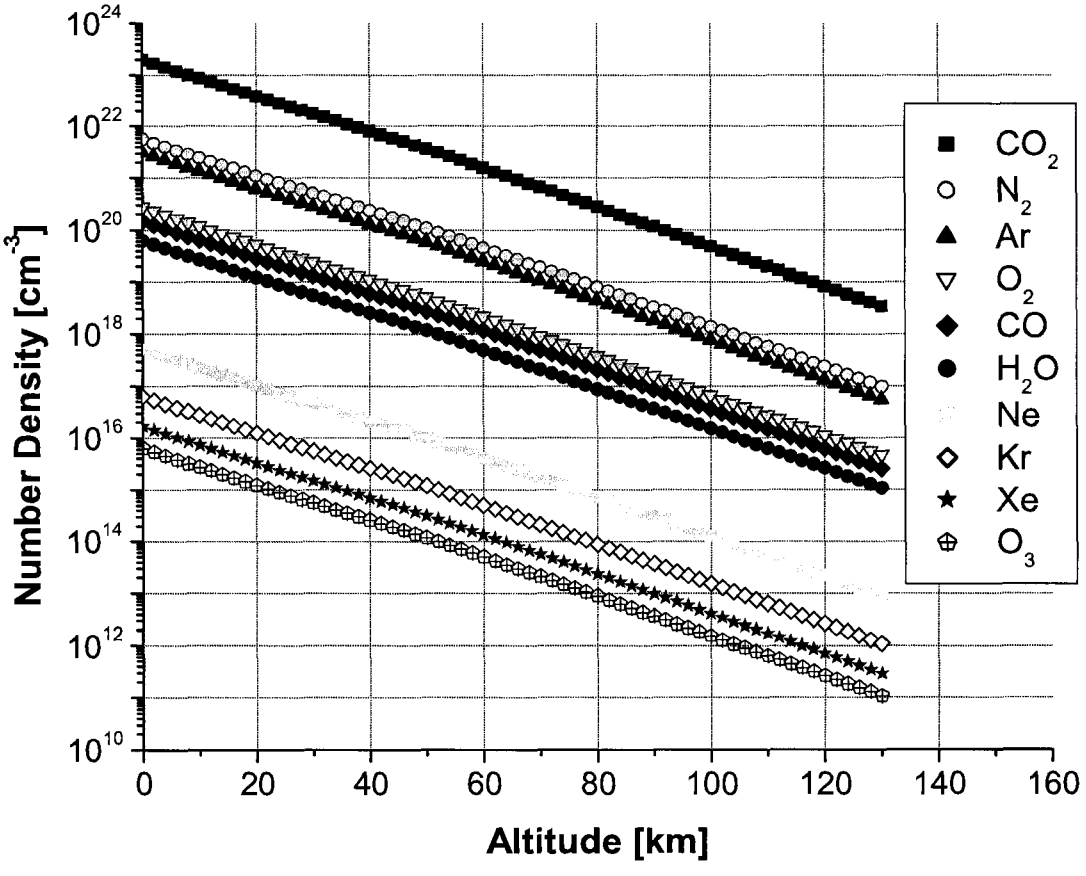

FIG. 52: Number density of the constituents of the Martian atmosphere as a function of the altitude.

The free stream pressure measurements are presented in Fig. 53. From the figure we observed that the Viking and MER Opportunity Landers measured similar values for the atmospheric pressure. On the other hand, the Pathfinder Lander measured pressures that were up to one order of magnitude larger. This difference can be contributed to the seasonal changes in the atmosphere.

Unlike the free stream density and pressure, the temperature measurements were less accurate, see Fig. 54. Two models have been employed to estimate the temperature: Glenn model and the Langley Atmospheric Upwind Relaxation Algorithm (LAURA) [81]. Neither of these models were able to accurately explain the trends in the data. All the data were collected at approximately the same time of year and same distance from the equator. The only known difference in the data collection is from the fact that the Viking data were taken twenty years before the Pathfinder data. For our research we have generated a fitted model for the data that is labeled in the figure (present model). Additionally, we have constructed an upper and lower limit for the temperatures, which can be seen as the shading in the calculations which involve these temperature measurements.

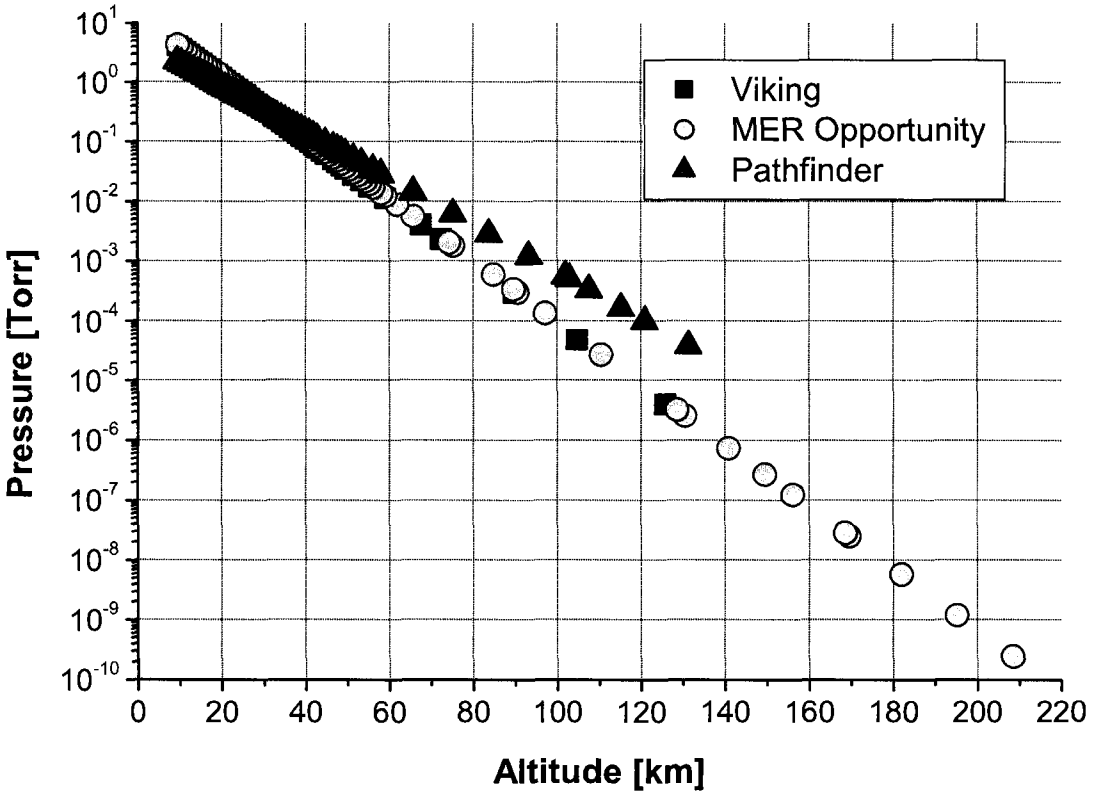

FIG. 53: Free stream pressure measurements taken by different Mars Landers.

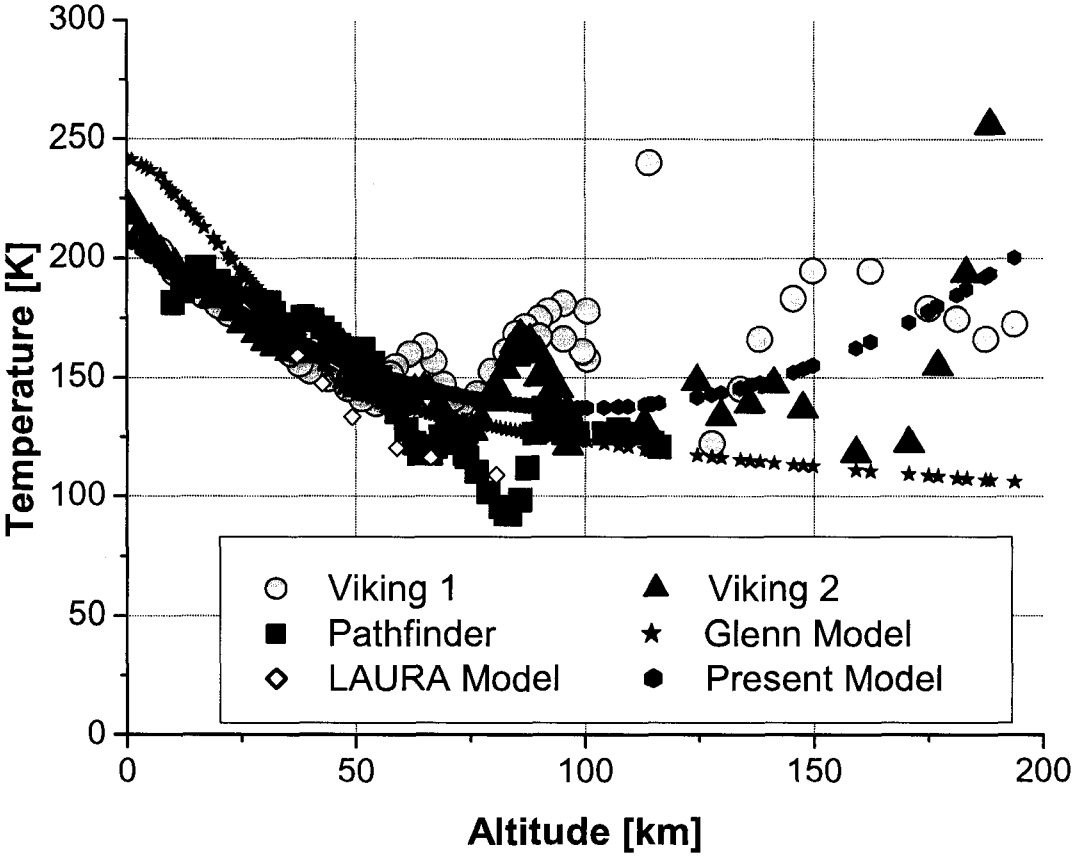

FIG. 54: Free stream temperature measurements for taken by different Mars Landers along with two current models.

IV.2 MARTIAN PROBE TRAJECTORY

By reconstructing the entry trajectory of the Martian probes we are able to develop an accurate portrait of all the atmospheric phenomena faced by them and presented in Fig. 55. We have reconstructed the velocity measurements for each of the listed probes. We note that the velocity was constant down to an altitude of 50 km. The velocity then dropped sharply over the next 40 km due to an increase in the atmospheric density, see Fig. 51. At an altitude of approximately 9 km the parachutes were deployed for each of the probes.

We also reconstructed a velocity profile for the MER Sprit Lander. Due to the closeness of the data for this lander with that of the MER Opportunity, we will use the MER Opportunity data in the following part of this dissertation. It is important to note that although there is sufficient velocity data for reconstruction of the trajectory of the MER Landers, there are no free stream temperature or density measurements.

We determined the Mach number (M) for each probe by using Eq. (4) and we present these calculations in Fig. 56. For the Martian atmosphere, the speed of sound (a_s) is

$$a_s = \sqrt{\frac{\gamma RT}{m_m}} \tag{56}$$

where γ is the specific heat ratio, R is the universal gas constant, m_m is the molecular mass, and T is the temperature from Fig. 54. From Fig. 56 we observe that the Mach number increased as the probes entered the atmosphere with a peak values of 42, 31, and 25 for the Pathfinder, MER Opportunity, and Viking Landers, respectively. After these higher values the Mach number has a sharp decrease due to an increase in atmospheric density. In our experiment the Mach number was determined to be about 2.15. According to Fig. 56, that correspond to value of at about 10 to 13 km above the Martian surface. Therefore, comparison of the experimental data to the model will be done with values in this interval.

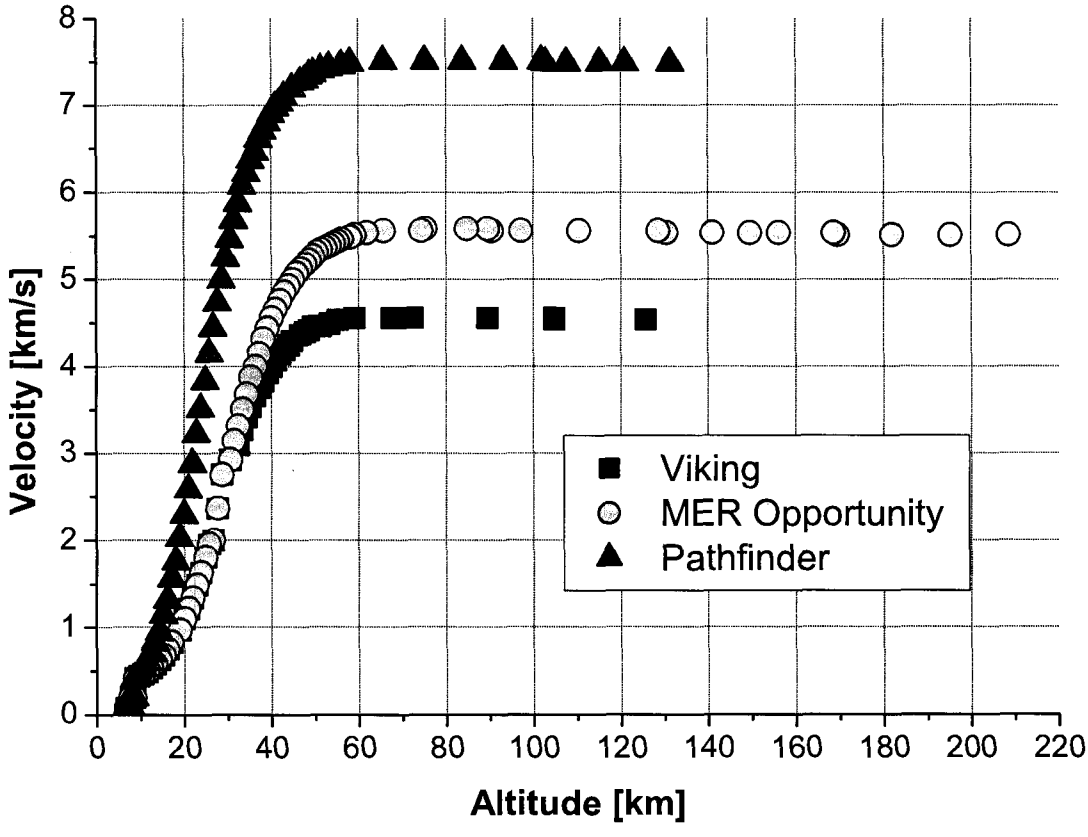

FIG. 55: Reconstructed velocity profiles for Pathfinder, Viking, and MER Opportunity Landers.

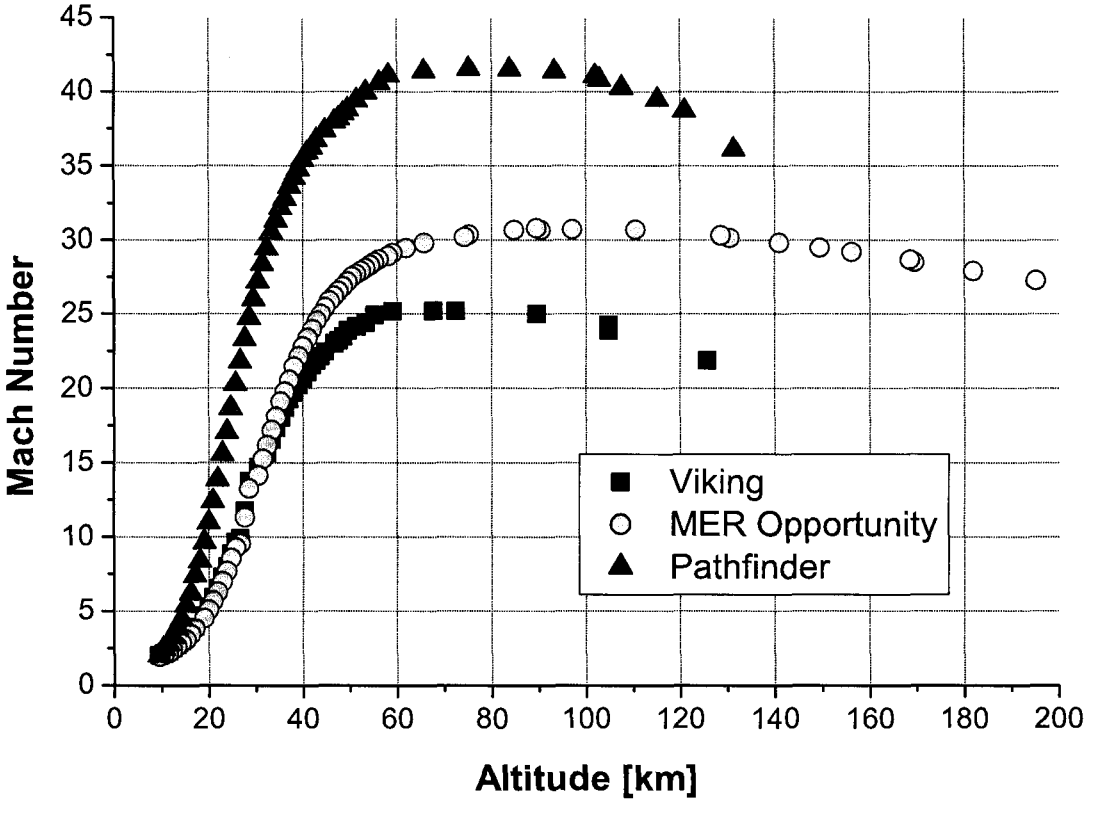

FIG. 56: Calculated values of the Mach number for the Viking, Pathfinder, and MER Opportunity Landers.

In order to determine accurately the gas composition and electron density for Martian atmospheric entry plasma (MAEP), we constructed a model for the shock region in front of each probe during entry. We introduce the following assumptions [82]: the gas mixtures generated during entry are thermodynamically perfect gases, ionization occurs instantly behind the shock front, the gas mixtures are constant in the boundary layer behind the shock front, and gas parameters are defined by the free stream parameters and the relations across the shock. With these assumptions, we calculated the shock parameters:

$$\frac{\rho_2}{\rho_1} = \frac{(\gamma+1)\mathrm{M}_1^2 \sin^2\beta}{(\gamma-1)\mathrm{M}_1^2 \sin^2\beta + 2} \tag{57}$$

$$\frac{T_2}{T_1} = 1 + \frac{2(\gamma-1)}{(\gamma+1)^2}\left(\frac{\mathrm{M}_1^2 \sin^2\beta - 1}{\mathrm{M}_1^2 \sin^2\beta}\right)(\gamma \mathrm{M}_1^2 \sin^2\beta + 1) \tag{58}$$

$$\frac{p_2}{p_1} = 1 + \frac{2\gamma}{\gamma+1}\left(\mathrm{M}_1^2 \sin^2\beta - 1\right) \tag{59}$$

$$\mathrm{M}_2^2 \sin^2(\beta-\theta) = \frac{\mathrm{M}_1^2 \sin^2\beta + [2/(\gamma-1)]}{[2\gamma/(\gamma-1)]\,\mathrm{M}_1^2 \sin^2\beta - 1} \tag{60}$$

where the subscripts 2 and 1 refer to the parameters on the forward and back side of the shock front, respectively, γ is the specific heat ratio, T is the atmospheric temperature from Fig. 54, p is the atmospheric pressure from Fig. 53, ρ is the atmospheric density from Fig. 51, and β is the oblique shock angle calculated by

$$\tan\theta = 2\cot\beta\left[\frac{\mathrm{M}_1^2 \sin^2\beta - 1}{\mathrm{M}_1^2(\gamma + \cos 2\beta) + 2}\right] \tag{61}$$

where β and θ are the angles defined in Fig. 57. For each of the three Mars probes studied here, θ was approximated as 70^o.

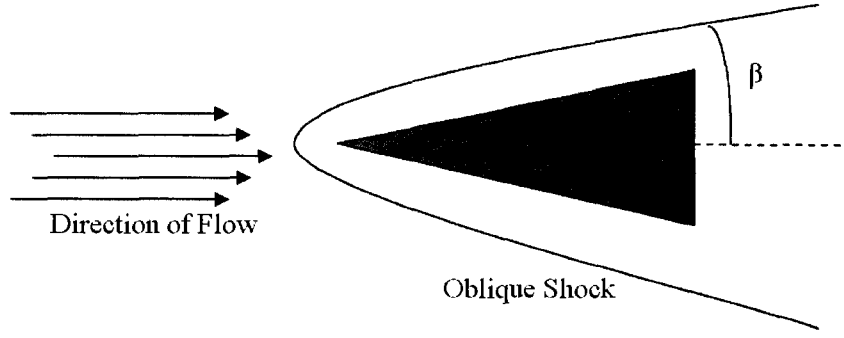

FIG. 57: Diagram of the oblique shock angle.

The calculated density across the shock layer, jump density, is given in Fig. 58. We calculated these values using Eq. (57) in which the specific heat ratio of the Martian atmosphere is 1.29 and the oblique shock angle for all three probes was 78.9^o as calculated with Eq. (61). We observe in Fig. 58 that the density increases constantly as the altitude decreases. Then at about 20 km above the surface, the density begins to decrease as well.

The jump pressure was calculated using Eq. (59) and the results are presented in Fig. 59. We observe that the pressure peaks at about 30 km above the surface for all three probes with a value of 150 Torr for Pathfinder and 95 Torr for Viking and MER Opportunity. The pressure then begins to decrease as the probes approach the 9 km limit where the parachute is deployed. Note that at the surface of Mars the atmospheric pressure is approximately 5 to 8 Torr depending upon the season.

The jump temperature was calculated employing Eq. (58) and presented in Fig. 60. We observe that the temperature reaches a peak average value of about 36000 K, 19000 K, and 13000 K for the Pathfinder, MER Opportunity, and Viking Landers, respectively. These maximum values occurred between 50 and 60 km above the surface. The shaded regions give us a range of values for the temperature. For example, the Pathfinder Lander will have a peak temperature of 36000 K $\pm$ 2500 around 60 km. At higher altitudes all the distributions become wider since the atmosphere becomes less dense.

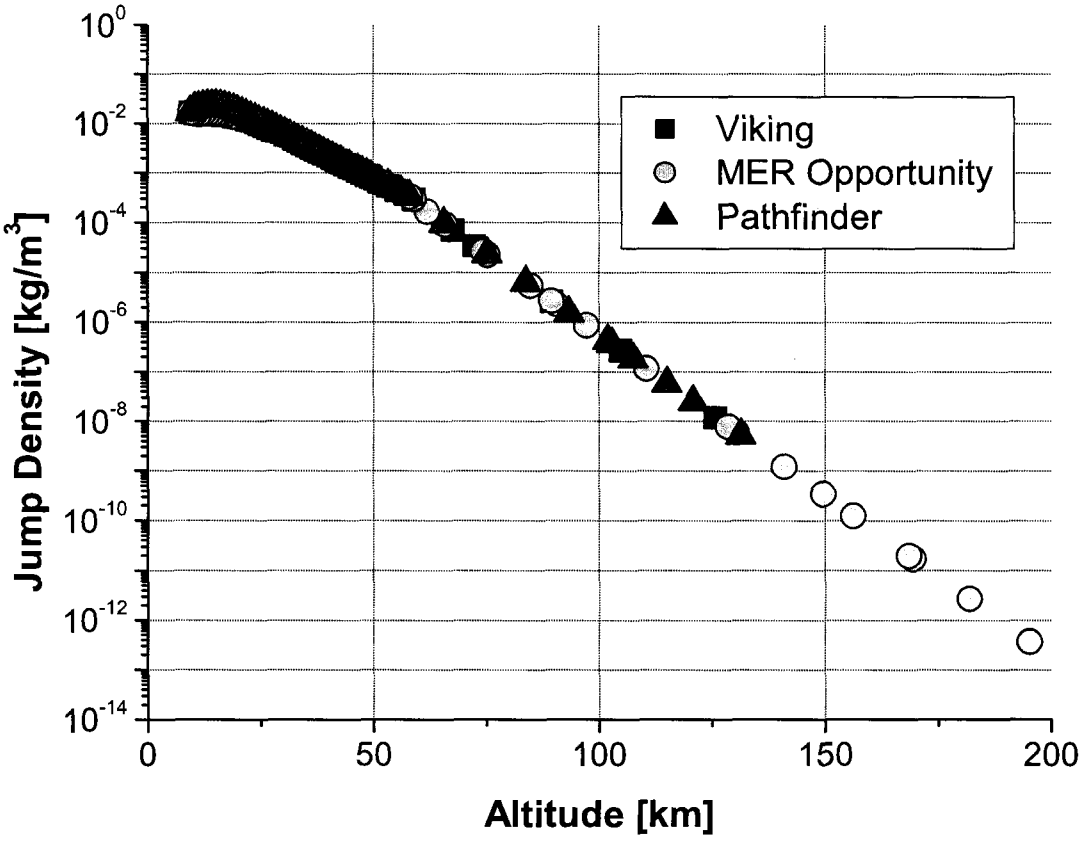

FIG. 58: Gas density across the shock front in MAEP from data of the Mars Pathfinder, Viking, and MER Opportunity Landers.

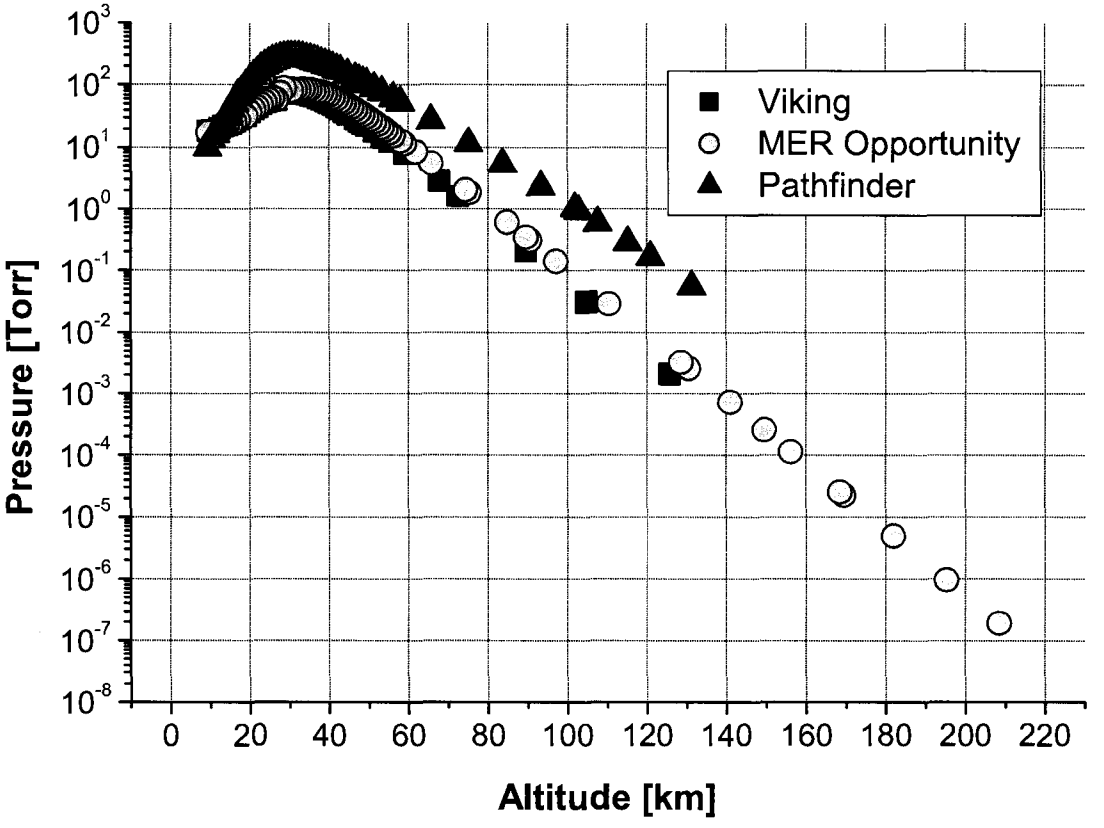

FIG. 59: Jump pressure for MAEP for the Mars Pathfinder, Viking, and MER Opportunity Landers.

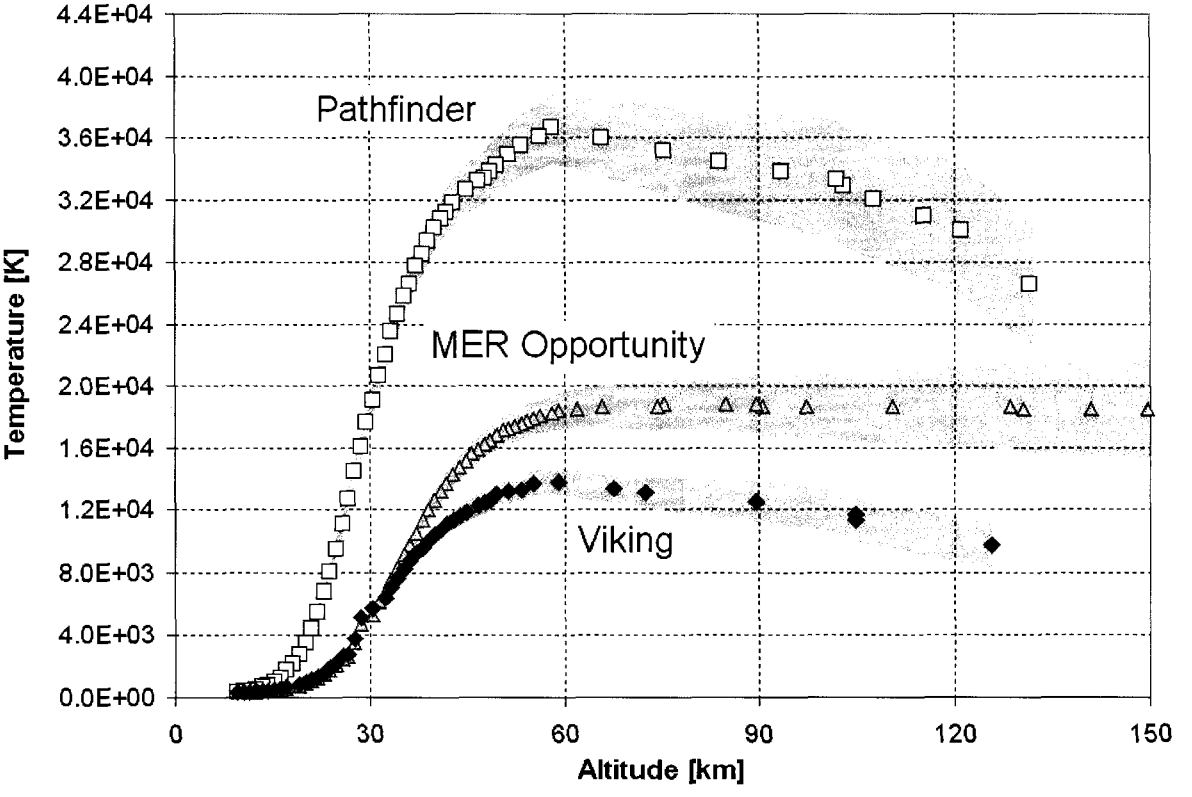

FIG. 60: Temperature across the shock layer in the MAEP. The shaded region is due to the error in the measurement of the free stream temperature data.

IV.2.1 Stationary Shock Wave Parameters

During the entry phase, there will be a region between the probe and the shock front known as the stagnation point region. In this region the temperature, pressure, and density will be orders of magnitude greater than in the rest of the flow since the velocity of the gas in this region will be much lower then in the surrounding flow, $v \rightarrow 0$. To determine how each of these parameters vary within the stagnation region during entry, we used the following equations [32]

$$\frac{T_o}{T} = 1 + \frac{(\gamma - 1)}{2}\mathrm{M}^2 \tag{62}$$

$$\frac{p_o}{p} = \left(1 + \frac{(\gamma - 1)}{2}\mathrm{M}^2\right)^{\gamma/(\gamma-1)} \tag{63}$$

$$\frac{\rho_o}{\rho} = \left(1 + \frac{(\gamma - 1)}{2}\mathrm{M}^2\right)^{1/(\gamma-1)} . \tag{64}$$

The pressure in the stagnation region was calculated using Eq. (63) and results are presented in Fig. 61. From this figure we notice that the pressure peaks at around 40 km where as the jump pressure had a peak at 30 km above the surface. In addition, it is obvious from this graph that the peak pressure is nearly 5 orders of magnitude greater then in the rest of the flow.

The density in the stagnation region was calculated from Eq. (64) and the results are presented in Fig. 62. In the figure we observe that the stagnation density has a peak at 40 km with a value of about 7000 kg/m^3 which is five orders of magntiude greater then the jump density. The density then decreased to an altitude of 9 km where it was equivalent to the jump density. Similar results were found for temperature in the stagnation region.

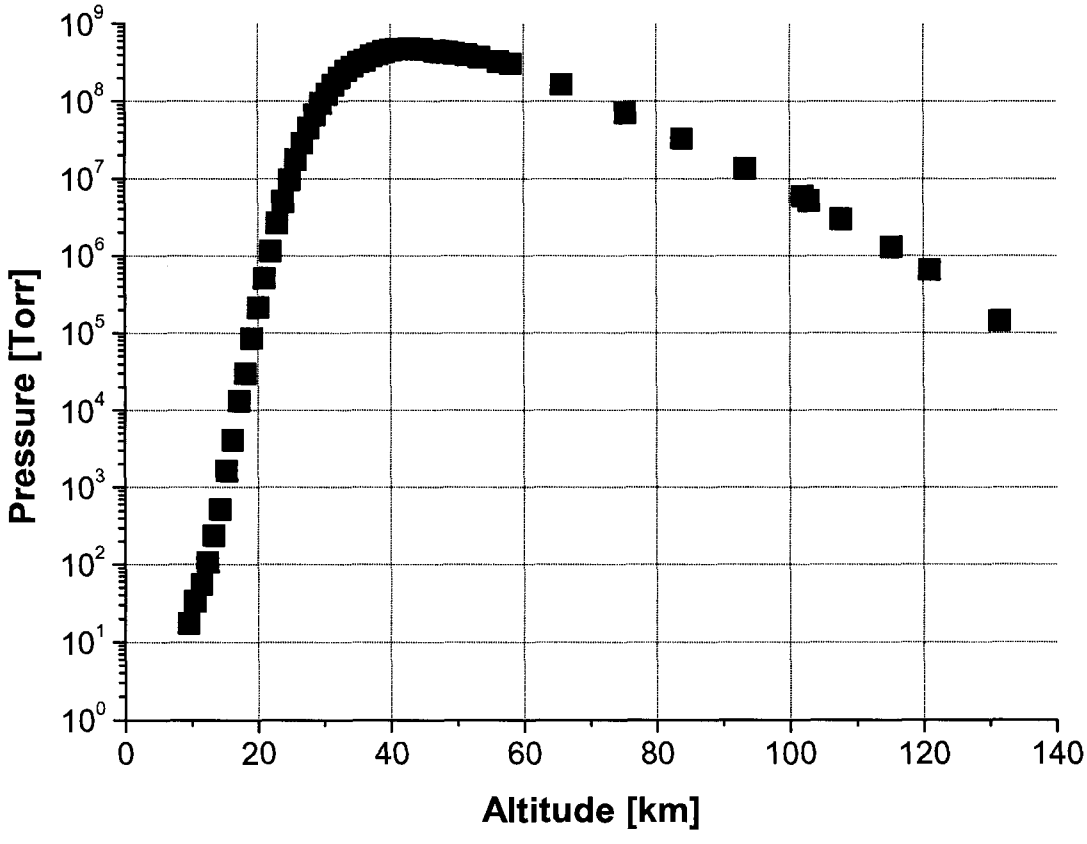

FIG. 61: Stagnation pressure for Pathfinder Lander during entry into the Martian atmosphere.

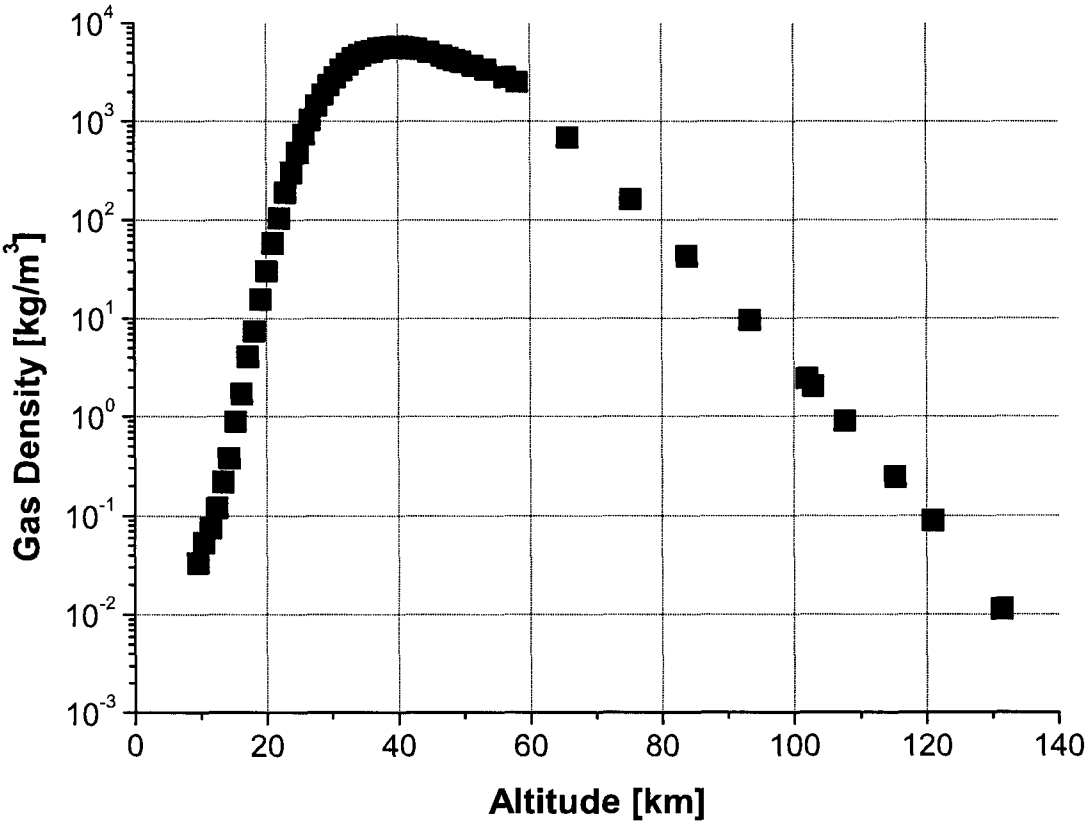

FIG. 62: Stagnation gas density for Pathfinder Lander during entry into the Martian atmosphere.

IV.2.2 Electron Density in Martian Atmospheric Entry Plasma

The electron density was evaluated by using the Saha equation,

$$\log \frac{N_e N_{ik}}{N_k - N_{ik}} = -5040 \frac{\varepsilon_k}{T_e} - 1.5 \log \frac{5040}{T_e} + 26.9366 + \log \frac{2 g_{ki}}{g_{k0}} \tag{65}$$

where N_{ik} is the number density of ions from species k, N_k is the neutral species density, e_k is the ionization potential of species k, g_{ki} is the statistical weight of the ion species k, and g_{k0} is the statistical weight of the neutral species k. In this model we have assumed that the electron temperature (T_e) is equivalent to the gas temperature obtained in Fig. 60. We must also assume that the gas temperature is still high enough that we can neglect the effects of the interactions of the ions with other species in the plasma [82].

Since Martian air is composed of many constituents, this calculation is very complex. We see in Table 6 that the main constituents of the Martian atmosphere are CO_2, N_2, and Ar. During ionization, the major additional neutral species will be O_2, O, CO, and NO. The number densities of the other neutral species mentioned in the introduction for this chapter are negligible in comparison with the densities of these seven species. As such, we have reduced the number of equations needed to find the electron density by assuming that CO_2, N_2, Ar, O_2, O, CO, and NO will be the seven dominant species in the discharge.

To calculate the electron density, we start by assuming a value for the electron density and then calculate N_{ik} applying Eq. (65). Then we apply

$$N_e = \sum_k N_{ik} \tag{66}$$

to recalculate the electron density and repeat this process. Due to the fast convergence of this method, we are able to calculate the electron density fairly quickly. Data shown in Fig. 63 where we observe that the electron density for all three probes is the same at altitudes above 50 km. Below this point we found that the Pathfinder results were orders of mangitude different from the Viking and MER Opportunity results. In addition, we observe a distribution in the electron densities, shown by the shaded region in the figures. This distribution was due to the variations in the free stream temperature measurements.

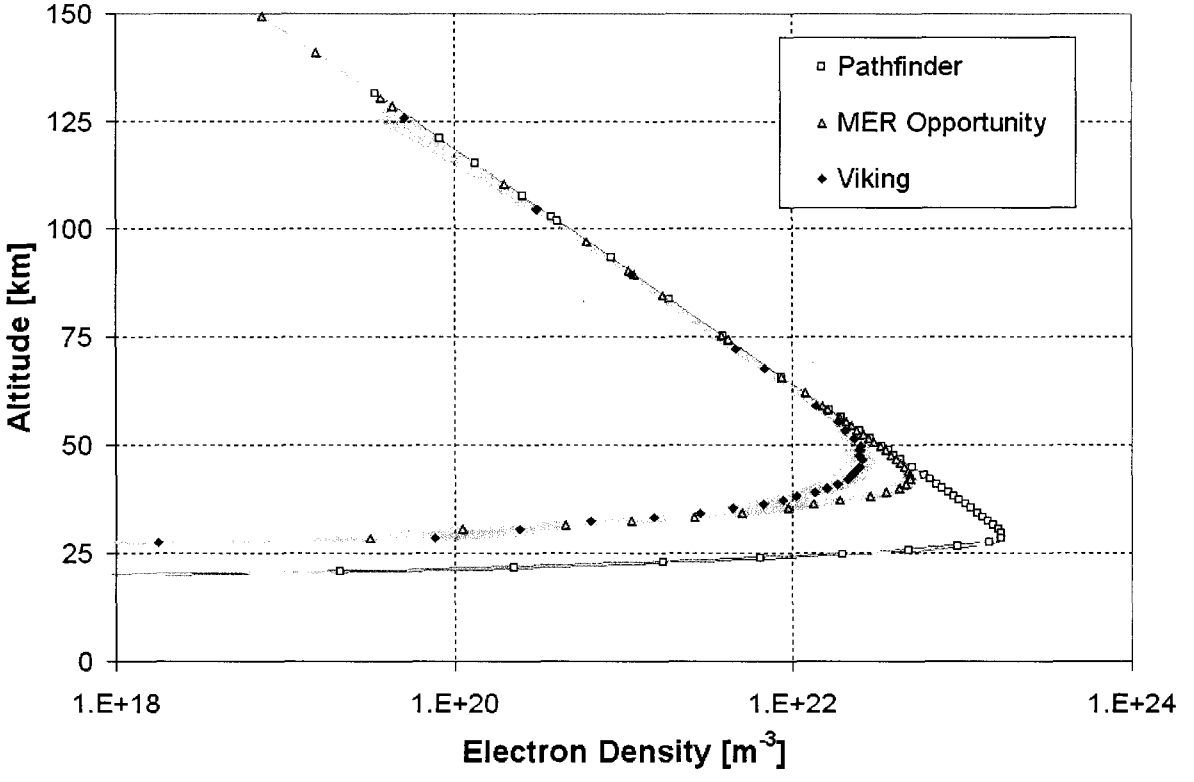

FIG. 63: Calculated values of the electron density for MAEP. The shaded regions are due to the error in the measurements of the free stream temperature data [67].

The main problem with this approach to calculating the electron density is that the assumption that the plasma is in thermal equilibrium at the shock fronts. Several papers [26, 27, 75] have discussed the possibility that the plasma is not in thermal equilibrium. Therefore, for a first approximation, we have estimated the electron temperature by assuming that it will be equivalent to some constant times the gas temperature. Thus we assumed that the electron temperature is two times the gas temperature. For comparison we have calculated the electron density assuming that the electron temperature is half of the gas temperature. In Fig. 64 we see that at the higher altitudes, above 40 km, the electron density does not vary by much. However, below 40 km it can vary by three or four orders of mangitude. We next compared these results with the results for the electron density from the experiment, presented in section II.3.5. We observe from Fig. 65 that the electron density in the experiment is very close the value we determined from the model when the electron temperature was an order of magnitude greater then the gas temperature.

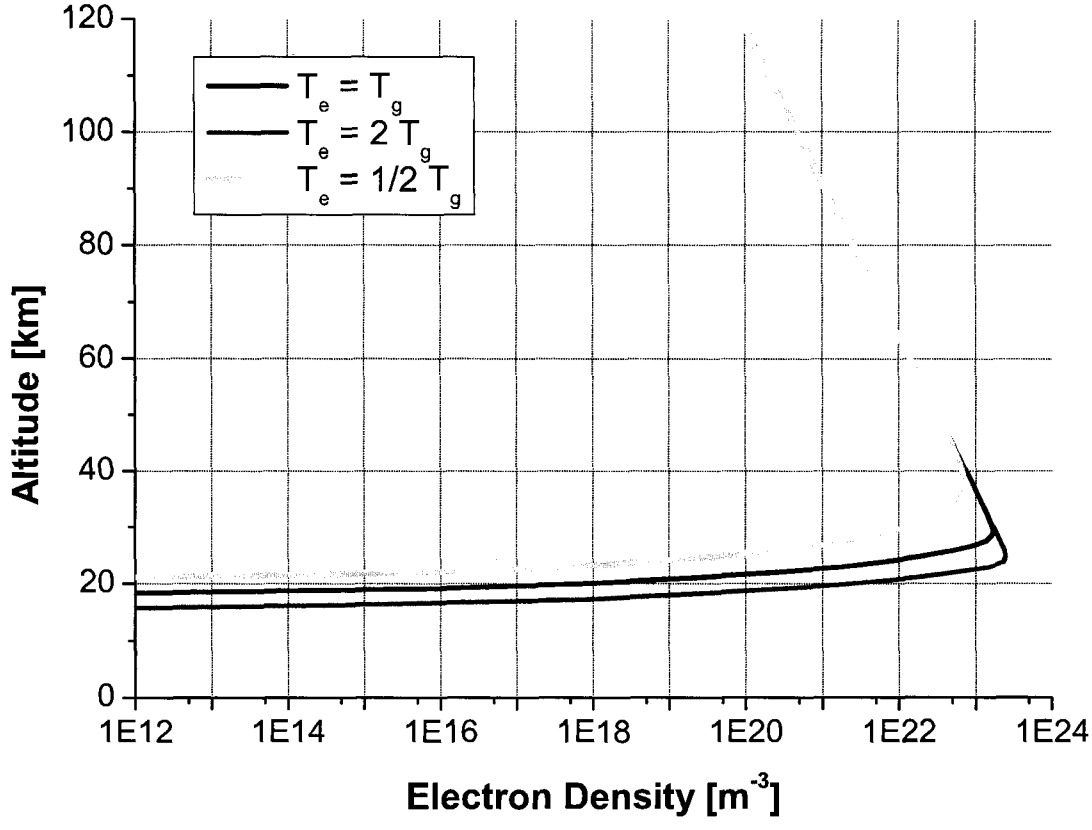

FIG. 64: Calculated values of electron density for MAEP for the Pathfinder probe assuming both thermal and non-equilibrium [67].

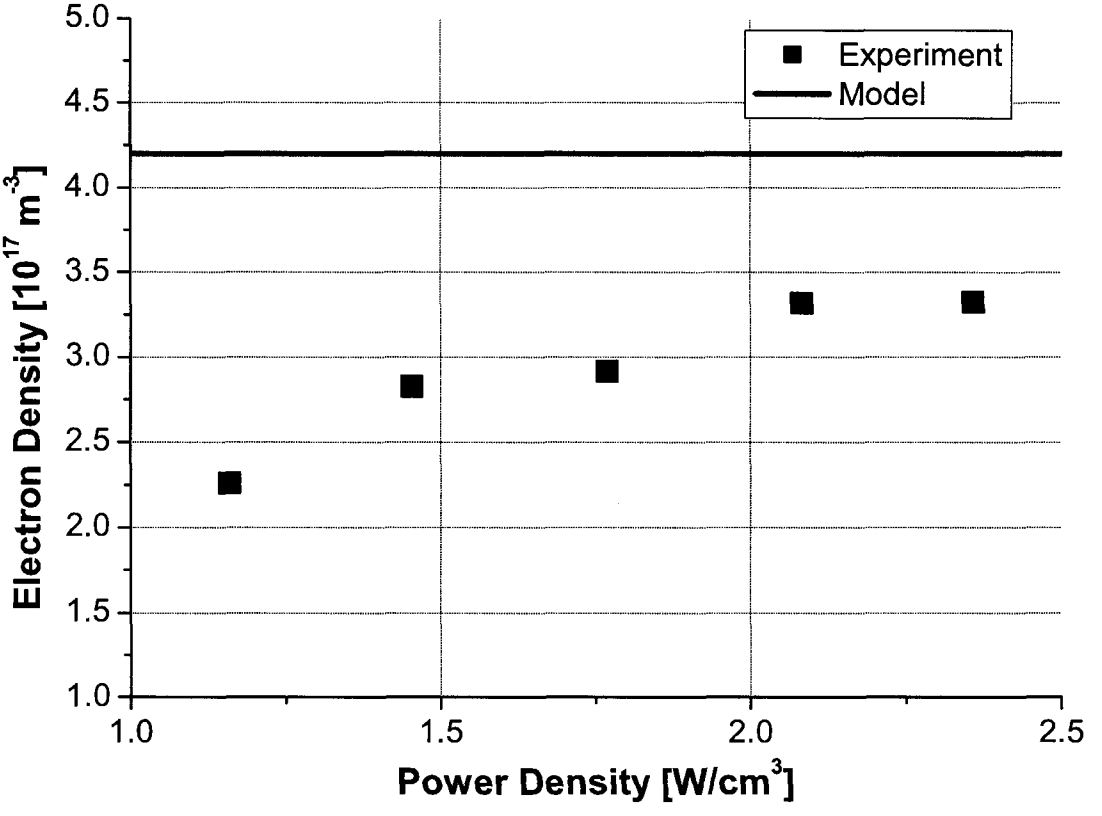

FIG. 65: Comparision of electron density measurements from experiment with the model for MAEP when the electron temparture was assumed to be an order of magnitude greater then the gas temperature.

IV.3 GAS KINETIC MODELING OF MARTIAN ATMOSPHERIC ENTRY PLASMA

In section III.1, we discussed the use of the Boltzmann transport equation for gas kinetic modeling of an Ar/H_2/air discharge. A similar approach was taken for modeling of Martian atmospheric entry plasma. The boundary conditions in Eq. (52) correspond to the typical Martian entry geometry as well as to the experimental arrangement. From Figs. 51 and 56, we see that the density of the Martian atmosphere is very low at high altitudes, while the Mach number of the entry vehicles are very large. The production of electrons at these altitudes within the shock layer can have significant effects on some of properties of the gas [83]. Kinetic modeling of the Martian atmosphere is essential for detailed understanding of the influence of electrons on both aerodynamic quantities and transport parameters in the the discharge.

As mentioned previously the dominant species for Martian atmospheric entry plasma are CO_2, N_2, Ar, O_2, O, CO, and NO. In reactive plasmas the cross sections of the gas mixture vary on the time scale of the experiment and the whole computational process has to account for these changes. Fig. 66 shows the momentum transfer cross sections for most of these species.

The EEDF for a mixture 95.7% CO_2, 2.8% N_2, and 1.5% Ar was calculated employing Bolsig. We present the results in Fig. 67 for a reduced electric field of 25 Td, or 2.5×10^{-16} V cm^2, at a temperature of 300 K. As a comparison we calculated the EEDF for terrestial air. Then, applying Eq. 54, we calculated the average electron temperature at various values of E/N for terrestrial air and Martian air and present the results in Fig. 68. We observe that T_e increases almost linearly with E/N values great then 4×10^{-16} V cm^2. Below this point, the values for terrestrial air decrease very slowly and are almost constant, while the values for Martian air continue to decrease linearly.

The dissociation rate coefficients were then determined for CO_2 and O_2 from Eq. (53). In Fig. 69 we see that the dissociation of both species is very fast at the higher values of E/N. At the lower values of E/N we notice that the rate coefficients decrease expontially. Thus, for CO_2 the rate coefficient drops from 10^{-11} cm^3/s at 4×10^{-16} V cm^2 down to 10^{-15} cm^3/s at 2×10^{-16} V cm^2.

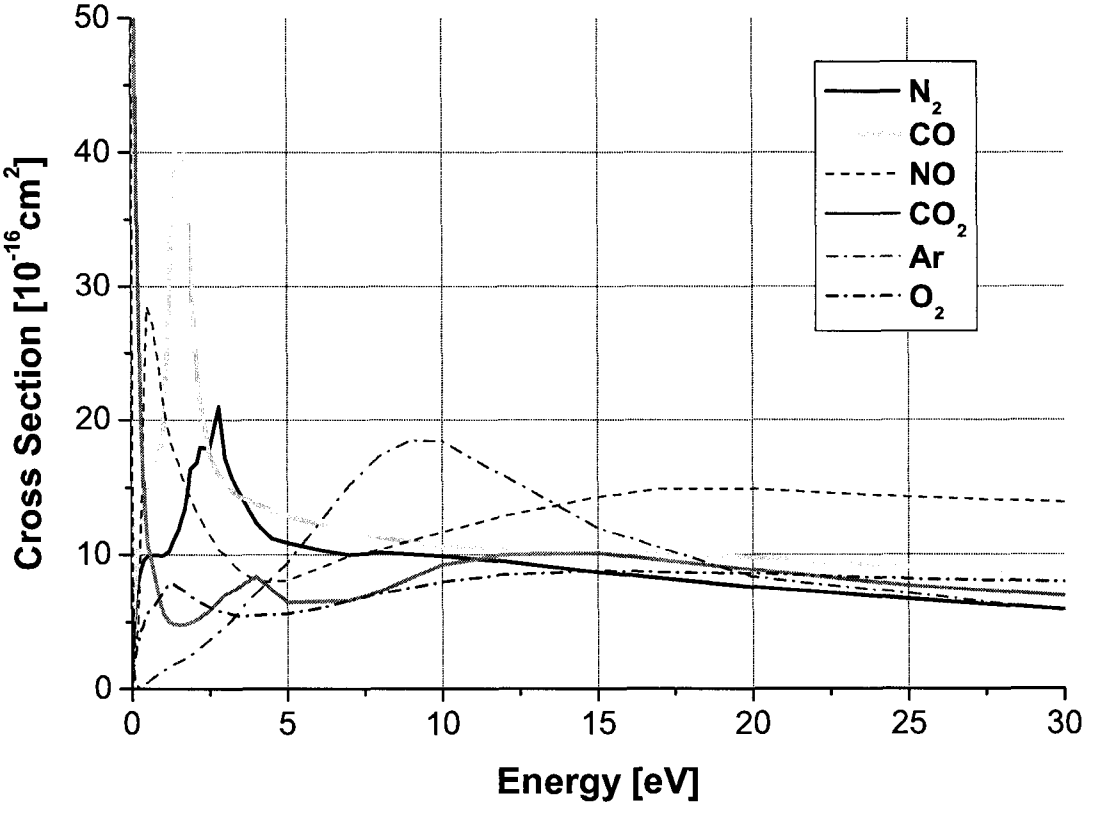

FIG. 66: Momentum transfer cross sections for CO_2, N_2, Ar, O_2, CO, and NO.

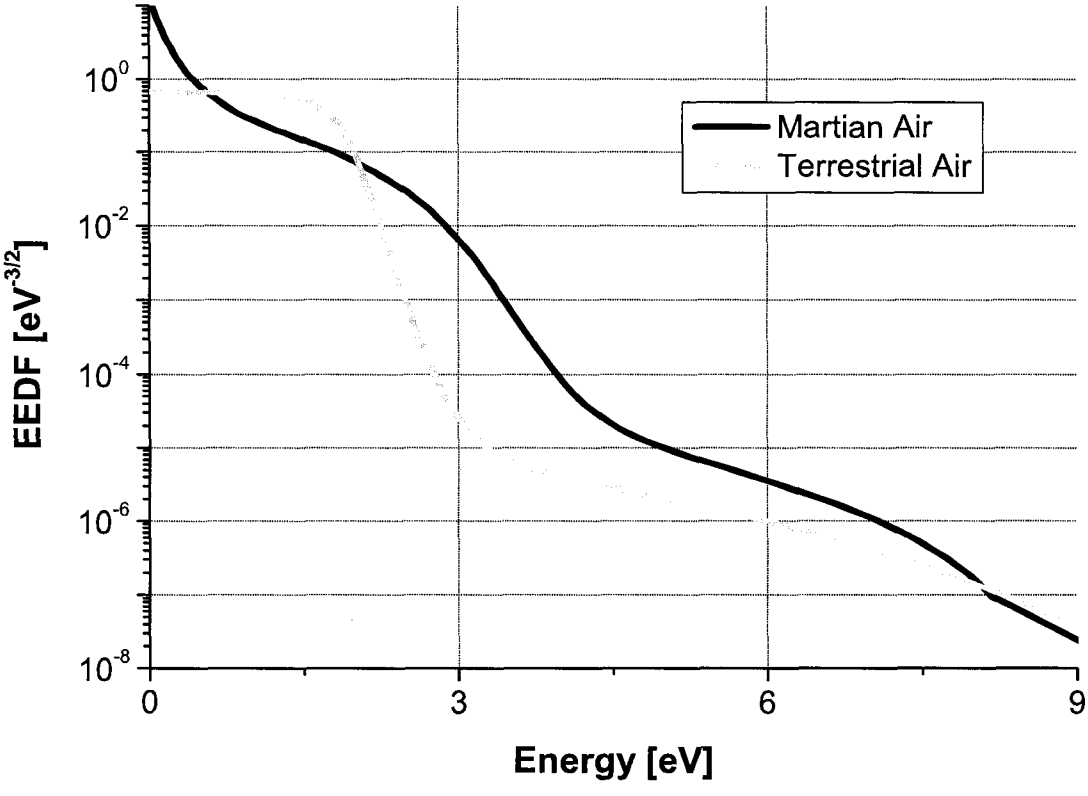

FIG. 67: Electron energy distribution functions for Martian simulated gas and terrestrial air for a reduced electric field of 25 Td and a temperature of 300 K.

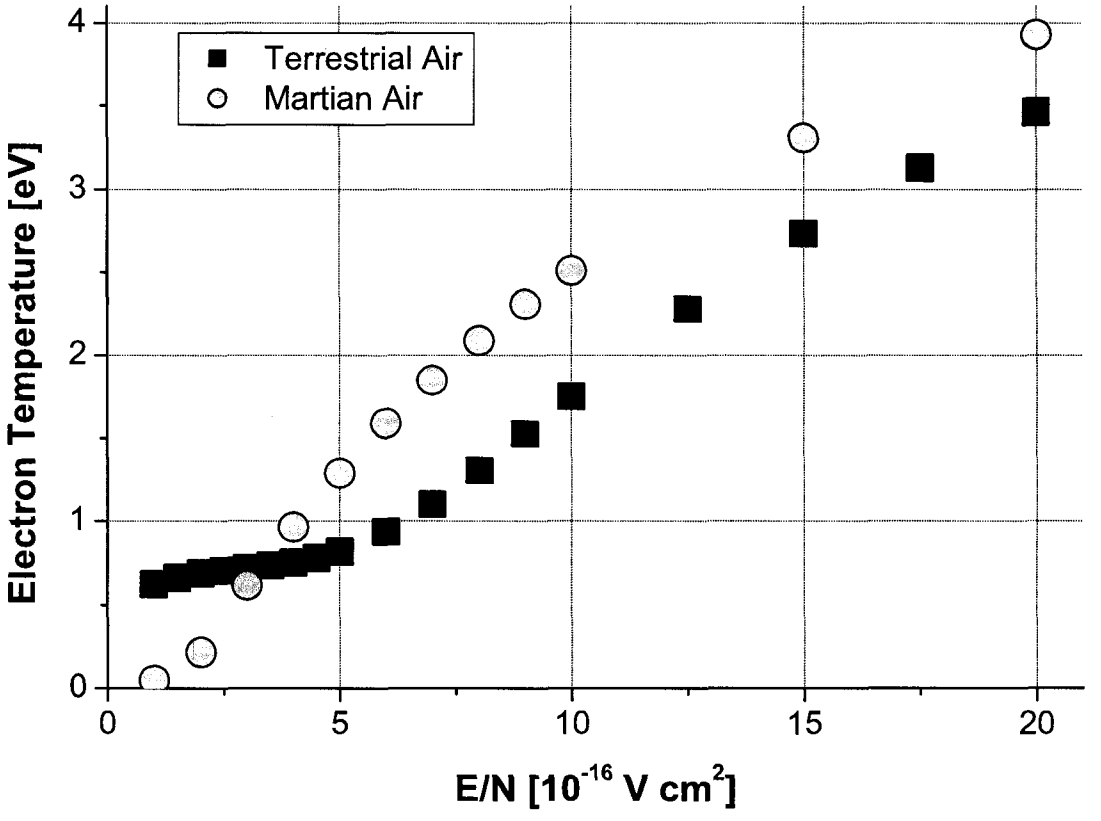

FIG. 68: Electron temperature as a function of the reduced electric field for Martian simulated gas and terrestrial air.

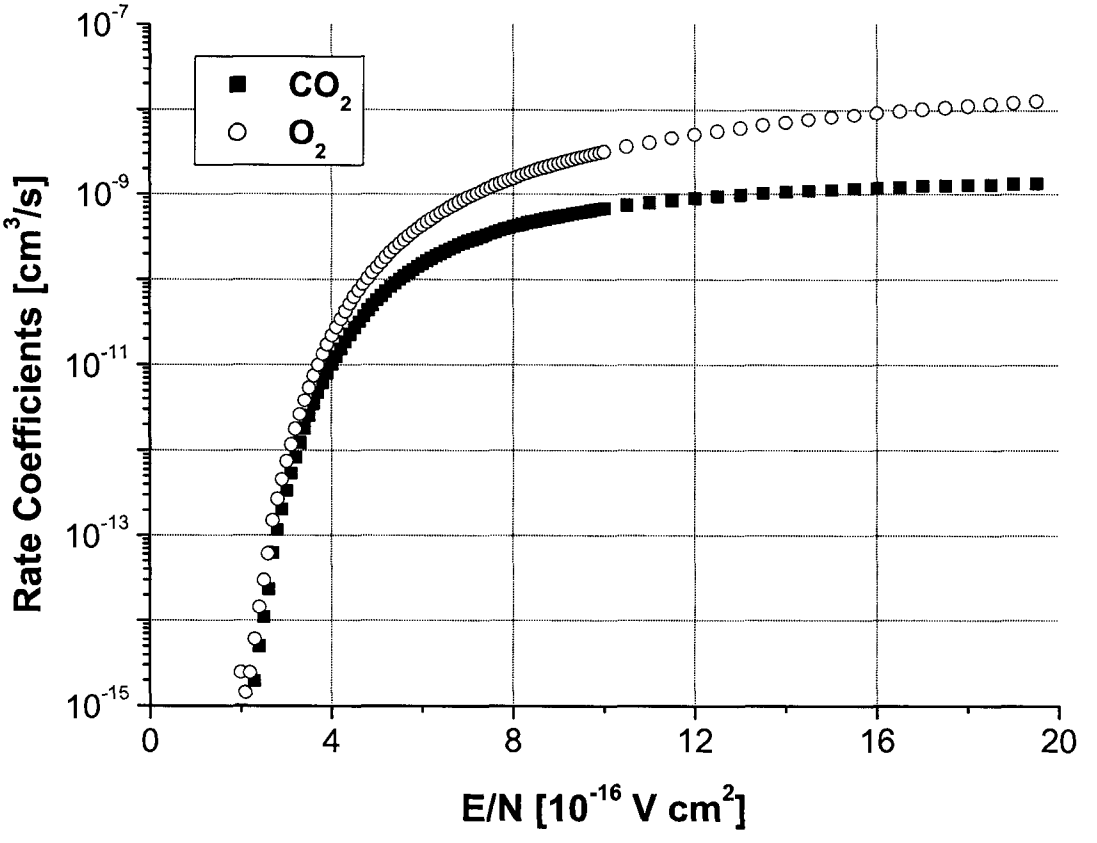

FIG. 69: Dissociation rate coefficients for CO_2 and O_2 in MAEP.

IV.3.1 Gas Phase Reactions and Rate Equations

The most probable gas reactions that affect the production and destruction of the neutral species in MAEP are listed in Table 8. A more comprehensive list of the reactions can be found in a paper by Park *et al.* [73]. In our model the reactions including N_2 have not been taken into account since N_2 acts as a buffer gas in this discharge and thus does not react with the other species. Reactions with Ar have also not been included in this model since it is a noble gas which comprises less the 2% of the total volume. A more detailed explanation can be found in Ref. [5].

In our model we have excluded all the carbonic and oxygen containing ions, along with CN^+, C_2^+, Ar^+, N^+, and N_2^+ since their concentrations are very small in comparison to their neutral counterparts [84]. As such, they do not play a significant role in the rate processes. The only ion which will play any part is the O^- ion which has an active role in the production and loss of the neutral species.

TABLE 8: List of major gas reactions in simulated MAEP.

No.	Reaction	Rate Coefficient	Ref.
Dissociation			
R1	$e + CO_2 \rightarrow CO + O + e$	$k_1 = f(E/N)$	Fig. 69
R2	$e + O_2 \rightarrow 2O + e$	$k_2 = f(E/N)$	Fig. 69
R3	$e + O_3 \rightarrow O^- + O_2$	$k_3 = 1 \times 10^{-8}\ cm^3/s$	[84]
Reformation			
R4	$O + O_3 \rightarrow 2O_2$	$k_4 = 4.6 \times 10^{-14}\ cm^3/s$	[84, 85, 86]
R5	$O + O + M \rightarrow O_2 + M$	$k_5 = 8 \times 10^{-33}\ cm^6/s$	[84, 87]
R6	$O + O_2 + M \rightarrow O_3 + M$	$k_6 = 5 \times 10^{-34}\ cm^6/s$	[86, 88]
R7	$O^- + CO \rightarrow CO_2 + e$	$k_7 = 7 \times 10^{-10}\ cm^3/s$	[89, 90, 91, 92]
R8	$O^- + O \rightarrow O_2 + e$	$k_8 = 2 \times 10^{-10}\ cm^3/s$	[84, 89, 92, 93, 94]
R9	$O^- + O_2 \rightarrow O_3 + e$	$k_9 = 1.0 \times 10^{-12}\ cm^3/s$	[93, 94]

The gas composition can be obtained by solving a system of rate and mass conservation equations. In a time dependent model, the system reduces to a set of combined differential equations and algebraic equations. Based on the discussion given by Ref. [5], the minimal system of rate and mass conservation equations is given by

$$\frac{d[CO_2]}{dt} = -k_1 N_e [CO_2] + k_4 [O^-][CO] \tag{67}$$

$$\frac{d[O_3]}{dt} = \left(k_6[CO_2]_0[O] + k_9[O^-]\right)[O_2] - \left(k_3 N_e + k_4[O]\right)[O_3] \quad (68)$$

$$\frac{d[O]}{dt} = \left(k_1[CO_2] + 2k_2[O_2]\right) N_e - \left(2k_5[O][CO_2]_0 + k_4[O_3] + k_6[O_2][CO_2]_0 + k_8[O^-]\right)[O] \quad (69)$$

$$\frac{d[O^-]}{dt} = k_3 N_e[O_3] - \left(k_7[CO] + k_8[O] + k_9[O_2]\right)[O^-] \quad (70)$$

$$[CO_2]_0 = [CO_2] + [CO] \quad (71)$$

$$2[CO_2]_0 = 2[CO_2] + [CO] + [O] + 2[O_2] + 3[O_3] \quad (72)$$

where [X] is the concentration of species X, $[CO_2]_0$ is the initial concentration of neutral CO_2, k_n is the rate coefficient for n^{th} reaction, and N_e is the electron density calculated from (65). Equations (71) and (72) represent the mass conservation of carbon and oxygen atoms in the plasma, respectively. In Eq, (71), we have neglected the carbonic ions since they have negligible number densities in comparison with their neutral counterparts. Similarly, in Eq. (72) we have neglected the oxygen ions.

The steady state solution for this system can be found by setting the time differentials in Eqs. (67) to (70) equal to zero. This set, including eqs. (71) and (72), of nonlinear coupled equations can be solved for the six unknown concentrations: [CO], $[CO_2]$, [O], $[O_2]$, $[O_3]$, and $[O^-]$. Fig. 70 shows the resultss of the dissociation of CO_2 into CO, O, and O_2 under these steady state conditions. We observe from the figure that as the reduced electric field increases to 8.0×10^{-16} V cm^2 over 80% of the CO_2 has been dissociated.

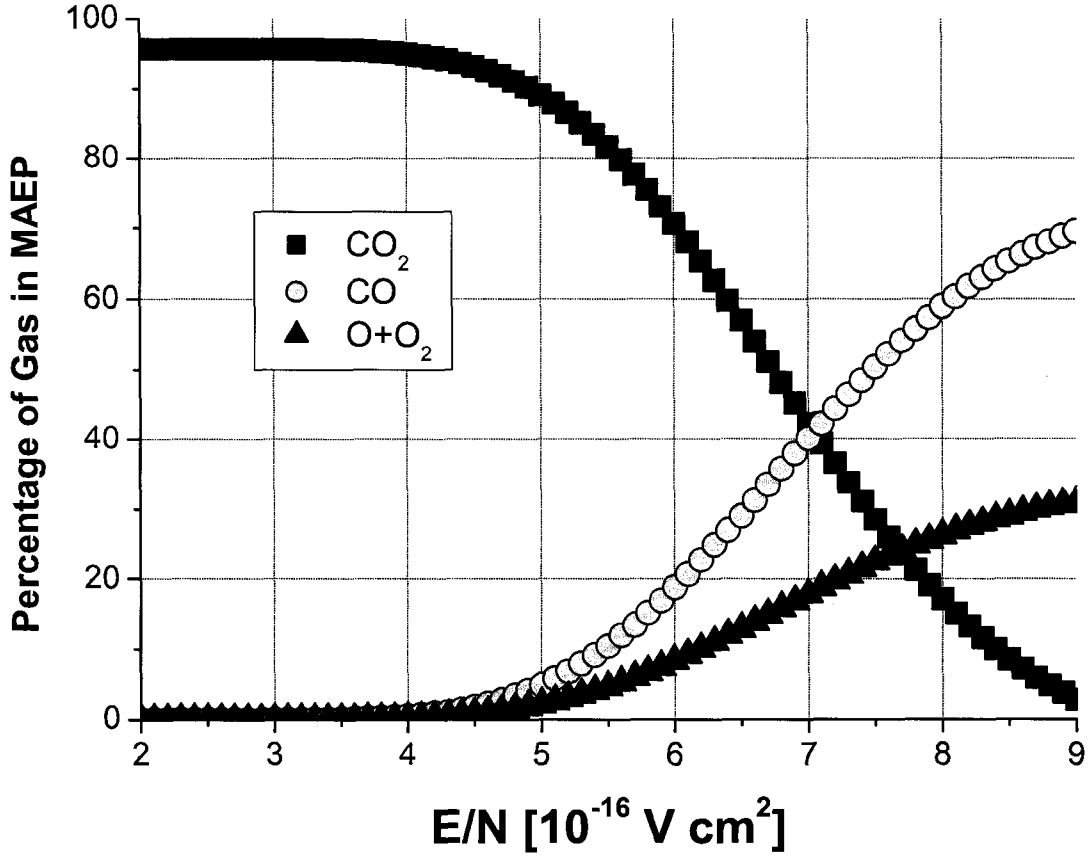

FIG. 70: Dissociation of CO_2 in the Martian atmosphere as a function of the reduced electric field from the Pathfinder Lander data assuming steady state conditions.

This calculation was performed assuming that the plasma in front of each of the probes was in thermal equilibrium. As mentioned previously, we are uncertain whether this assumption is correct. Thus, we determined the change in concentration of the system assuming non-equilibrium as well and present the results in Fig. 71. From the figure it is evident, that although the values for thermal equilibrium are higher, there is very little change in the over all concentration of CO_2. Similar results were observed for CO, O, and O_2.

Next we needed to estimate the reduced electric field (E/N) for the plasma. From Fig. 60 we observed that for the Pathfinder data from 10 km - 100 km the total change in jump temperature was approximately 36000 K or 3 eV. We estimate that the total thickness of the shock front is about 5λ, where λ is the mean free path, or about 0.3 cm. Thus the total electric field, E, is approximately 10 V/cm. We determined that the number density, N, was between 2×10^{16} and 1×10^{17} cm^{-3}. Therefore, we estimated the reduced electric field to be in the range of 1×10^{-16} to 6×10^{-16} V cm^2.

To calculate the time evolution of the species concentrations, we employed a forth order Runge-Kutta method. This method finds a solution over an interval h by combining information from several Euler-style steps and then uses this information to match a Taylor series expansion up to $O(h^4)$. Using fixed dissociation rate coefficients, we made these calculations and present these results in Fig. 72. We observe that about 95% of the CO_2 dissociation was achieved within 5.0×10^{-7} s. This result is consistent with previous work by Ref. [73], which showed the dissociation rate for CO_2 is very quick behind the shock front during Martian atmospheric entry.

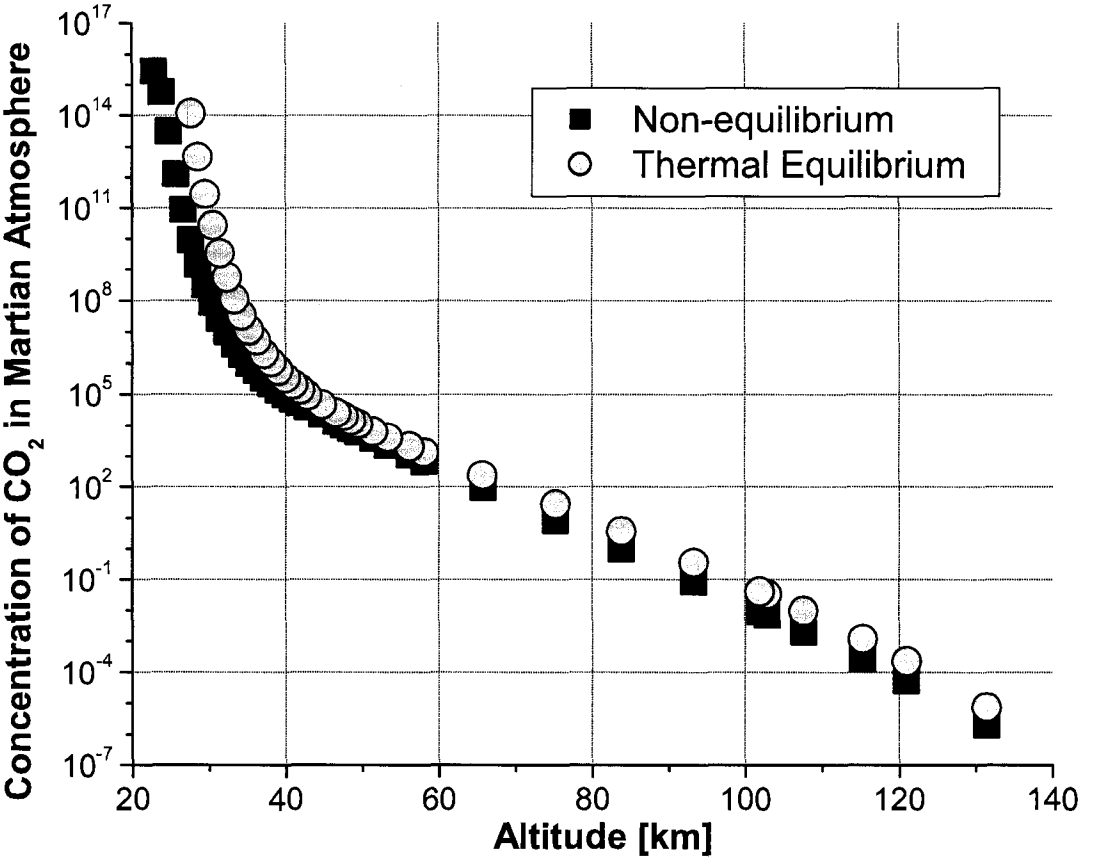

FIG. 71: Concentration of CO_2 as a function of the altitude in the Martian atmosphere determined by assuming thermal and non-equilibrium.

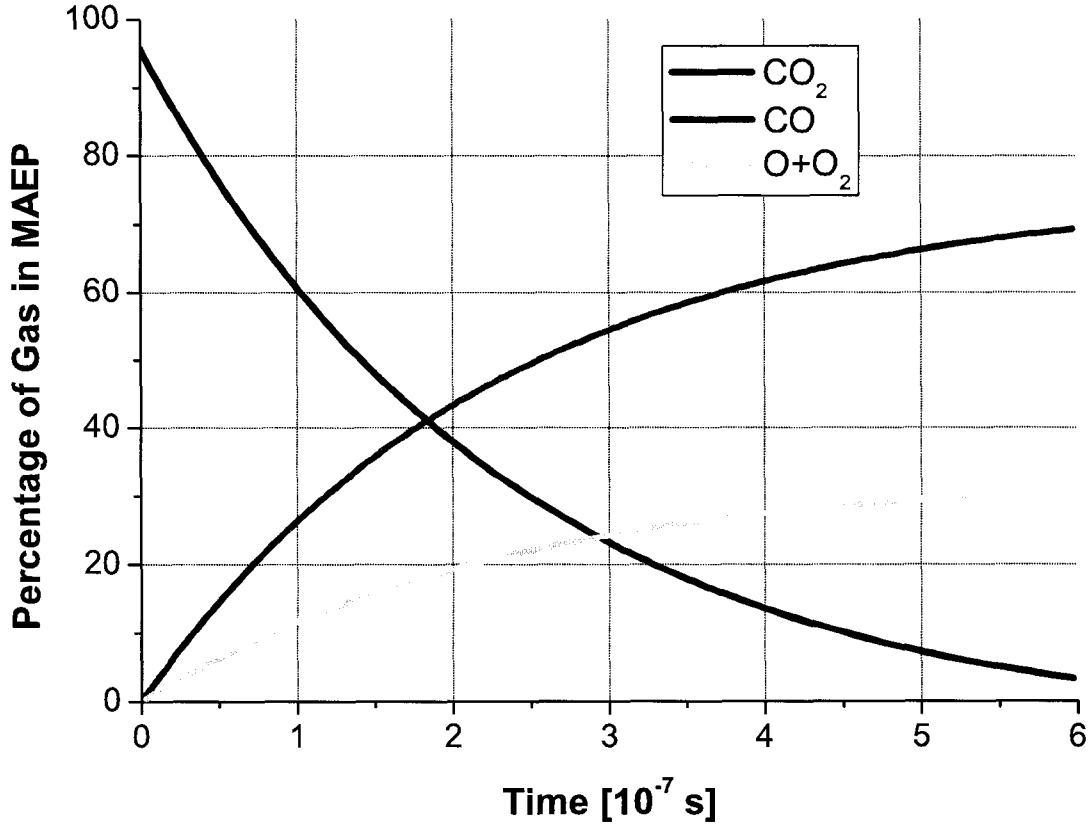

FIG. 72: Dissociation of CO_2 as a function of the time in the Martian atmosphere from the Pathfinder Lander data at $E/N = 5.0 \times 10^{-16}$ V cm ^{2}.

From the previous figures, we have observed that the composition of the MAEP will vary both with altitudes and over time. Thus, we looked at how this change in concentration of the species will effect the EEDF. From Fig. 73, we observe that the EEDF will change significantly as CO_2 is dissociated in the atmosphere. Therefore, we can conclude that changes in the composition will affect the values of the rate coefficients and concentration of CO_2 over time.

To calculate the changes in the composition, we started with the initial mixture and calculated the EEDF and rate coefficients for that mixture. After a specific length of time, a new composition was computed and the corresponding EEDF and rate coefficients were calculated. This process was repeated until most of the CO_2 in the MAEP was dissociated. We used time steps of 0.25×10^{-7} s. The values for the dissociation rate coefficient for carbon dioxide are presented in Fig. 74. For constant k_{CO_2}, a straight line would appear across the figure. Instead of a straight line, we observe a decrease in k_{CO_2} values over time. This corresponds to a change in the dissociation rate of CO_2 over time, as seen in Fig. 75 where the solid line represents the values that were obtained for constant rate coefficients. Over the same time interval, the percentage of CO_2 dissociation was 15% less with the effects of compositional changes included.

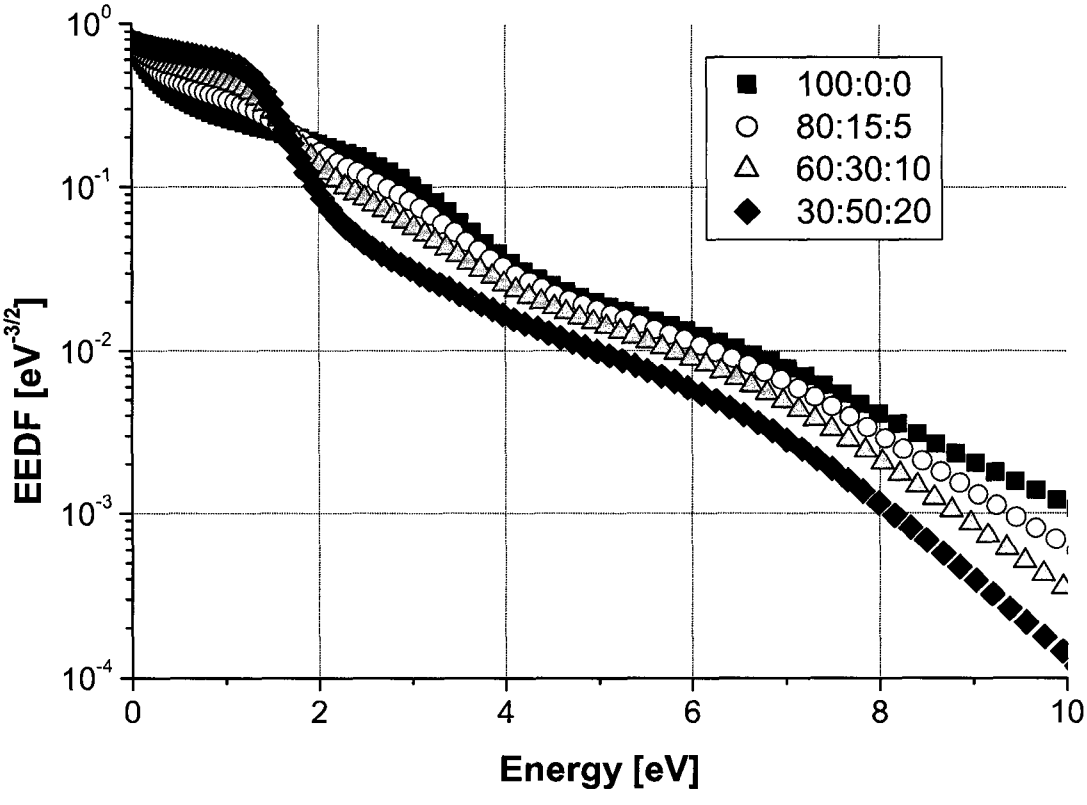

FIG. 73: EEDF as a function of the energy of different compositions of CO_2:CO:O_2 in MAEP.

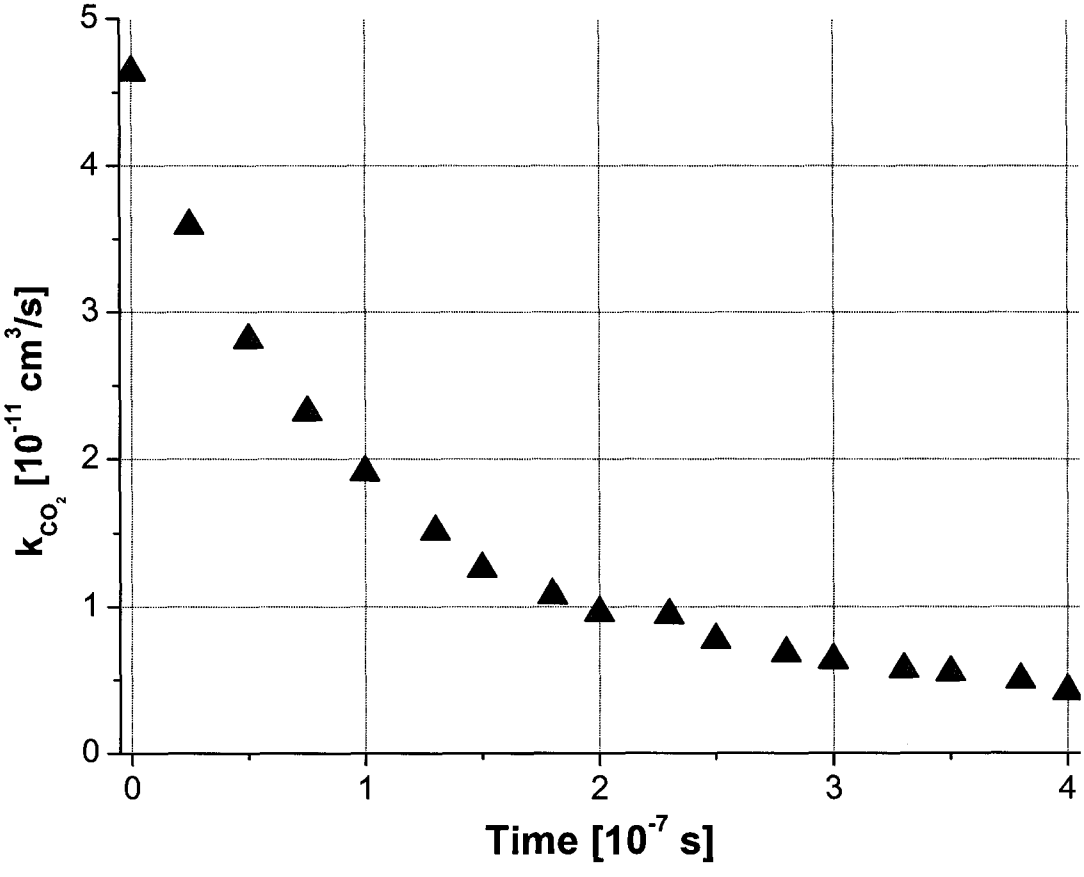

FIG. 74: Calculated dissociation rate coefficients for CO_2 as a function of time at an E/N =5.0 $\times$ 10^{-16} V cm^2 and an altitude of 40 km.

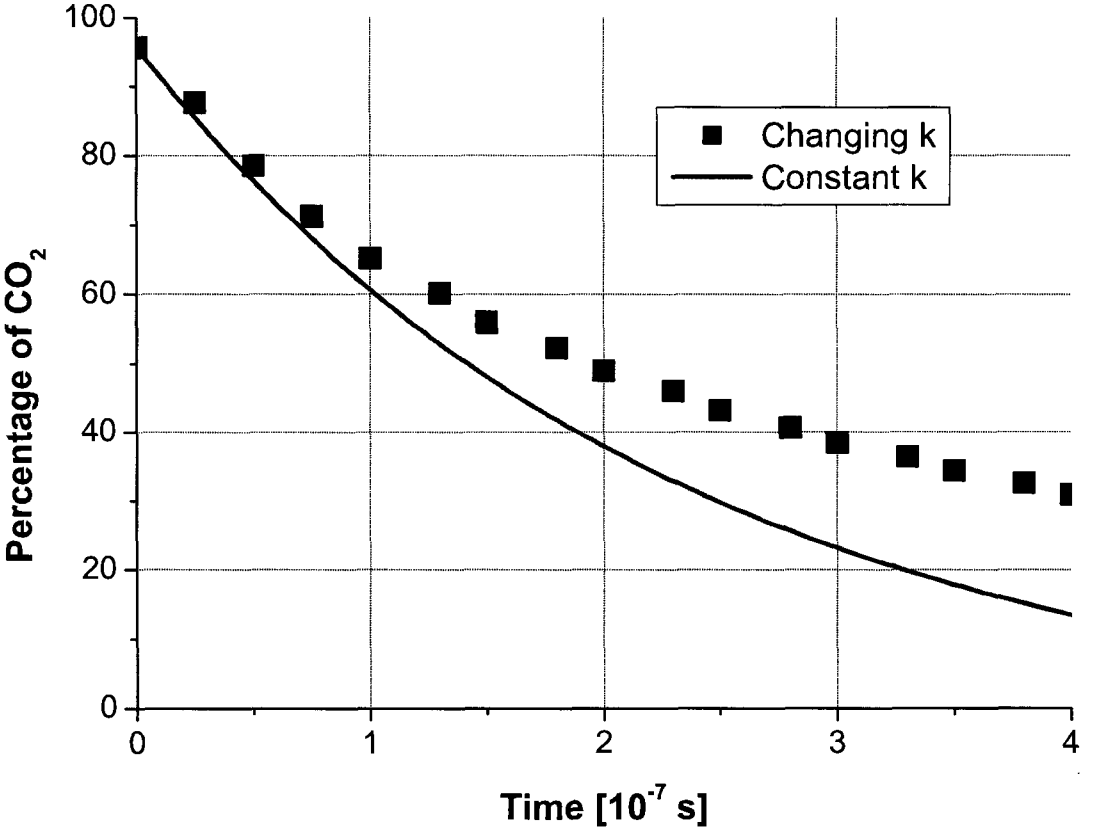

FIG. 75: Percentage of CO_2 in MAEP as a function of time at an E/N =5.0 $\times$ 10^{-16} V cm^2 and an altitude of 40 km.

IV.3.2 Influence of OH radicals

A water free model was presented in the previous sections of the paper. However, in the Martian atmosphere there is a small amount of water vapor, 0.03% see Table 6, which must be taken into account in order to accurately understand the atmospheric entry conditions. The effects associated with water vapor in discharges and plasmas have been studied by many groups over the years. Ratliff and Harrison [95] showed that when up to 5% water vapor was added to a glow discharge that the concentrations of the primary species in the discharge will be effected by the dissociation of H_2O and ion molecule reactions. Lockwood, *et al.* [96] showed how water vapor will effect chemical vapor deposition of diamond-like carbon using a CH_4-H_2 discharge. They observed that by adding 1% water vapor to the feed gas increased most of the hydrocarbon ion currents by about 50%, which they deduced was due primarily to an increase in electron concentration in the discharge. However, these effects have not been studied either experimentally or by modeling for Martian atmospheric entry conditions.

TABLE 9: Major reactions due to OH radicals in Martian atmospheric entry plasma.

No.	Reaction	Rate Coefficient	Ref.
R10	$CO + OH \rightarrow CO_2 + H$	$k_{10} = 1.5 \times 10^{-13}$ cm^3/s	[88, 92, 94]
R11	$O + OH \rightarrow O_2 + H$	$k_{11} = 3.0 \times 10^{-11}$ cm^3/s	[88]
R12	$H_2O + e \rightarrow OH + H^-$	$k_{12} = 5.0 \times 10^{-9}$ cm^3/s	[92]

The effect of OH radicals from water vapor in the MAEP is summarized in Table 9. From the last reaction, we observe that the generation rate of OH radicals from the dissociation of water molecules is relatively fast. This indicates that with an electron density of 10^{10} cm^{-3}, the concentration of OH radicals is about 10% of the initial water concentration in the system [5]. The first reaction has a direct effect on the dissociation of CO_2 in the atmosphere. Since the amount of water vapor reduces the rate of dissociation, we must take the OH radicals into account in our model. Thus, we included an amount of water vapor equivalent to 0.03% of the total gas volume in our model or the amount of water vapor in the Martian atmosphere.

As before, we observed the changes in the concentration of CO_2 in the atmosphere due to dissociation and present these results in Fig. 76. We observe that the addition of 0.03% watervapor or less to the model did not have a significant effect on the

dissociation of CO_2. However, with water vapor concentrations about 0.03% we observed a slower rate of decrease of CO_2 in MAEP. It is important to note the data was calculated for the Pathfinder Lander, but similar results were seen for all other landers mentioned in this report.

Another interesting phenomena that occurs when water vapor is added to our model, is that the production of O_2 in the system increases. As calculated for the Pathfinder Lander, Fig. 77, we estimated the percentage of O_2 will increase by 20%. This is significant since one of the proposed ideas is to extract O_2 from MAEP for us on the planet surface by explorers. Up till now most the experiments and models on this problem have focused on discharges that do not have any water vapor in them. Our results therefore indicate that it is important to include water vapor when studying this issue.

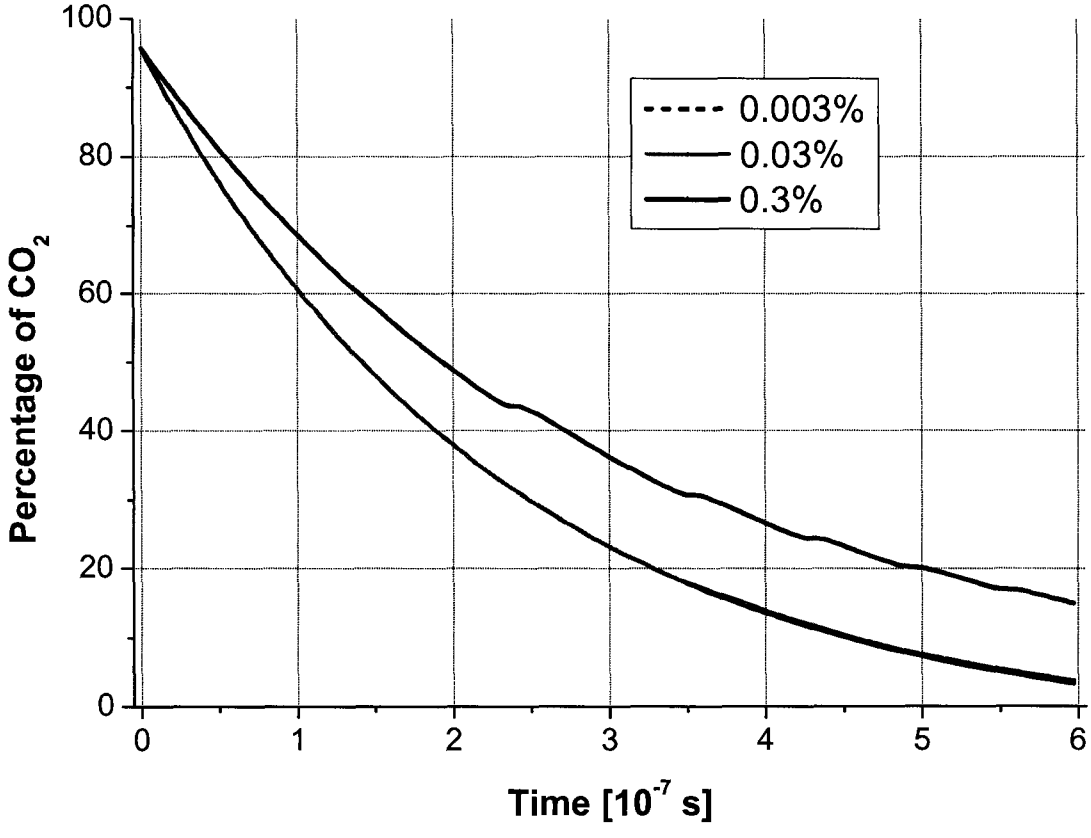

FIG. 76: Percentage of CO_2 in MAEP as a function of time with the addition of different amounts of water vapor added to the system. The 0.003% curve coincides with the 0.03% curve.

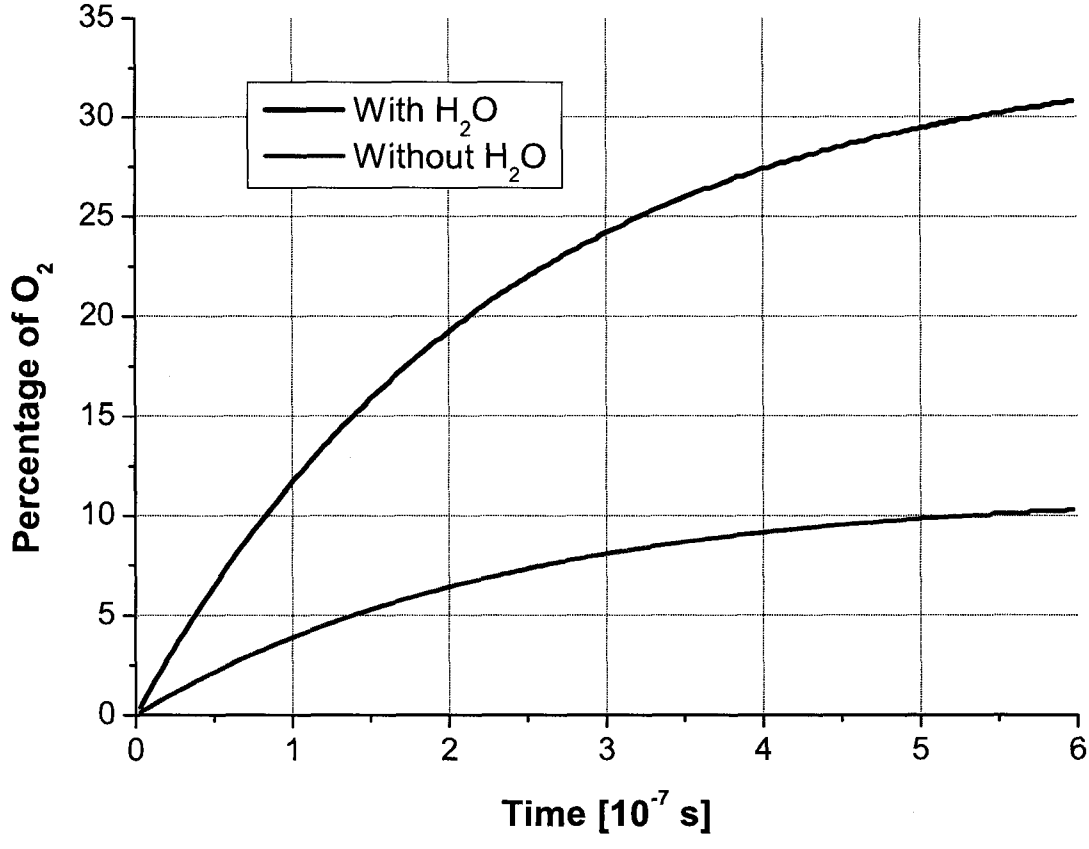

FIG. 77: Percentage of O_2 in MAEP as a function of time when 0.03% water vapor is added to the discharge model.

CHAPTER V

CONCLUSION

We have described a Mach 2 supersonic flowing microwave discharge used to investigate unresolved problems related to the interactions of a supersonic flow and a weakly ionized gas, plasma-assisted supersonic combustion, and the kinetics of Martian atmospheric entry plasma and its relationship to a potential application for harvesting during Martian entry. One of these unresolved problems associated with the interaction of a shock wave and a weakly ionized gas is the understanding of why there is an excessive increase in excited state populations at the shock fronts. This increase has been reported as being due to either a temperature gradient in the flow or the formation of a strong double electric layer at the shock front. Thus one key aim of the research was to look at the distribution of the populations of the excited states across the shock fronts. A concern for plasma-assisted supersonic combustion is the generation of excited species and radicals in the supersonic flow. A loss of ionization can cause a decrease in the production of these species. Therefore, understanding the effects of ionization loss in a discharge is important for combustion. The last set of problems we investigated were related to the kinetics of Martian atmospheric entry plasma. This type plasma is a complex mixture of ions, neutrals, and electrons and the kinetic modeling required in order to fully characterize it is very complex. Consequently, we needed to establish the basis for a kinetic model of Martian atmospheric entry plasma.

Plasma parameters were determined for a Mach 2 supersonic flowing microwave discharges in a mixture of Ar with up to 10% H_2 and up to 45% air and a Martian simulated mixture of 95.7% CO_2, 2.75% N_2, and 1.55% Ar. By using optical emission spectroscopy we analyzed the rotational spectrum of N_2 to find the rotational temperature of the Ar/H_2/Air discharge. We found that T_r decreased with increasing amounts of H_2 or air. From analysis of a pure air discharge, we determined that this decrease is due to the mixing of the different gas species. The T_r for the Martian simulated mixture was determined from analysis of the CO rotational spectrum. We found that the rotational temperature did not vary greatly with power density.

We investigated how the vibrational temperature varied in both mixtures. In the Ar/H_2/Air discharge, we determined T_v from analysis of the vibrational spectrum of the N_2 second positive system. As in the case of T_r, we found that T_v decreased with

increasing amounts of air due to mixing effects. For the Martian mixture, T_v was calculated from the ratio of the intensities of the vibrational levels 1 and 0 for the CO $B^1\Sigma^+$ state. We found that the vibrational temperature decreased with power density till it reached a plateau.

The electron excitation temperature and electron temperature were determined for the $Ar/H_2/Air$ discharge by analysis of the Ar I and Ar II spectra. We showed that the electron excitation temperature decreased with increasing power, but did not very greatly with the amount of H_2 in the discharge. The electron temperature for a pure Ar discharge was found to be relatively constant as the power density increased. We concluded that with increasing power the average energy of the electrons in the discharge do not vary significantly. In addition, we noticed that the electron temperature decreased when 5% H_2 was added to the discharge, which is an indication of ionization loss. Spherical models were then added to flow and the populations of the Ar I states were determined. We observed an excessive increase in excited state populations in front of the models. However, we did not observe a strong variation in the populations which are indicative of a strong double electric layer.

Part of the experiment was to determine the electron density through analysis of the hydrogen Balmer series and the nitrogen second positive system. Both approaches were used to analyze the discharge in $Ar/H_2/Air$. We observed that the electron density, as determined from the hydrogen Balmer lines, was constant as the power density increased. On the other hand, the electron density decreased with increasing amounts of H_2 in the system, which is a direct indicator of ionization loss in the discharge. When the electron density was calculated from the N_2 spectrum, the decrease was lower. In addition, we observe that the electron density increased with power density, while the data taken from the hydrogen lines were constant. This increase is expected, since with increasing energy in the system, the possibility of ionization of different atoms and molecules does increase. For the Martian simulated discharge, we observed that the electron density increased with power density but was nearly two orders of magnitude lower then the density for the $Ar/H_2/Air$ discharge. The presence of negative ions in the discharge could account for the observed difference.

A gas kinetic model was developed for an $Ar/H_2/Air$ discharge by finding an isotropic solution to the Boltzmann transport equation in order to determine the electron energy distribution functions. From these functions the average electron

energy and rate coefficients for different processes within the discharges were determined. The effects of the addition of H_2 and air to an Ar discharge were discussed. We showed that knowing the initial composition of the discharge was highly important for effective modeling of the changes in the composition. In addition, the effects of ionization loss when H_2 was added to the mixtures was discussed.

We then constructed a model of Martian atmospheric entry given data from the Pathfinder, Viking, and MER Opportunity Landers. The density, pressure, and temperature across the shock front were calculated for each probe. A distribution of temperature was observed due to the imprecision in the atmospheric models and data for the free stream temperature. The electron density was determined from the Saha-Boltzmann equation for a simple model with the main species of the ionized gas. Because of the distribution in the temperature across the shock front, a large distribution in electron density was observed at altitudes above 50 km for the Viking and MER Opportunity Landers. Comparison between the calculated values and the experimental results showed good agreement.

A gas kinetic model was then used to estimate the dissociation of CO_2 in the Martian atmosphere for steady state and non-steady state conditions. Under non-steady state conditions we observed a decrease of 20% in the rate of CO_2 dissociation in the MAEP. Water vapor in concentrations consistent with that in the Martian atmosphere were added to the model. The effect of the water vapor on the model was then calculated. With so small amount of water vapor we found an increase in the dissociation of CO_2 in the Martian air as well as an increase in the O_2 production.

In this research we confirmed that there is an accumulation of excited states at the shock fronts produced by a spherically blunt body and there was an observable decrease in ionization when hydrogen and air were added to a pure Ar discharge. We also established the kinetic basis for a detailed study of Martian atmospheric entry plasma. In addition, we discovered a plasmoid in the afterglow region of the flow which has not been well documented in the literature. Due to a lack of nonintrusive diagnostic techniques we developed and successfully tested a sensitive technique for measuring the electron density based on the intensity of the N_2 second positive system and a technique for evaluation of the electron temperature from a ratio of Ar atomic and Ar ionic lines. We have also worked extensively on the application of supersonic flowing microwave discharges to validate a Martian entry model. Furthermore, we developed a model MHD generator which demonstrated the feasibility of

harvesting plasma during Martian atmospheric entry. Additional research will entail a detailed study of the aerodynamic and electrodynamic properties of the plasmoid in the afterglow and measurements of the Ar metastable state using absorption spectroscopy. It is recommended that Rayleigh scattering be used to determine absolute gas temperatures for the discharge since emission spectroscopy can not provide direct measurement of this parameter. Finally, a more detailed study should be conducted on the physics behind the use of the N_2 second positive system to measure the electron density.

BIBLIOGRAPHY

[1] E. J. Lerner, Industrial Physicist **6**, 16 (2000).

[2] G. R. Brewer, M. R. Currier, and R. C. Knechtil, Proceedings of the IRE **49**, 1789 (1961).

[3] W. L. Wiese, M. W. Smith, and B. M. Miles, *Atomic Transtion Probabilities. Vol. 2: Sodium through Calcium*, (NSRDS-NBS, Washington, D. C., 1969).

[4] M. A. Liebermann and A. J. Lichtenberg, *Principles of Plasma Discharges and Marterials Processing.* Wiley: NY, 1994.

[5] T. Dinh, *Decomposition of Carbon Dioxide in a Capacitively Coupled Radio Frequency Discharge*, Ph.D. Thesis, Old Dominion University, Norfolk, VA, USA, 2002.

[6] G. Hartmann and P. C. Johnson, J. Phys. B: Atom. Molec. Phys. **11**, 1597 (1978).

[7] K. L. McNesby and R. A. Fifer, Appl. Spectro. **45**, 61 (1991).

[8] A. Bogaerts and R. Gijbels, Spectro. Acta. B **57**, 1971 (2002).

[9] Y. Z. Ionikh, N. V. Chernysheva, A. V. Meshchanov, A. P. Yalin, and R. B. Miles, Phys. Lett. A **259**, 387 (1999).

[10] A. F. Aleksandrov, N. G. Vidyakin, V. A. Lakutin, M. G. Skvortsov, I. B. Timofeev, and V. A. Chernikov, Sov. Phys. Tech. Phys. **31**, 468 (1986).

[11] P. Bletzinger, B. N. Ganguly, D. Van Wie, and A. Garscadden, J. Phys. D: Appl. Phys. **38**, R33 (2005).

[12] P. Bletzinger and B. N. Ganguly, Phys. Lett. A **258**, 342 (1999).

[13] S. Popović and L. Vušković, Phys. Plasmas **6**, 1448 (1999).

[14] P. Bletzinger, B. N. Ganguly, and A. Garscadden, Phys. Plasmas **7**, 4341 (2000).

[15] S. O. Macheret, Y. Z. Ionikh, N. V. Chernysheva, A. P. Yalin, L. Martinelli, and R. B. Miles, Phys. Fluids **13**, 2693 (2001).

[16] N. Siefert, B. N. Ganguly, P. Bletzinger, Phys. Rev. E **72**, 066402(6) (2005).

[17] C. J. Jachimowski, NASA Report No. TP-2791, 1988.

[18] D. J. Drake, S. Popović, and L. Vušković, J. Appl. Phys. **104**, 063305 (2008).

[19] M. Berglund, N. Wilkström, and C. Fureby, FOI-R-1650-SE (2005).

[20] S. M. Starikovskaia, J. Phys. D: Appl. Phys. **39**, R265 (2006).

[21] S. B. Leonov and D. A. Yarantsev, Plasma Sources Sci. Technol. **16**, 132 (2007).

[22] E. Barbi, J. R. Mahan, W. E. O'Brien, and T. C. Wagner, J. Propul. Power **5**, 129 (1989).

[23] M. Capitelli and M. Dilonardo, Chem. Phys. **24**, 417 (1977).

[24] R. S. Mason, P. D. Miller, and I. P. Mortimer, Phys. Rev. E **55**, 7462 (1997).

[25] R. Hermann, UARI Research Report No. 29 (1965).

[26] M. Lino da Silva, F. Passarinho, and M. Dudeck, J. Thermophys. Heat Trans. **20**, 680 (2006).

[27] V. A. Gorelov, M. K. Gladyshev, A. Yu. Kireev, and S. V. Shilenkov, J. Appl. Mech. Tech. Phys. **41**, 970 (2003).

[28] P. Kessaratikoon, *Shock Wave Dispersion in Weakly Ionized Gas*, Ph.D. Thesis, Old Dominion University, Norfolk, VA, USA, 2003.

[29] J. Jackson, *Classical Electrodynamics.* 3rd Ed. Wiley: NY, 1999.

[30] W. H. Hayt, *Engineering Electromagnetics.* McGraw-Hill: NY, 1989.

[31] D. B. Atkinson and M. A. Smith, Rev. Sci. Instrum. **66 (9)**, 4434 (1995).

[32] J. D. Anderson, *Modern Compressible Flow with Historical Perspective.* 3rd Ed. McGraw-Hill: NY, 2004.

[33] J. J. Bertin, *Aerodynamics for Engineers.* 4th Ed. Prentice-Hall: Upper Saddle River, NJ, 2002.

[34] M. Rasmussen, *Hypersonic Flow.* Wiley: NY, 1994.

[35] Ya. B. Zel'dovich and Yu. P. Raizer, *Physics of Shock Waves and High-Temperature Hydrodynamic Phenomena.* Dover: Mineola, NY, 2002.

[36] B. L. Sands, N. S. Siefert, and B. N. Ganguly, Plasma Sources Sci. Tech. **16**, 716 (2007).

[37] L. Vušković, S. Popović, D. J. Drake, and R. Moses, *Magnetohydrodynamic Power Generation in the Laboratory Simulated Martian Entry Plasma.* Fifteenth International Conference on MHD Energy Conversion, Moscow, Russia, May 2005.

[38] J. M. Williamson, P. Bletzinger, and B. N. Ganguly, J. Phys. D: Appl. Phys. **37**, 1658 (2004).

[39] R. D. Cowan and G. H. Dieke, Rev. Mod. Phys. **20**, 418 (1948).

[40] G. Herzberg, *Molecular Spectra and Molecular Structure: Spectra of Diatomic Molecules*, D. Van Nordstom: NY, 1950.

[41] V. N. Ochkin, S. Yu. Savinov, and N. N. Sobolev, Trudy FIAN **157**, 6 (1985).

[42] P. H. Krupenie, *The Band Spectrum of Carbon Monoxide*, (NSRDS-NBS-5, Washington, D. C., 1966).

[43] H. Hönl and F. London, Z. Physik **33**, 803 (1925).

[44] O. A. Evsin, E. B. Kupriyanova, V. N. Ochkin, S. Yu. Savinov, and S. N. Tskhai, Bulletin of the Lebedev Phys. Inst. **10**, 9 (1994).

[45] A. Qayyum, Z. Shaista, M. A. Naveed, N. U. Rehman, S. A. Ghauri, and M. Zakaullah, J. Quant. Spec. Rad. Trans. **107**, 361 (2007).

[46] M. Ivković, S. Jovićević, and N. Konjević, Spectro. Acta B **59**, 591 (2004).

[47] R. F. G. Meulenbroeks, A. J. van Beek, A. J. G. van Helvoort, M. C. M. van de Sanden, and D. C. Schram, Phys. Rev. E **49**, 4397 (1994).

[48] L. Vušković and S. Popović, *Magnetohydrodynamic Power Generator.* Report to NASA LARC April 2005.

[49] J. Loureiro and C. M. Ferreira, J. Phys. D: Appl. Phys. **22**, 67 (1989).

[50] J. T. Gudmundsson, I. G. Kouznetsov, K. K. Patel, and M. A. Lieberman, J. Phys. D: Appl. Phys. **34**, 1100 (2001).

[51] A. Rodero, M. C. Garcia, M. C. Quintero, A. Sola, and A. Gamero, J. Phys. D: Appl. Phys. **29**, 681 (1996).

[52] A. D. MacDonald, *Microwave Breakdown in Gases.* John Wiley & Sons: NY, 1966.

[53] X. Tu, B. G Chéron, J. H. Yan, L. Yu, and K. F. Cen, Phys. Plasmas **15**, 053504 (2008).

[54] C. V. Budtz-Jørgensen, P. Kringhøj, and J. Bøttiger, Surf. Coat. Technol. **116-119**, 938 (1999).

[55] N. Hershkowitz, Space Sci. Rev. **41**, 351 (1985).

[56] L. S. Frost and A. V. Phelps, Phys. Rev. **127**, 1621 (1962).

[57] J. Lowke, A. V. Phelps, and B. W. Irwin, J. Appl. Phys. **44**, 4664 (1973).

[58] L. C. Pitchford, S. V. O'Neil, and J. R. Rumble Jr., Phys. Rev. A **23**, 294 (1980).

[59] V. Puech and L. Torchin, J. Phys. D **19**, 2309 (1986).

[60] S. J. Buckman and A. V. Phelps, J. Chem. Phys. **82**, 4999 (1985).

[61] A. V. Phelps and L. C. Pitchford, Phys. Rev. **31**, 2932 (1985).

[62] S. A. Lawton and A. V. Phelps, J. Chem. Phys. **69**, 1055 (1978).

[63] C. M. Ferreria and J. Loureiro, J. Phys D: Appl. Phys **16**, 2471 (1983).

[64] G. M. Petrov and D. Zhechev, Phys. Plasmas **9**, 1815 (2002).

[65] H. Singh and D. B. Graves, J. Appl. Phys. **87**, 4098 (2000).

[66] R. D. Hake Jr. and A. V. Phelps, Phys. Rev. **158**, 70 (1967).

[67] D. J. Drake, S. Popović, L. Vušković, and T. Dinh, submitted to IEEE Trans. Plasma Sci. (2009).

[68] D. F. Doody, Acta Astronaut. **35**, 475 (1995).

[69] S. Bougher, G. Keating, R. Zurek, J. Murphy, R. Haberle, J. Hollingsworth, and R. T. Clancy, Adv. Space Res. **23**, 1887 (1999).

[70] R. D. Braun and R. M. Manning, IEEEAC paper 0076 (2006).

[71] D. A. Spencer and R. D. Braun, J. Spacecraft and Rockets **33**, 670 (1996).

[72] P. A. Gnoffo, Annu. Rev. Fluid Mech. **31**, 459 (1999).

[73] C. Park, J. T. Howe, R. L. Jaffe, and G. V. Candler, J. Thermophys. Heat Trans. **8**, 9 (1994).

[74] V. Lago, A. Lebhot, M. Dudeck, S. Pellerin, T. Renault, and P. Echegut, J. Thermophys. Heat Trans. **15**, 168 (2001).

[75] E. Barbosa, B. Lopez, M. Dudeck, A. Kaminska, and B. Izrar, *Numerical Simulations of Non-equilibrium Hypersonic Flow in a Convergent-divergent Nozzle: Applications to Mars Atmospheric Entry Simulation*, Proc. VII International Symposium on Exp. and Comp. Aerothermodynamics of Internal Flows, Lyon, France, July 2007.

[76] R. G. Prinn and B. Fegley, Ann. Rev. Earth Planet. Sci. **15**, 171 (1987).

[77] A. O. Nier and M. B. McElroy, J. Geophys. Res **82**, 4341 (1977).

[78] A. O. Nier, W.B. Hanson, M. B. McElroy, A. Alvin, and N. W. Spencer, Icarus **16**, 74 (1972).

[79] J. T. Schofield, J. R. Barnes, D. Crisp, R. M. Haberle, S. Larsen, J. A. Magalhaes, J. R. Murphy, A. Seiff, and G. Wilson, Science **278**, 1752 (1997).

[80] G. M. Keating, S.W. Bougher, R. W. Zurek, R. H. Tolson, G. J. Cancro, S. N. Noll, J. S. Parker, T. J. Schellenberg, R. W. Shane, B. L. Wilkerson, J. R. Murphy, J. L. Hollingsworth, R. M. Haberle, M. Joshi, J. C. Pearl, B. J. Conrath, M. D. Smith, R. T. Clancy, R. C. Blanchard, R. G. Wilmoth, D. F. Rault, T. Z. Martin, D. T. Lyons, P. B. Esposito, M. D. Johnston, C. W. Whetzel, C. G. Justus, and J. M. Babicke, Science **279**, 1998 (1998).

[81] K. T. Edquist, D. S. Liechty, B. R. Hollis, S. J. Alter, and M. P. Loomis, J. Spacecraft and Rockets **43**, 330 (2006).

[82] L. Vušković and S. Popović, *Magnetohydrodynamic Power Generator.* Report to NASA LaRC March 2004.

[83] J. W. Bond Jr., Jet Propul. **28**, 228 (1958).

[84] S. R. Byron and H. Apter, J. Appl. Phys. **71**, 1976 (1992).

[85] P. H. Wine, J. M. Nicovich, R. J. Thompson, and A. R. Ravishankara, J. Phys. Chem. **87**, 3948 (1983).

[86] R. Atkinson, D. L. Baulch, R. A. Cox, R. F. Hampson Jr., J. A. Kerr, M. J. Rossi, and J. Troe, J. Phys. Chem. Ref. Data **26**, 1329 (1997).

[87] J. E. Morgan and H. I. Schiff, J. Chem. Phys. **38**, 1495 (1963).

[88] P. W. Pace and M. Lacombe, IEEE J. Quantum Electron. **14**, 263 (1978).

[89] H. Shields, A. L. S. Smith, and B. Norris, J. Phys. D: Appl. Phys. **9**, 1587 (1976).

[90] I. C. Walker, J. M. Gingell, N. J. Mason, and G. Marston, J. Phys. B: At. Mol. Opt. Phys. **29**, 4749 (1996).

[91] D. A. Parkes, J. Chem. Soc. Faraday Trans. **68**, 627 (1972).

[92] C. Leys, C. V. Egmond, and E. Desoppere, J. Appl. Phys. **78**, 2265 (1995).

[93] W. L. Nighan and W. J. Wiegand, Phys. Rev. A. **10**, 922 (1974).

[94] H. Hokazono and H. Fujimoto, J. Appl. Phys. **62**, 1585 (1987).

[95] P. H. Ratliff and W. W. Harrison, Spectro. Acta. B **49**, 1747 (1994).

[96] R. B. Lockwood, R. E. Miers, L. W. Anderson, J. E. Lawler, and C. C. Lin, Appl. Phys. Lett. **55**(14), 1385 (1989).

[97] S. P. Kuo and D. Bivolaru, Phys. Plasmas **8**, 3258 (2001).

[98] V. R. Soloviev, V. M. Krivtsov, A. M. Konchakov, and N. D. Malmuth, AIAA J. **41**, 2403 (2003).

[99] M. Rajabian, D. V. Gravelle, and S. Vacquié, Plasma Chem. Plasma Process. **24**, 285 (2004).

[100] Y. Arata, A. Kobayashi, and Y. Habara, J. Appl. Phys. **62**, 4884 (1987).

[101] Z. Sheng, X. Binshi, and J. K. Yao, Mater. Sci. Forum **475-478**, 3981 (2005).

[102] D. Harbec, J. L. Maunier, L. Guo, and J. Jureidini, Carbon **45**, 2054 (2007).

[103] S. I. Choi, J. S. Nam, J. I. Kim, T. H. Hwang, J. H. Seo, and S. H. Hong, Thin Solid Films **506-507**, 244 (2006).

[104] K. H. Lee, H. Jang, G. Eom, B. Lee, D. Burk, L. Overzet, and G. S. Lee, Mater. Lett. **62**, 3849 (2008).

[105] R. J. Rosa, *Magnetohydrodynamic Energy Conversion.* McGraw-Hill: NY, 1968.

[106] V. A. Kirillin and A. E. Sheyndlin, *MHD Energy Conversion: Physiotechnical Problems.* AIAA: NY, 1983.

APPENDIX A

MAGNETOHYDRODYNAMIC ENERGY CONVERSION

A.1 INTRODUCTION

In addition to plasma-assisted supersonic combustion and atmospheric entry modeling, supersonic flowing discharges and plasmas have been used for many applications, including supersonic drag reduction, inlet shock control, generation of ceramic coatings, and carbon nanotube production.

One of the main issues associated with supersonic flight is vehicle drag. Drag is the force of a fluid on an object that resists the motion of that object as it passes through the fluid. The drag force due to the flow of air around a supersonic vehicle can be substantial and is directly related to the Mach number of the flow. The Mach number is defined as the ratio of the speed of the vehicle to the speed of sound in air. To reduce the drag force, a small amount of plasma is generated close to the surface of a hypersonic vehicle [97, 98]. The plasma causes a rise in gas temperature around the vehicle and thus a reduction in pressure close to the surface. The air flow is then altered over the vehicle surface due to this pressure change, which reduces the drag on the vehicle.

Another issue for supersonic vehicles is the design of the inlet for air flow into an engine. The inlet is designed to have one Mach number at a specific angle of attack, where the angle of attack for a vehicle is defined as the angle between the vehicle's body and the direction of the air flow. Plasma inlet shock control can be used when situations require variable inlet characteristics, such as a hypersonic craft which must fly at various Mach numbers [11]. A discharge is produced on the forebody of the inlet thus ionizing the air and reducing the pressure and flow rate into the inlet. Consequently, the Mach number of the air flow is reduced.

Supersonic plasma jets have been shown to help in the production of high quality ceramic coating. Since these jets are able to work at high temperatures, there is the possibility of using both metals and nonmetals with very high melting points for ceramic coatings [99, 100]. In an article by Sheng [101], the use of a hypersonic plasma sprayer was described. The sprayer was able to produce ceramic coatings with improvements in both performance and microstructure. In addition, the cost to produce the same quality as the supersonic plasma jets was decreased by half with

the hypersonic sprayer.

Supersonic plasma jets have also been shown by a number of researcher groups to create high purity carbon nanotubes [102, 103]. Carbon nanotubes are cylindrical lattices of carbon atoms bonded together in various ways: zigzag, chiral, armchair, etc. Carbon nanotubes have been studied in both industry and academy for their possible application to nano-electronics, contact electrodes, and sensors. This means that there is a need to create good, high quality tubes in large volumes [104], which plasmas have been shown to do.

In addition to these many applications of supersonic discharges, there is the possibility of harvesting Martian plasma for use on the surface. During the entry phase into the Martian atmosphere, which lasts about 120 s, most of the kinetic energy of a probe is lost in the form of heat and thermal ionization. The motivation behind this part of my work is to extract usable power, employing a magnetohydrodynamic generator (MHD), from the plasma that is produced in the entry phase.

A.2 MAGNETOHYDRODYNAMIC GENERATORS

Magnetohydrodynamic generators have been seen as an approach to generate power since 1910 when the study of the electrical properties of gases began to develope [105]. Using these properties and Faraday's law of electromagnetic induction, a MHD model can be created. The basic physics of this device is that it converts the thermal energy in a hot flowing gas stream into electrical energy by means of an electromagnetic field [106].

In Fig. 1 we presented a diagram of the experimental apparatus. Once the flow has been accelerated and ionized in the microwave cavity, we add a MHD generator model in place of the spherical blunt body downstream of the cavity. This flowing afterglow provides the necessary ionization and conductivity to operate the MHD generator.

A model was constructed from aluminum silicate with large cooper electrodes attached to either side by high temperature epoxy. Two small magnetic discs, made of $SmCo_5$, where placed inside the model with approximately a 0.4 cm separation between the magnets, see Fig. 78. $SmCo_5$ is a sintered rare earth magnetic material with high maximum energy density and rather high Curie temperature and residual magnetic flux density, which makes it useful in our experiments [82]. In Table 10 we present the characteristics of the $SmCo_5$ and $SmCo_{16}$.

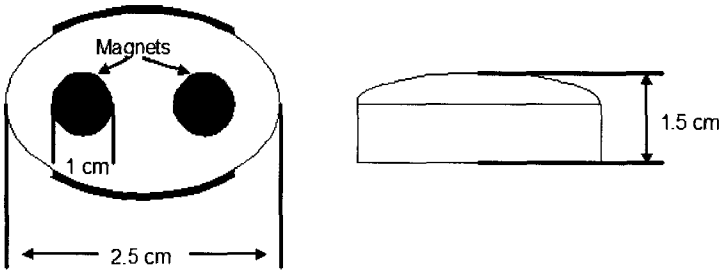

FIG. 78: Schematic of the MHD generator model.

TABLE 10: Characteristics of $SmCo_5$ and $SmCo_{16}$.

Residual magnetic flux density	$B_r = 0.82$T
Coercive force	$H_{cb} = 597$ kA/m
Intrinsic coercive force	$H_{cj} \geq 1989$ kA/m
Maximum energy product	BH $= 127$ kJ/m^3
Curie temperature	$T_C = 685$ °C
Thermal expansion coefficent (perpendicular)	$\alpha_\perp = 1.3 \times 10^{-5}$ 1/°C
Thermal expansion coefficient (parallel)	$\alpha_\parallel = 0.7 \times 10^{-5}$ 1/°C
Density	$\rho = 8.4\ g/cm^3$
Electrical conductivity	$\sigma = 1.92 \times 10^4\ 1/\Omega cm$

The magnetic field of the MHD model was measured in the axial and radial directions at room temperature using a Gaussmeter. These results are shown in Fig. 79. A peak magnetic field strength was found to be at B = 0.22 T with a magnetic field larger then 0.1 T, extending over a volume of more than 2.0 cm^3. By varying the environmental temperature, we found that magnetic field strength of the $SmCo_5$ magnet was constant up to about 450 K, as shown in Fig. 80. Then over the next 200 K, it decreased by nearly 35%, which can play an important role in the effectiveness of the MHD model.

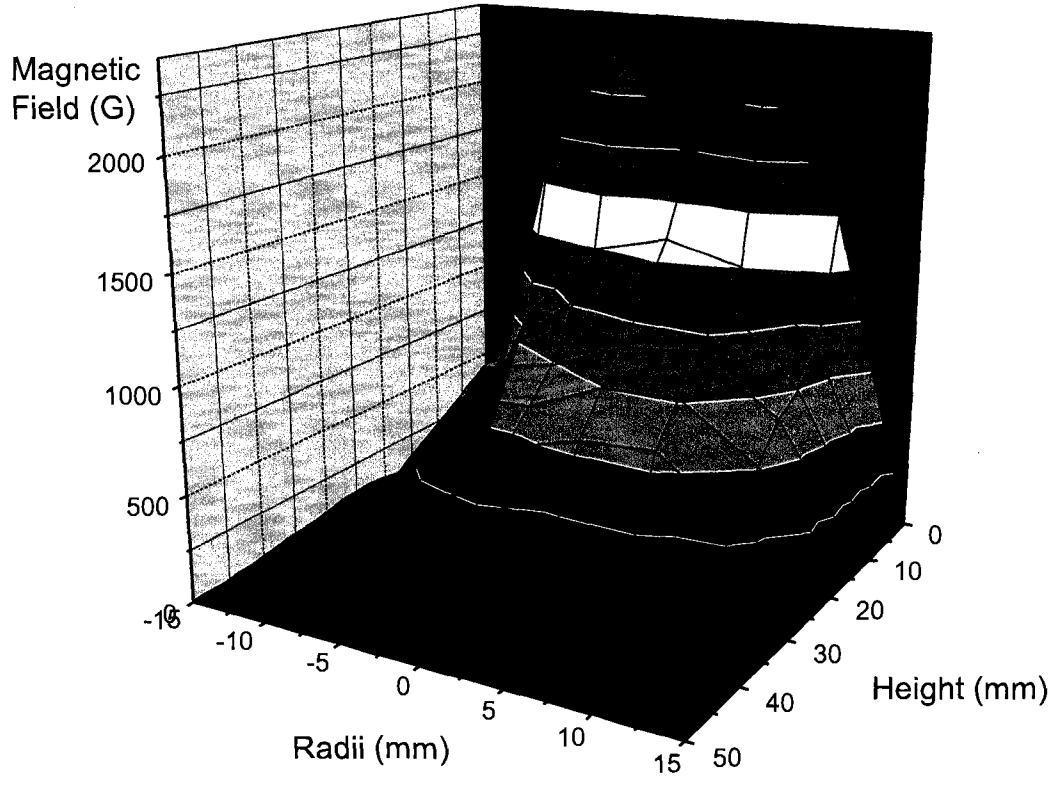

FIG. 79: Magnetic field strength distribution for the MHD model with $SmCo_5$ magnets.

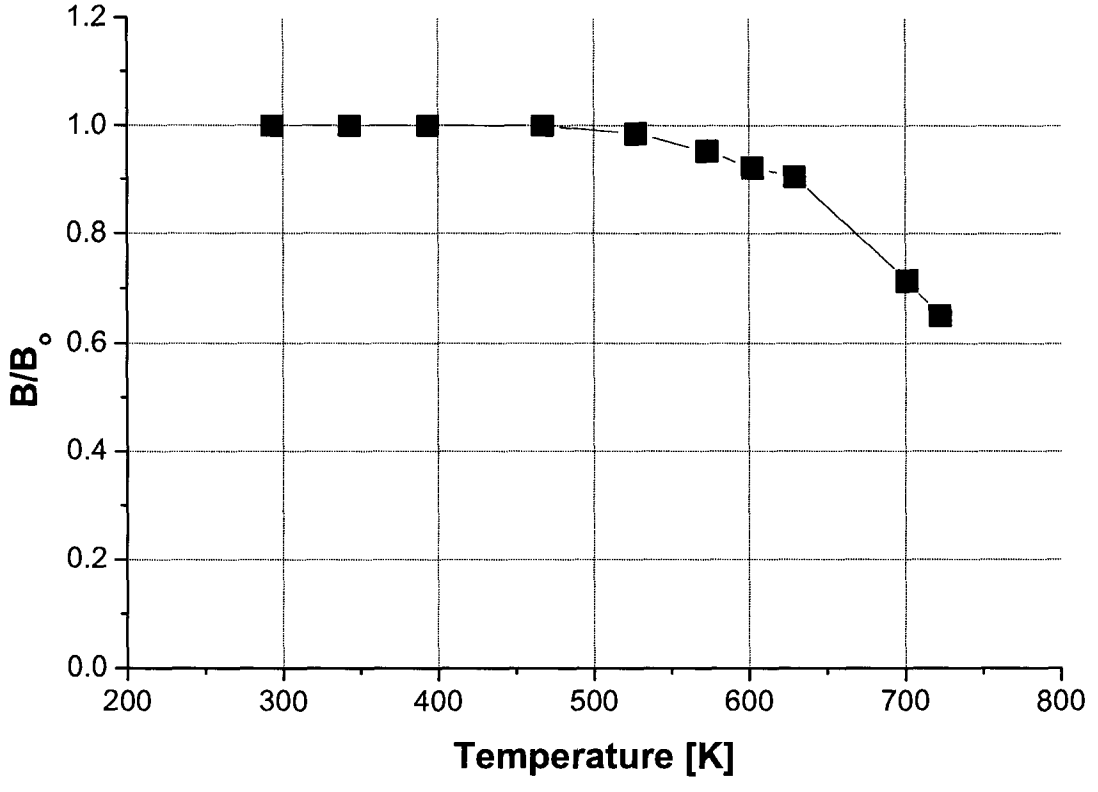

FIG. 80: Ratio of the magnetic field (B) to the inital magnetic field (B_0) as a function of the temperature.

A.3 EXPERIMENTAL RESULTS

The goal of our work with the MHD generator is to extract part of the lost energy with about 1% efficiency, which would result in 40 kWh of energy being extacted duing the entry phase. Martian atmospheric entry plasma has a very high degree of ionization, which means that the efficiency of an MHD maybe far more then 1% [37]. In order to study this, we have attached our MHD generator in series to a light emitting diode (LED) and 5 kΩ resistor, as shown in Fig. 81.

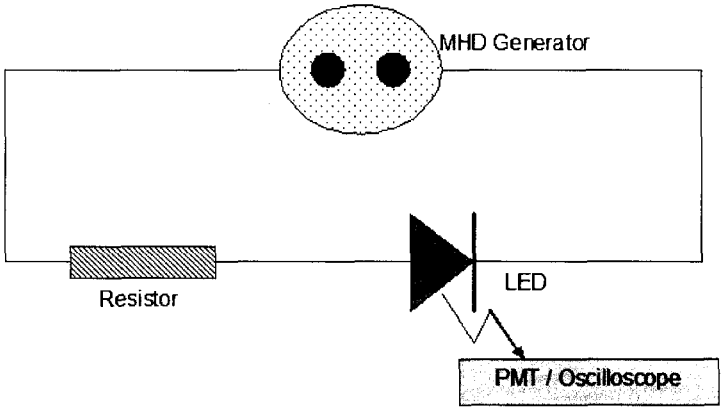

FIG. 81: Scheme of current collection from MHD generator.

In front of the LED was placed a photomultiplier tube (PMT). The PMT was attached to a Tektonix Model TDS 340A oscilloscope to measure the amount of photons emitted by our LED. In order to determine accurately the current produced by our MHD generator, the PMT was calibrated using a variety of resistors to construct a plot of the voltage vs. current as shown in Fig. 82. This allowed us to estimate the current output from the MHD based on the voltage applied to the PMT by the LED.

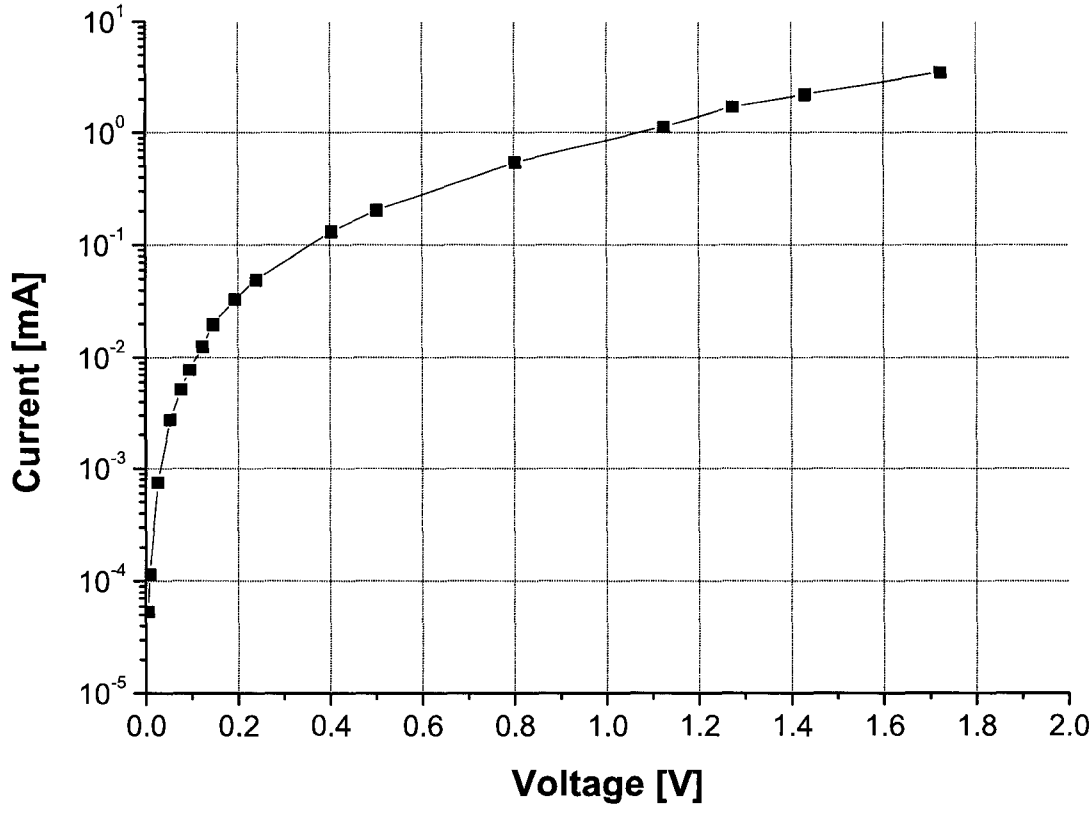

FIG. 82: Current and voltage dependence on the PMT for the LED.

The MHD model was positioned in the center of the quartz tube by using three symmetric glass spacers. In Fig. 83 is shown that the current pulse is much shorter then the driving pulse. This is due to the fact that the discharge breakdown conditions require a specific amount of microwave power. Additionally, the current pulse has an asymmetrical shape, which is most likely due to the time lag corresponding to the time of flight of the gas [37].

We determined that our MHD generator was able to produce about 20 mA of current when the PMT was given a 200 V bias by a DC high voltage power supply at an inlet pressure of 1.1 Torr, see Fig. 84. This proves that it is possible to generate current from the supersonic flowing discharges associated with Martian atmospheric entry.

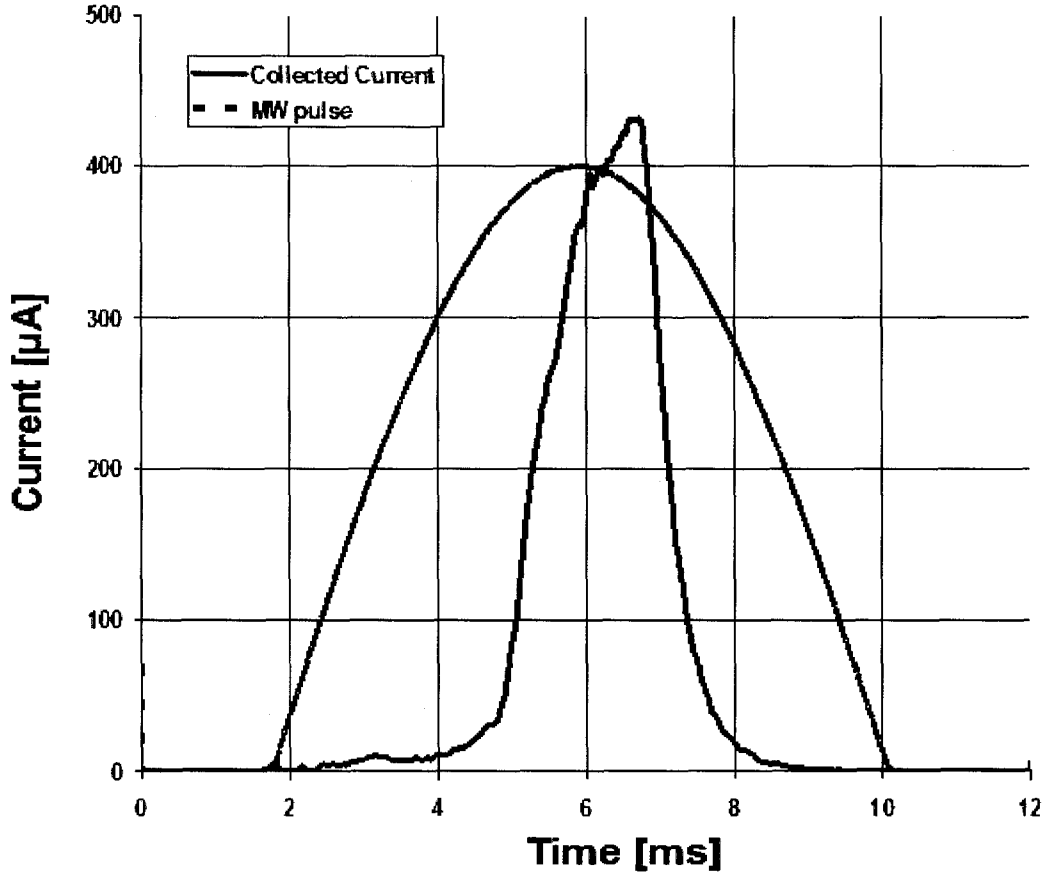

FIG. 83: Current and discharge pulse during breakdown in a discharge of Martian simulated gas.

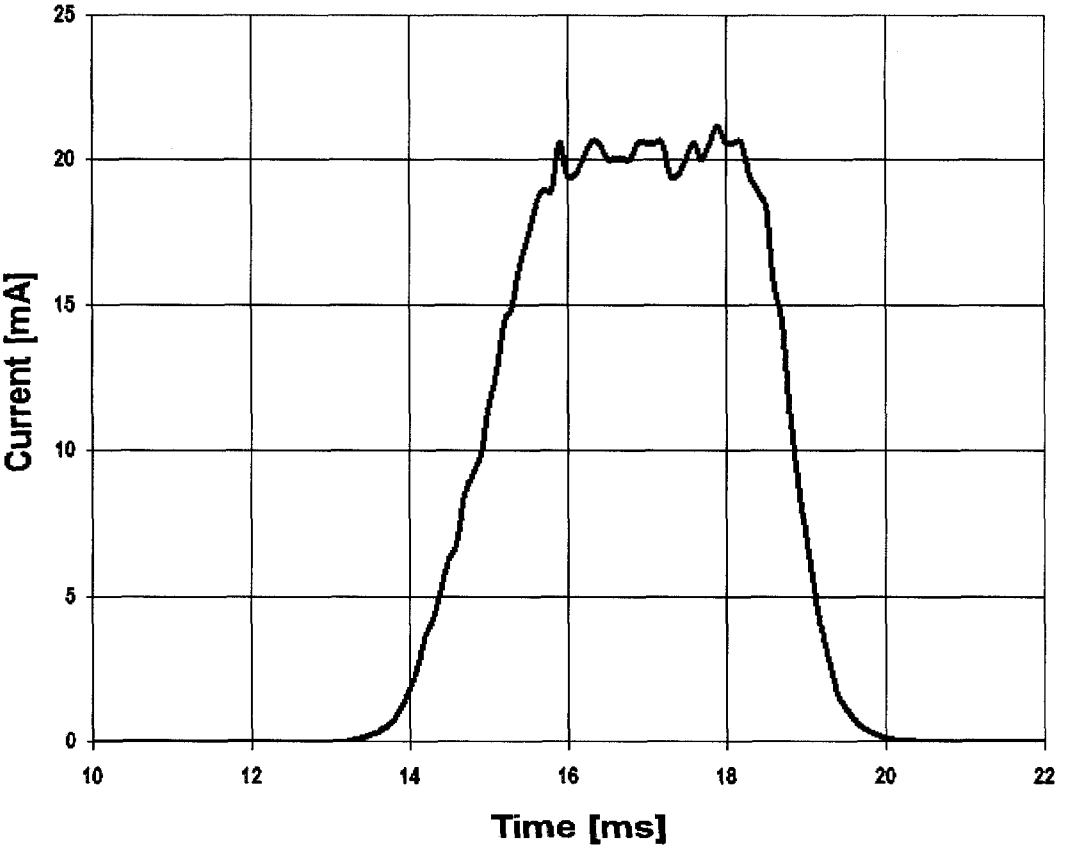

FIG. 84: Current generated by the MHD model as measured by the PMT.

APPENDIX B

PLASMOID IN AFTERGLOW

In the afterglow of the pure Ar and Ar with 1% H_2 discharge we observed a bright glow which we call a plasmoid. A picture of this plasmoid in a discharge of pure Ar is shown in Fig. 85. In order to find whether the plasmoid is formed by aerodynamic or electrodynamic effects of the flowing discharge, a series of experiments were performed. The first of these experiments was to look at the populations of different Ar I and Ar II states in the discharge. We chose a set of eight states corresponding to two ionic transitions, one 5p-4s transition, one 4p-4s transitions, and four 6s-4p transitions. In Fig. 86 we present a 1-D graph of the population distribution of the $4p[3/2] \rightarrow 4s[3/2]^o$ state at 714.704 nm as a function of the distance from the microwave cavity along the axis of symmetry for the discharge. From the figure, we observe that the population increases by approximately one order of magnitude over the entire length of plasmoid. This indicates that the plasmoid is detached from the plasma that is inside of the microwave cavity.

Futher, we created 2-D contour plots of all eight transitions to reveal how the populations very with both distance from the microwave cavity and perpendicularly to it. These graphs are taken at the positions from 3.5 to 10.5 cm from the cavity and vertically from 0.2 to 1.4 cm from the center of the quartz tube. It is important to note that the diameter of tube was 3.2 cm. We present these results in Fig. 87. From the data we see that the populations of the two Ar II states were stronger at the front of the plasmoid, the same as the population of the 470.232 nm line, which corresponds to a 5p-4s transition. For the lower level transitions (4p-4s and 6s-4p) the populations has a maximum in the middle of the plasmoid. In order to be completely understood, this distribution of excited and ionic states within the plasmoid will need to be studied in more detail.

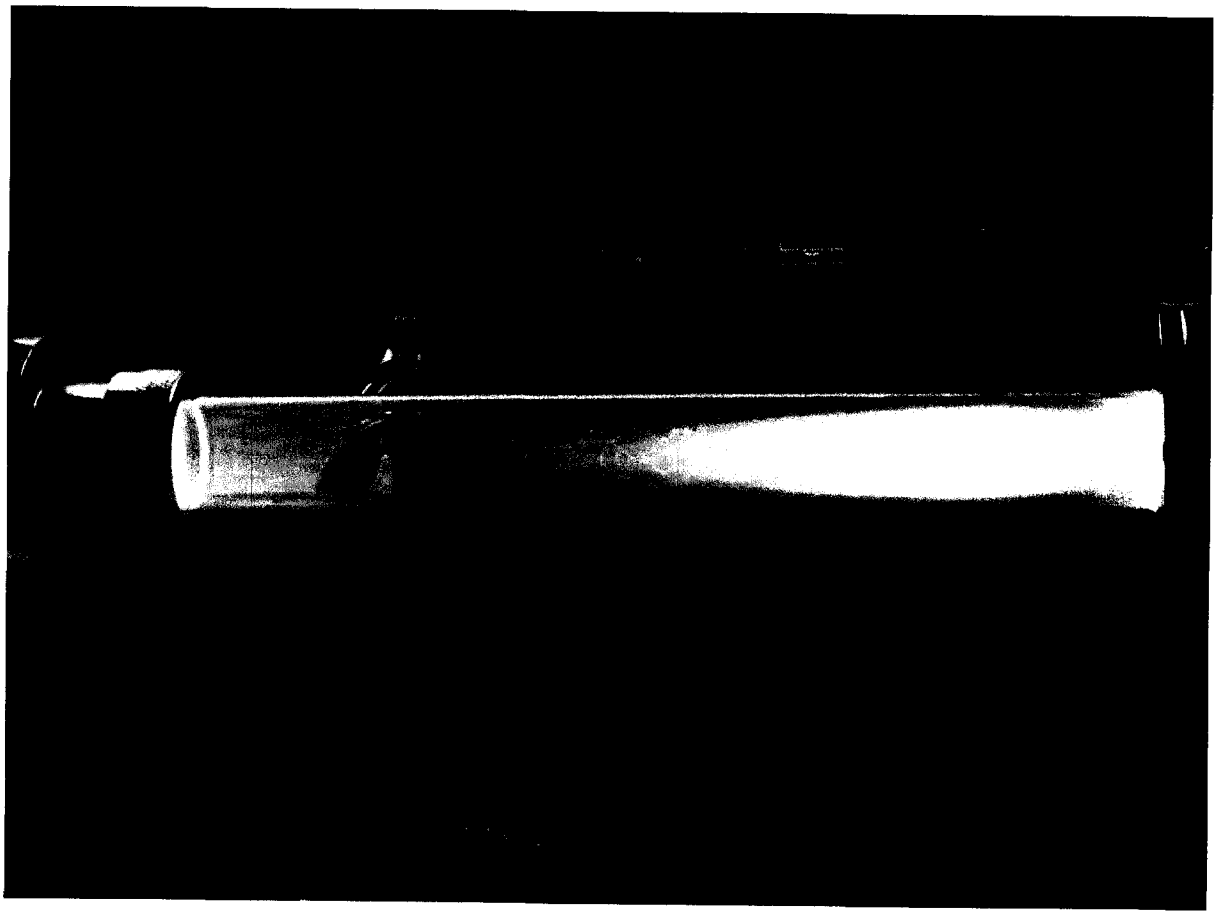

FIG. 85: Picture of the plasmoid in the afterglow region of an Ar discharge.

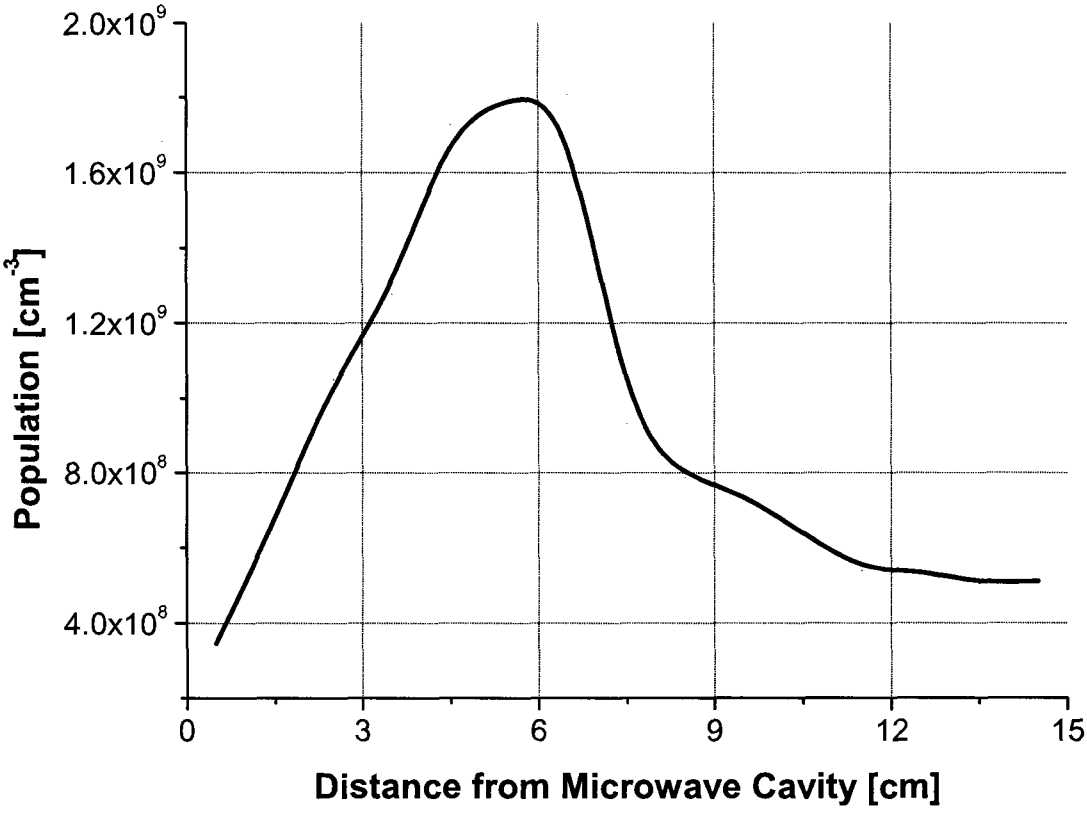

FIG. 86: Population of the 4p[3/2] $\rightarrow$ 4s[3/2]^o state at 714.704 nm as a function of the distance from the exit of the microwave cavity.

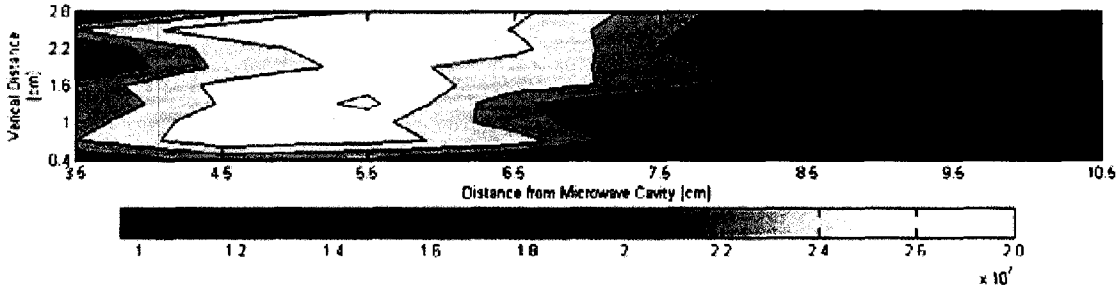

(a) $5p(\frac{1}{2}) \rightarrow 4s'(\frac{1}{2})^o$ at 470.232nm

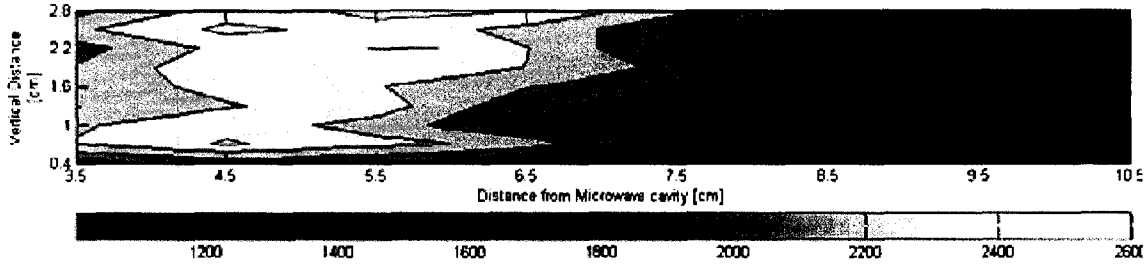

(b) $4p^2P^o \rightarrow 4s^2P$ at 476.487nm

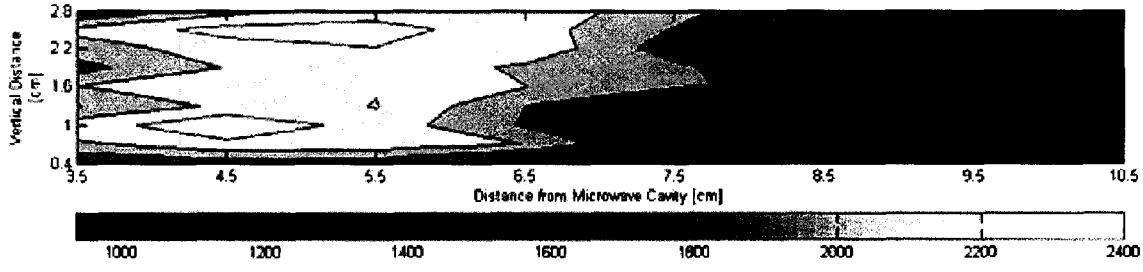

(c) $4p^4P^o \rightarrow 4s^4P$ at 480.602nm

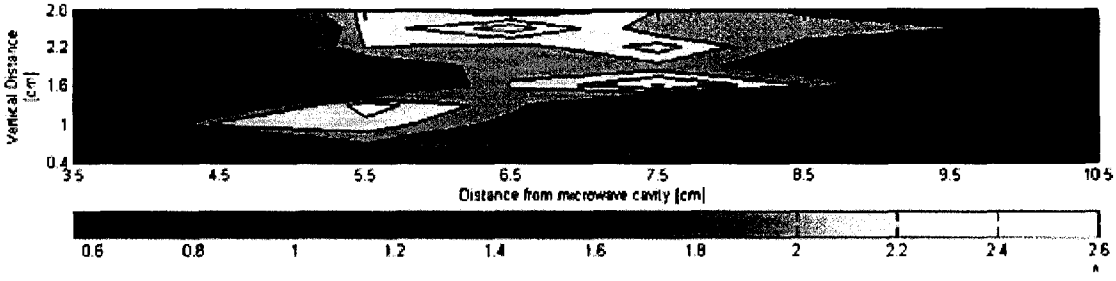

(d) $6s(\frac{3}{2})^o \rightarrow 4p(\frac{5}{2})$ at 710.748nm

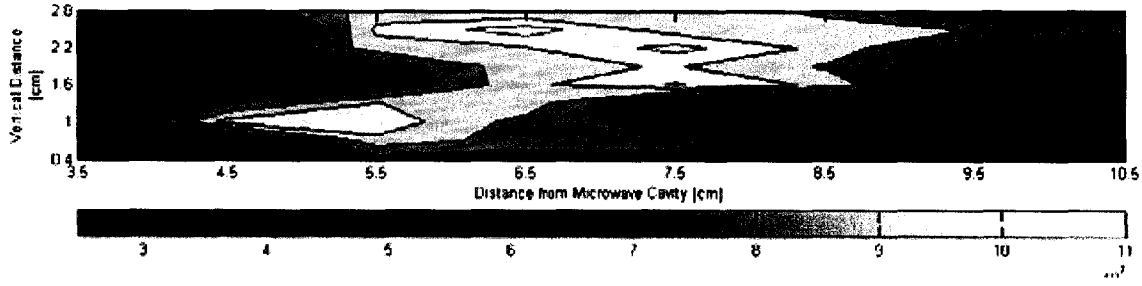

(e) $6s(\frac{1}{2})^o \rightarrow 4p(\frac{3}{2})$ at 712.582nm

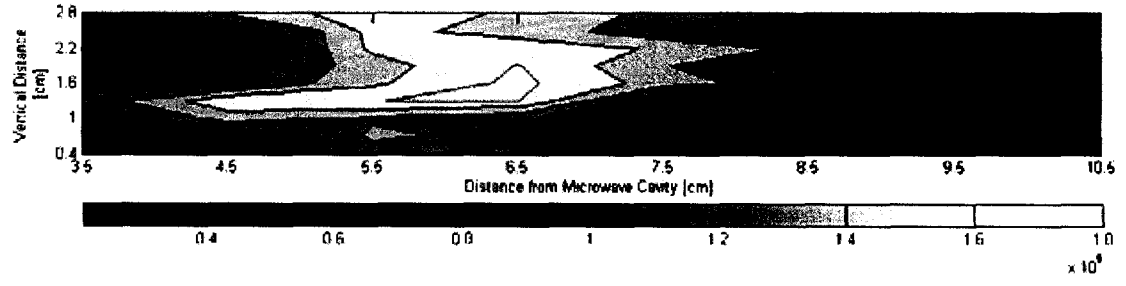

(f) $4p(\frac{3}{2}) \rightarrow 4s(\frac{3}{2})^o$ at 714.704nm

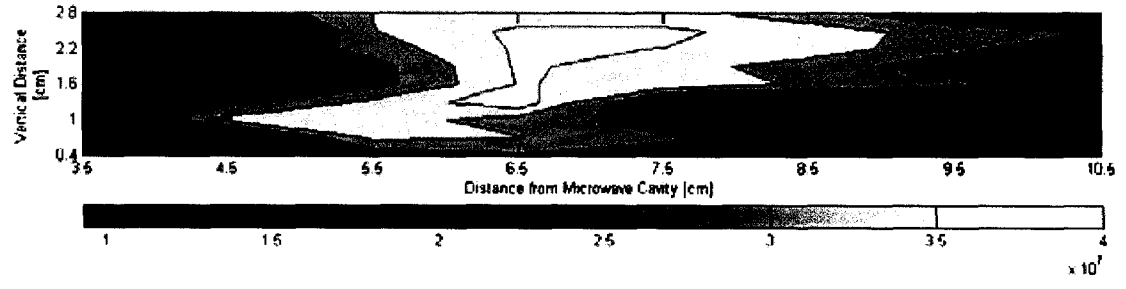

(g) $6s(\frac{1}{2})^o \rightarrow 4p(\frac{3}{2})$ at 715.884nm

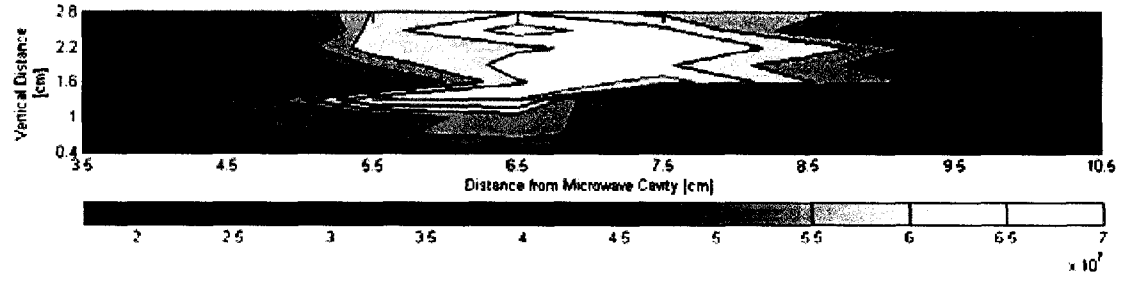

(h) $6s(\frac{1}{2})^o \rightarrow 4p(\frac{3}{2})$ at 720.698nm

FIG. 87: Population of Ar I and Ar II states in a pure Ar discharge within the plasmoid region of the afterglow.

We calculated the electron temperature based on the ratio of the Ar I to Ar II states using Eq. (50) and we present these results in Fig. 88. We see that the electron temperature did not vary substantuily through the plasmoid region. This indicates that the plasmoid was predominantly due to aerodynamic effects.

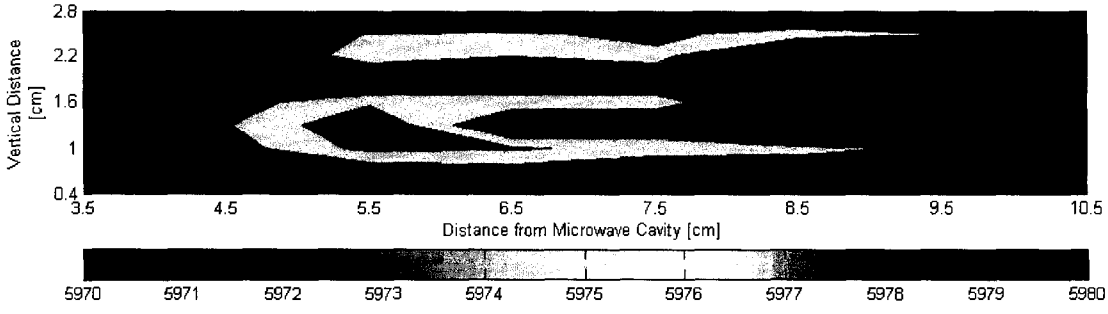

FIG. 88: Electron temperature along the plasmoid region of the afterglow.

To confirm this we performed a second set of experiments in which the cavity was moved in 1.0 cm increments. If the plasmoid is mostly due to aerodynamics, then it should stay in the same place within the quartz tube. However we found that the plasmoid moved with the position of the microwave cavity, which would indicate that there are electrodynamic effects causing this phenomena to form within the afterglow region. More experiments are measured in order to completely understand the discharge parameters in this region and subsequently the electrodynamic and aerodynamic effects as well as how they combine to form the plasmoid.

VITA

Dereth Janette Drake
Department of Physics
Old Dominion University
Norfolk, VA 23529

EDUCATION

May 2009 **Ph.D.**, Physics, Old Dominion University
Dissertation: *Characterization of Microwave Cavity Discharges in a Supersonic Flow*

May 2005 **M.S.**, Physics, Old Dominion University

May 2002 **B.S.**, Physics and Applied Mathematics, Longwood University

HONORS AND AWARDS

Graduate Student Researchers Program Fellowship for 2007-2009
NASA's Marshall Space Flight Center

Aerospace Graduate Research Fellowship for 2006-2009
Virginia Space Grant Consortium

Honorable Mention for Outstanding Graduate Poster Presentation
2008 Research Exposition

Student Travel Award for 2005-2008
Gaseous Electronics Conference

Best Physics Presentation
2006 Spring Research Symposium

PROFESSIONAL MEMBERSHIP

American Physical Society

Typeset using LaTeX.